FLOW IN THIN POLYMER FILMS

FLOW IN THIN POLYMER FILMS: MOLECULAR STRUCTURE, INITIAL CONDITIONS, AND BOUNDARY CONDITIONS

By

MARK ILTON, M.Sc.

A Thesis
Submitted to the School of Graduate Studies
in Partial Fulfillment of the Requirements
for the Degree
Doctor of Philosophy

McMaster University
©Copyright by Mark Ilton, 2015.

DOCTOR OF PHILOSOPHY (2015)
(Physics)

McMaster University
Hamilton, Ontario

TITLE: Flow in thin polymer films:
molecular structure, initial conditions, and boundary conditions

AUTHOR: Mark Ilton, M.Sc.(University of Waterloo)

SUPERVISOR: Dr. Kari Dalnoki-Veress

NUMBER OF PAGES: x, 143

Abstract

Surface tension driven flow is studied in films of viscous polymer liquid by monitoring the spreading of droplets or the capillary levelling of films with excess surface area. The research presented in this thesis is focused on three major themes where molecular details are important to flow: molecular anisotropy, interfacial friction, and the initial state of the film.

The effect of molecular anisotropy is studied by examining the dynamics of partially wetting diblock copolymer droplets using optical microscopy. The shape of the droplets is measured as they evolve towards equilibrium. In this system, it is found that energy is dissipated at the base of the droplets. This is consistent with a reduced interfacial friction at the liquid-substrate interface.

Flow dynamics are also found to depend on the symmetry of the initial film thickness profile. Thickness perturbations with different degrees of symmetry were created in an initially flat film using focused laser spike annealing. The films were allowed to flow under the driving force of surface tension, and using atomic force microscopy, the film thickness profile was measured as a function of time. We find the depth of the perturbations decreases as a power law in time, with a power law exponent that depends on the symmetry of the thickness perturbation.

The role of interfacial effects are explored by studying the flow in a film with zero interfacial friction: a freely-suspended film. Flow is measured in films with no interfacial friction using a technique which creates a film with a sharp step in the initial thickness profile. The excess surface area at the edge of the step drives flow, and information about the dynamics of the fluid is obtained by measuring the width of the step over time with atomic force microscopy. We observe flow that is consistent with plug flow: where the velocity of the fluid in the plane of the film is constant along the direction perpendicular to the film.

Finally, freely-suspended films provide a model system to study the nucleation and growth of pores in a membrane. By purposefully creating pores of different initial size, the critical radius for nucleation is measured as a function of the membrane thickness. The experimental results agree with a simple model in which the free energy cost at the perimeter of a pore is determined by the excess surface area due to the curved interface of the pore edge.

Acknowledgements

There are so many people I would like to thank. These past four years have been an incredible journey, and I have been fortunate to have amazing people by my side every step of the way.

First of all, I would like to thank my supervisor Kari Dalnoki-Veress. Kari, I am so grateful for everything you have taught me. Your infectious excitement for science has made every day fun. You have opened my mind to viewing the world through the lens of trust, enthusiasm, and optimism. The passion you have for research, teaching, and learning have left a lasting impression on me. You have taught me to reflect on concepts to develop intuition. You have been my mentor, role model, collaborator, and friend. Thank you, I truly can't imagine doing this without you.

I would also like to thank all the members of the "KDV experience" I had the pleasure of working with. Thank you for patiently teaching me, for showing me what can be accomplished with dedication, and for helping to create amazing environment where teamwork comes so naturally. Paul, I have sincerely enjoyed all the time we have spent together in and out of the lab. Even the most daunting days spent making impossible samples are great memories that I will cherish. Thank you for all of our chats, for always helping me out (including proofreading this thesis), and for telling me what music to listen to.

To my friends and colleagues in the Department of Physics and Astronomy at McMaster University, thank you for the stimulating discussions, for sharing your research and your friendship. I would like to mention in particular the staff in the main office whose dedication and care makes a huge difference. Thank you for always taking the time to help.

Outside of McMaster, I would like to thank my family and close friends for their continual love and support. I am so blessed to be surrounded by such incredible, generous, and loving people. Thank you for everything.

Finally, I would like to thank my partner Amanda. You have always believed in me, encouraged me, and supported me in everything I do. You believe in my dreams so strongly that I have no choice but to believe in them as well. Words cannot express how grateful I am for the strength and balance you give me. Thank you.

Contents

List of Figures

Chapter 1

Introduction

The study of thin films of a polymeric liquid is the backbone of this thesis. Thin polymer films are used extensively in industrial applications including lubricating coatings, masks for photolithography, and adhesives. The use of thin polymer films in emerging technologies like flexible displays, high density data storage, organic electronics, and self-healing paint provides further motivation to understand their physical properties at the nanoscale. Polymer molecules are particularly useful in nanotechnology applications because of the ability to alter their molecular architecture, allowing for control of patterning down to sub-10 nm lengthscales [1–3].

From an experimental perspective, a benefit of studying polymeric liquids is their tunable physical properties. For example, by changing temperature, the viscosity of a polymeric liquid can change by orders of magnitude which allows experimenters the ability to speed up or slow down dynamics to suit their needs [4]. Other properties have the potential for alteration, such as the surface tension or the wetting conditions of the fluid. This provides a convenient system for the study of fluid dynamics. Since the material properties are tunable, the fluid dynamics can be studied over a range of lengthscales and forces.

A final, and perhaps most important motivation for using polymeric liquids to study fluid dynamics is the ability to make and measure thin films where the molecular details become important. Typically, a polymer molecule is on the order of $\sim 1 - 100\,\text{nm}$ in its unperturbed state, depending on the molecular weight. In fluid dynamics, one basic assumption is that the matter forms a continuum, and the density of the fluid is independent of the lengthscale being examined. By studying films only a few molecules thick, the effect of perturbing polymer molecules from their equilibrium conformations can be observed, thus introducing the possibility to measure deviations from the continuum approximation.

This thesis is structured around three themes where the molecular details play a non-trivial role in determining the flow properties: 1) Molecular anisotropy and heterogeneity, 2) Initial state of the film (initial condition) 3) Interfacial friction (boundary conditions). Each of these are active areas of research, and an overview of these three area provided in Section 1.5.2. A brief description of each area is provided here to put the five papers described in this thesis (see Chapter 3) in the context of these three categories.

Molecular anisotropy and heterogeneity

When a thin film is homogeneous and isotropic in both composition and dynamic properties, its flow can be described with a uniform viscosity. In contrast, materials which have molecular heterogeneity or anisotropy have a more complicated viscosity. There are a few experimental systems in which heterogeneity or anisotropy have been shown to play a large role, such as glassy polymer films near their glass transition temperature or films in which the molecules are confined. In this thesis, Papers I and II presented in Chapter 3 examine the effect of molecular anisotropy by using a particular type of polymer fluid - a diblock copolymer. An introduction to this class of materials is presented in Section 1.2.3, and the effect of anisotropy on the free energy of a diblock copolymer film is described in Section 1.3.2. The results of Paper I, where a quantized spectrum of contact angles is observed for diblock copolymer droplets, is a direct consequence of the free energy of the diblock copolymer film. While Paper I describes the equilibrium state of these droplets, Paper II examines the dynamics of the droplets as they approach their equilibrium state.

Initial state of the film

Depending on how a thin film is prepared, the measured flow can differ. For example, spin coating is a common method of creating films (see Section 2.1), which can leave residual stresses that results in an apparent viscoelastic response of the film during flow. Another way that the initial condition can affect flow is by the periodicity of an initial thickness variation in the film. Short wavelength variations decay more rapidly than long wavelength variations, which is explained in Section 1.4.2. In this thesis, Paper III details how the symmetry of an initial thickness variation with finite horizontal extent determines the relaxation of the thickness profile as the film undergoes capillary levelling.

Interfacial friction

The boundary condition of fluid flow at a liquid-solid interface is in many situations a "no-slip" boundary condition, where the liquid molecules have zero horizontal[1] velocity at the interface. Because the interfacial friction between the liquid and solid is so large, the molecules are unable to move horizontally at the interface. However, there are some liquid-solid combinations which have a relatively low interfacial friction, allowing the liquid molecules to slide across the solid interface. This is the "slip" boundary condition. There are several polymeric fluids which show slip effects. In this thesis, Papers IV and V examine films which are freely-suspended with no solid substrate. In that case there are two free interfaces of the film with no interfacial friction. This is an extreme limit of slip which cannot be realized on a substrate as there is always some degree of interfacial friction. Paper IV investigates flow in these "freestanding" films by using a capillary levelling technique reviewed in Section 1.5.1. Paper V examines the growth and shrinkage of pores, making connections to biological membranes.

With these themes in mind, this thesis will proceed as follows. Since this is a 'sandwich thesis', each of the 5 papers (published or submitted) will be presented with a preface in Chapter 3. Before that, the background information to the thesis will be presented. Chapter 1 provides an introduction to the structure and flow of thin polymeric fluids. Chapter 2 gives the experimental details of the thesis work, describing in detail the sample preparation and measurement techniques used. Finally, some general conclusions are drawn in Chapter 4 which tie together the work and discuss future research.

In this introductory chapter, an overview of fluid dynamics relevant to flow at small lengthscales will be presented first. Then, specific details about polymeric liquids will be given before delving into the equilibrium free energy and fluid dynamics

---

[1] For brevity, in this thesis the direction parallel to the liquid-substrate interface will be referred to as the "horizontal" direction.

of thin polymer films. Finally, the current experimental literature relating to the measurement of flow in polymeric fluids at small lengthscales will be reviewed.

1.1 Fluid dynamics at small length scales

One of the more remarkable aspects of the field of fluid dynamics is its breadth. Continuum fluid dynamics and the Navier-Stokes equation can be used to describe flows which occur on astronomical lengthscales down to flows at the nanoscale. Moreover, the types of flow (e.g. turbulent versus laminar) and forces involved vary depending on the system studied. As a consequence of this breadth, it is often necessary to narrow down study to a particular flow regime. To do so, one must consider the relevant forces involved in the system under study. A useful way to conceptualize the different forces involved is in terms of driving forces which push liquid to flow, and mediating forces which are internal to the fluid and emerge in response to flow. Examples of driving forces include surface tension, gravity, and external fields such as an electromagnetic field. Some mediating forces are viscous and inertial forces. Any given flow regime will involve one or more driving force and one or more mediating force.

For example, when a honey dipper is pulled out of a jar of honey, a stream of liquid honey flows off the end of the dipper and back into the jar. The potential energy due to the driving force of gravity is dissipated as friction through the viscous sliding of fluid molecules past one another. In this regime, there is gravity driven flow mediated by viscosity. Contrast flowing honey with a water droplet in space. When a water droplet is formed (by pinching out of a tube for example) surface tension will drive the droplet towards a spherical shape. However, since water has a significant inertial component, the momentum of the droplet will cause it to overshoot a spherical shape. This dynamic motion will cause the droplet shape to oscillate, and in the limit of a frictionless droplet the oscillations will continue indefinitely due to inertia. This is the regime of surface tension driven flow mediated by inertia. From these two examples we can develop some general characteristics of how the different forces affect fluids. For the driving forces, surface tension tends to favour spherical shapes (or surfaces of constant curvature), whereas gravity favours flattening of the fluid. For the mediating forces, inertial forces typically lead to an oscillatory motion while viscous forces cause damped motion.

This thesis will focus on the regime of surface tension driven flow mediated by viscosity, which usually describes flows at small lengthscales. For small volumes of fluid, the gravitational force is small in comparison to the forces of surface tension. A way to characterize this is through the capillary length [5]

$$L_c \equiv \sqrt{\frac{\gamma}{\rho g}}, \tag{1.1}$$

where γ is the surface tension of the fluid, ρ is its density, and g is the gravitational acceleration. For lengthscales much larger than L_c, gravitational forces dominate. For lengthscales much smaller than L_c, capillary forces (surface tension) dominates. The capillary length of both water at room temperature and polystyrene in its liquid state are approximately 2 mm. So for droplets and films with a size on the order of microns or lower, gravity makes a negligible contribution to the dynamics of flow.

The relative contributions of the two common mediating forces (inertial and viscous forces) is typically characterized by the Reynold's number of the fluid [5], defined by

$$Re \equiv \frac{\rho v L}{\eta} = \frac{\rho \gamma L}{\eta^2}, \tag{1.2}$$

where the characteristic velocity v is set by the ratio of surface tension to viscosity $v_c = \gamma/\eta$ (the capillary velocity), and L is a characteristic lengthscale. Viscous forces dominate for small Reynold's numbers, whereas turbulent flow can occur for large values of the Reynold's number. An alternate way to think about the relative contribution of the mediating forces is through the characteristic lengthscale

$$L_r \equiv \frac{\eta^2}{\rho \gamma}, \tag{1.3}$$

which for capillary driven flows is the lengthscale at which viscous and inertial forces are comparable. Above this lengthscale, inertial forces begin to dominate, whereas for droplets and films much smaller than this characteristic lengthscale, viscous forces dominate. Here the difference between water and polystyrene offers a stark contrast. For water at room temperature with $\eta \sim 1\,\mathrm{mPa\cdot s}$, the characteristic lengthscale is

$L_r \sim 10\,\mathrm{nm}$, while for polystyrene with a typical viscosity of $1\,\mathrm{MPa\cdot s}$ this characteristic lengthscale is larger than the diameter of the sun. This lengthscale is only relevant for capillary driven flow and gravitational effects become significant for polystyrene long before this astronomical lengthscale is reached. In other words, because the viscosity is large for typical polymeric liquids, whenever gravity can be ignored, so too can inertia. This is not the case for water or other fluids with a low viscosity.

Therefore, for small volumes of a viscous liquid both gravity and inertia can be ignored, and this thesis focuses on surface tension driven flow mediated by viscosity. To study this regime, we perform experiments with high viscosity fluids at small lengthscales, specifically polymeric liquids.

1.2 Polymeric liquids

Polymers are materials comprised of long molecules (chains) made of smaller repeating subunits (monomers) covalently bonded together. Polymers are well suited for fluid dynamics research for several reasons. First, their large molecular size makes the study of molecular confinement accessible at larger lengthscales compared to small molecule liquids. Second, the viscosity of polymeric liquids are tunable with both temperature and molecular weight, and can be altered by orders of magnitude without substantially changing the surface tension. Third, commercially available polymers have a wide variety of chain architectures and chemical compositions which allows for the study of anisotropic materials. Each of these three properties of polymers will be discussed in the following sections in further detail, which is based on the discussion in reference [6].

1.2.1 Size of a polymer molecule

One way to characterize the size of a polymer molecule is by its molecular weight. For the same repeating subunit, molecules with a greater mass correspond to having more repeating units, and as a result is a larger molecule. Suppose there was a polymeric liquid with chains having many different molecular weights M_i, and there were N_i chains with molecular weight M_i. To characterize the molecular mass of such a collection of polymer chains, the number-averaged molecular weight can be used

$$M_n = \frac{\sum_i N_i M_i}{\sum_i N_i}, \tag{1.4}$$

which gives the average molecular weight per chain. Another way to characterize the overall molecular weight is through the weight-averaged molecular weight, where the number of molecules N_i in the above equation gets replaced by their weight $N_i M_i$ to give

$$M_w = \frac{\sum_i N_i M_i^2}{\sum_i N_i M_i}. \tag{1.5}$$

When using polymers to study fluid dynamics it is typically desirable to use polymers with a single chain size. In that case $M_n = M_w$ and the polymer is "monodisperse". The ratio of the weight-averaged to the number-averaged molecular weights is a measure of how many different molecular components there are in the polymer, or to what extent it is "polydisperse". The polydispersity index $\mathrm{PI} = M_w/M_n$ equals one for a monodisperse polymer and greater than one when there is more than one molecular component. All the polymers used in this thesis have a low polydispersity with $\mathrm{PI} < 1.1$.

Although the molecular weight of the polymer gives indirect information about how large the polymer chains are, a physical lengthscale is required to understand when confinement effects might occur in a thin film. A potential choice for this lengthscale is the length along the backbone of a single chain. Figure 1.1 shows a schematic of a polymer chain. Given the bond length l and bond angle θ between the n repeating subunits, the contour length is the maximum extension of the polymer chain $R_{\max} = nl\cos(\theta/2)$. Another potential lengthscale is the average distance between the two ends of the polymer chain, the end-to-end displacement $< \vec{R} >$.

Since for typical polymer molecules, the correlations between the successive subunits falls off exponentially with a characteristic length only a few subunits long, the probability of finding a chain in a stretched state is infinitesimally small. The chain can be divided into N Kuhn monomers of size b such that the contour length $R_{\max} = Nb$. The conformations of successive Kuhn monomers is uncorrelated so the polymer chain is a random walk of N segments with length b. As a consequence, the probability of finding a chain with an end-to-end distance vector $\vec{R}$ is given by a

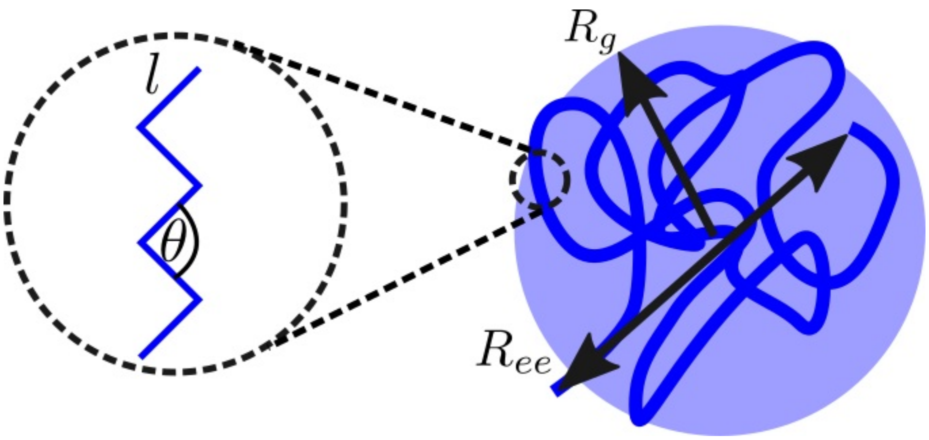

Figure 1.1: Characteristic lengthscales of a polymer chain. On the lengthscale of an individual monomer, the bond length l is a relevant size. However, because correlations between the direction of neighbouring subunits decay over roughly 10 monomers for many polymers, the bond length does not provide a useful characterization of the size of the polymer chain. Instead, the radius of gyration of the polymer R_g or the end-to-end distance R_{ee} give the characteristic size of a polymer chain.

Gaussian distribution

$$P(\vec{R}) = \left(\frac{3}{2\pi N b^2}\right)^{3/2} \exp\left(\frac{-3R^2}{2Nb^2}\right). \tag{1.6}$$

The probability distribution for $\vec{R} = (x, y, z = 0)$ is shown in figure 1.2. The distribution is axisymmetric with a peak at $\vec{R} = 0$, and so the end-to-end displacement averaged over an ensemble of chains is zero. This average end-to-end displacement can be explicitly calculated by integrating

$$< \vec{R} >= \int d^3\vec{R}\ P(\vec{R}) = 0. \tag{1.7}$$

From examining the probability distribution of chain lengths, the two candidate characteristic lengthscales for the polymer chain do not work. Since the the end-to-end displacement is zero, and the contour length is an unlikely state for a random walk, neither is an ideal lengthscale characterizing the size of the molecule. An alternative is to take the root mean square end-to-end distance given as $R_{ee} = \sqrt{< R^2 >} = N^{1/2}b$, or the radius of gyration $R_g = N^{1/2}b/\sqrt{6}$.

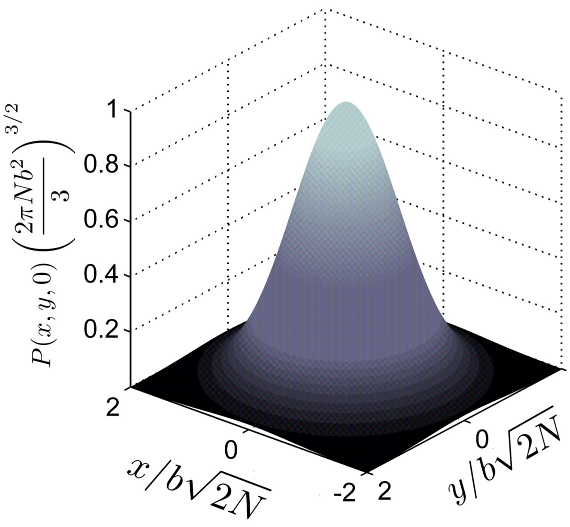

Figure 1.2: The probability distribution for finding a polymer chain with N Kuhn monomers of length b at an end-to-end distance $\vec{R} = (x, y, z = 0)$. The distribution is peaked at $\vec{R} = 0$.

Since the molecular weight of a chain is proportional to the number of Kuhn monomers in a chain ($M_w \propto N$), we can write R_g as

$$R_g = \zeta \sqrt{M_w}, \tag{1.8}$$

where ζ is a material dependent parameter. Table 1.1 shows the radius of gyration and constant ζ for polymers used in this thesis. Polystyrene (PS), poly(methylmethacrylate) (PMMA), and poly(2-vinyl pyridine) (P2VP) all have similar R_g for a given molecular weight.

Table 1.1: Radius of gyration for typical molecular weights and polymers used in this thesis. For PS and PMMA, R_g is determined from equation 1.8 with the parameter ζ taken from ref. [7]. The R_g for P2VP is approximated by PS of the same molecular weight [8].

	R_g ($M_w = 16$ kg/mol)	R_g ($M_w = 55$ kg/mol)	ζ (nm (mol/g)$^{1/2}$)
PS	3.40 nm	6.31 nm	0.0269
PMMA	3.36 nm	6.24 nm	0.0266

1.2.2 Viscosity of an amorphous polymer

For a polymeric fluid, the viscosity, which characterizes the frictional interaction between molecules, depends strongly on temperature T and the molecular weight of the polymer. A useful way to think about a material in its liquid state at the molecular level is to picture molecules in a crowded environment. In order for a single molecule to move and allow for flow, it needs to escape the surrounding cage of its neighbouring molecules. For a liquid with a low molecular friction coefficient this process can occur easily. At higher temperatures, there are more thermal fluctuations of the molecules, which increases the attempt frequency of escape. Therefore for a simple small molecule liquid, the ability to flow increases with increasing temperature, but decreases with an increasing frictional coefficient. In other words, the viscosity should increase with the molecular friction coefficient, but decrease with temperature.

These arguments do not take into account the connectivity of the molecules. For a monomer to move in a polymer fluid, the other monomers in the chain also need to move. Since the number of monomers is proportional to the molecular weight, the viscosity should increase with increasing molecular weight. There are two different regimes for this molecular weight dependence, which have different power law exponents for how the viscosity scales with molecular weight. The cross-over between these two regimes occurs at the entanglement molecular weight M_e. For molecular weights larger than M_e, topological constraints (entanglements) from surrounding chains confine the motion of a polymer chain to a tube. For molecular weights smaller than M_e, the chains can be modelled as N beads connected by springs, which are confined by neighbouring chains.

In order to proceed in either of the low molecular weight or high molecular weight cases, we proceed based on the discussion in reference [9] by considering the longest relaxation time of the material τ^*. The viscosity of the fluid can be approximated by the product of the plateau modulus and relaxation time [10]

$$\eta \approx \tau^* G(\tau^*). \tag{1.9}$$

The relaxation time can be found by considering the time it takes for a molecule to diffuse out of its cage with a characteristic size L,

$$\tau^* \approx \frac{L^2}{D}, \tag{1.10}$$

where D is the diffusion coefficient of the molecule inside its cage. The plateau modulus is given by

$$G(\tau^*) \approx 3\nu k_B T, \tag{1.11}$$

where ν is the number density of elastic constraints each storing energy $k_B T$. In short, the viscosity can be calculated using equation 1.9, knowing the relaxation time and plateau modulus.

We now derive the molecular weight scaling of the viscosity by inferring relations for the relaxation time and plateau modulus using physical arguments [10]. In the case of high molecular weights ($M_w > M_e$) polymer chains are entangled and for flow to occur a molecule has to diffuse out of its confining tube. The entanglements, which are on average N_e monomers apart, break up the tube into N/N_e unconstrained segments each with a characteristic size of $bN_e^{1/2}$. This gives a total path length of the unconstrained segments, the primitive path Λ, as

$$\Lambda = \frac{N}{N_e} b N_e^{1/2} = \frac{bN}{N_e^{1/2}}. \tag{1.12}$$

We need to consider the time it would take a chain to diffuse a distance Λ, with a diffusion coefficient given by the Einstein relation

$$D_{\text{rep}} = \frac{k_B T}{\mu_0 N}. \tag{1.13}$$

Here the frictional coefficient is assumed to be proportional to monomeric frictional coefficient μ_0 times the number of monomers N. This gives the reptation time

$$\tau_{\text{rep}} \approx \frac{\Lambda^2}{D_{\text{rep}}} \approx \frac{b^2 \mu_0}{k_B T} \frac{N^3}{N_e}. \tag{1.14}$$

To obtain the viscosity, first the plateau modulus needs to be determined. The elastic constraints are due to the entanglements which have a number density $\nu \approx 1/N_e b^3$.

Substituting this into equation 1.11

$$G(\tau_{\text{rep}}) \approx \frac{3k_BT}{N_eb^3}, \tag{1.15}$$

and then combining the reptation time and plateau modulus yields the viscosity in the entangled, high molecular weight regime

$$\eta_{\text{rep}} \approx \tau_{\text{rep}}G(\tau_{\text{rep}}) \approx 3\frac{\mu_0}{b}\frac{N^3}{N_e^2}. \tag{1.16}$$

The viscosity scales with the number of monomers cubed (or molecular weight cubed) for large molecular weight. Now, the same procedure for determining the viscosity will be applied to the low molecular weight case.

For low molecular weights, the longest relaxation time of a polymer melt is given by the Rouse model. In that model, each monomer is treated as a bead connected to its neighbour by a spring. The longest relaxation time, or Rouse time τ_R, is the self-diffusion time of the chain. The chain diffuses a distance $bN^{1/2}$, with the same diffusion coefficient given by equation 1.13. This gives the Rouse relaxation time as

$$\tau_R \approx \frac{N^2b^2\mu_0}{k_BT}. \tag{1.17}$$

Since the elastic constraint is provided by the neighbouring springs, the number density of elastic constraints is the number density of chains ($\nu \approx 1/Nb^3$). The plateau modulus is thus

$$G(\tau_R) \approx \frac{3k_BT}{Nb^3}, \tag{1.18}$$

leading to a viscosity of

$$\eta_R \approx \tau_RG(\tau_R) \approx 3\frac{\mu_0}{b}N. \tag{1.19}$$

Equation 1.19 and 1.16 show the viscosity scaling with molecular weight for the low molecular weight unentangled case and high molecular weight entangled case respectively. At low molecular weight, the viscosity is linearly related to the molecular weight. As molecular weight is increased, this dependence becomes stronger scaling with the cube of molecular weight. These scaling laws are useful in understanding why the viscosity changes with molecular weight, however, they are only an approximation

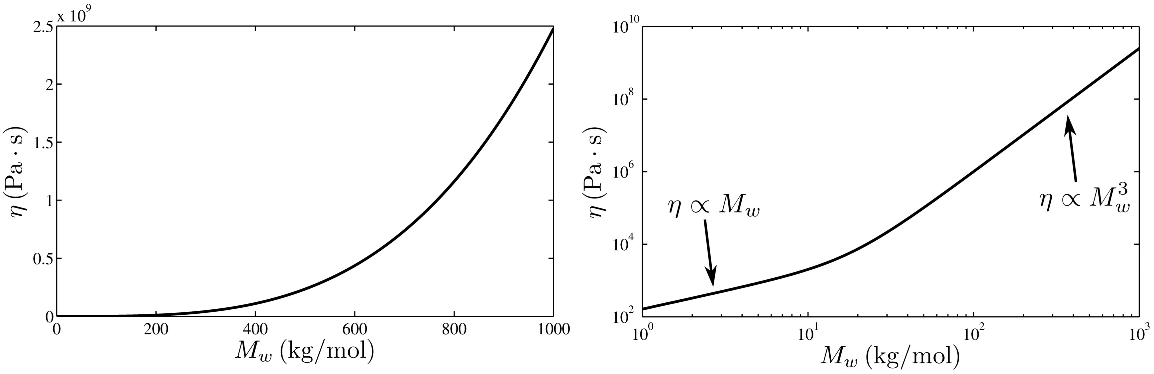

Figure 1.3: The molecular weight dependence of polystyrene viscosity. Here equation 1.20 is used with literature parameters for polystyrene, $\eta(192\,\mathrm{kg/mol}) = 9.1\times 10^6\,\mathrm{Pa\cdot s}$ [13] and $M_e = 18.1\,\mathrm{kg/mol}$ [14].The left plot has linear axes, while the right has logarithmic axes to show the power law relationship between η and M_w.

to a more precise empirical relation given by [11, 12]

$$\eta \propto M\left[1+\left(\frac{M}{M_e}\right)^{2.4}\right]. \tag{1.20}$$

Using $\eta = 9.1\times 10^6\,\mathrm{Pa\cdot s}$ at $T = 140°\mathrm{C}$ for 192 kg/mol [13], and $M_e = 18.1\,\mathrm{kg/mol}$, [14], the molecular weight dependence of PS is plotted in figure 1.3, on both linear axes (left panel) and logarithmic axes (right panel). The two different power-law scaling regimes are clearly visible as lines of constant slope in the right panel.

The viscosity of an amorphous polymer also depends on temperature. Amorphous polymers are a class of glass forming liquid, which means their viscosity appears to diverge as temperature decreases. One successful and widely used model to describe the viscosity of glass forming liquids is the Vogel-Fulcher-Tammann (VFT) equation. The viscosity is modelled with activation temperature T_A, and a temperature where the viscosity diverges T_v, such that

$$\eta(T) = \eta_0 \exp\left(\frac{T_A}{T-T_v}\right). \tag{1.21}$$

The parameters η_0, T_A, and T_v depend on the polymer and its molecular weight. Although assuming a diverging viscosity provides an effective model, it is not a nec-

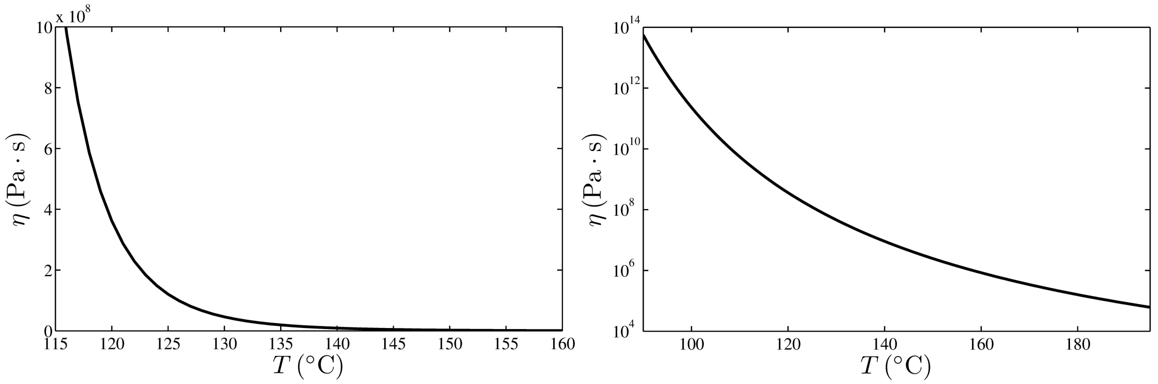

Figure 1.4: The temperature dependence of polystyrene viscosity. Here equation 1.21 is used with literature parameters for polystyrene, $\eta(192\,\mathrm{kg/mol}) = 9.1\times10^6\,\mathrm{Pa{\cdot}s}$ [13], $T_A = 1250\,\mathrm{K}$ and $T_v = 320\,\mathrm{K}$ [8]. The left panel shows linear axes, while the right has a logarithmic y-axis to show the divergence of the viscosity with temperature.

essary assumption to describe the temperature dependence of the viscosity. Other non-diverging models also give a reasonable fit to experimental data [15].

The VFT equation is plotted in figure 1.4 for PS using $T_A = 1250\,\mathrm{K}$ and $T_v = 320\,\mathrm{K}$ [8], as well as the reference viscosity $\eta = 9.1\times10^6\,\mathrm{Pa}\cdot\mathrm{s}$ at $T = 140°\mathrm{C}$ for 192 kg/mol [13]. The viscosity diverges as the temperature is decreased.

1.2.3 Structured fluid - diblock copolymers

The flow of a polymeric liquid also depends on its molecular structure. A polymer chain can be comprised of many different chemical species, and although for the purposes of this thesis the specific chemical details will be ignored, the overall arrangement of chemical species can cause differences in rheological properties. One possible arrangement is where each chain is comprised of two different chemical species which are separated into two different blocks - a diblock copolymer. A schematic of a single diblock copolymer chain is shown in the left panel of figure 1.5. When many chains are brought together, there is an enthalpic benefit to having the similar blocks together which drives phase separation. Since the two chemical species are bonded together, phase separation can only occur on the lengthscale of an individual chain (tens of nanometres). This small scale phase separation, known as microphase separation, causes the fluid to be structured [16]. For chains where the two blocks are of equal

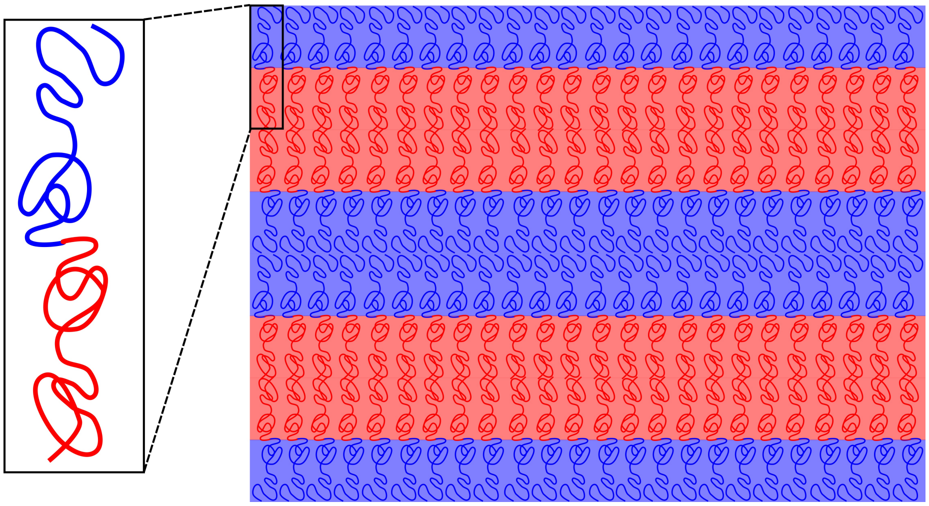

Figure 1.5: Schematic of a diblock copolymer molecule (left panel). Each chain is comprised of two distinct chemical species shown as red and blue covalently bonded together. Due to a net unfavourable interaction between the two blocks, phase separation is favourable. But because of the connectivity of the chains the lengthscale to do so is limited which causes a microphase separation (right panel). The in-plane order of the molecules is not a real feature of diblock copolymer liquids, and is only present for clarity of the schematic.

length, the structure is a lamellar phase where stacks of molecules form layers similar to stacks of lipid bilayers. The schematic in the right panel of figure 1.5 shows a lamellar forming diblock copolymer in its phase separated state. Other micro-structures are possible depending on the ratio of the lengths of the two blocks. For example, if one of the blocks is small compared to the other, the microphase separation will favour spheres with the minority block at the centre of the spheres. The experiments done in this thesis on diblock copolymers focus on lamellar forming diblock copolymers where the two blocks have equal length.

For a diblock copolymer, although microphase separation is enthalpically favoured there is an entropic cost associated with the stretching of chains. The equilibrium lamellar spacing L_0, which is the thickness of a bilayer of diblock molecules, is determined by the balance between the enthalpic and entropic contribution to the free energy. At high temperature, the entropic cost becomes more important and the lamellar spacing will decrease. There is a characteristic temperature, the order-disorder transition temperature T_{ODT}, above which the entropic cost dominates and there is

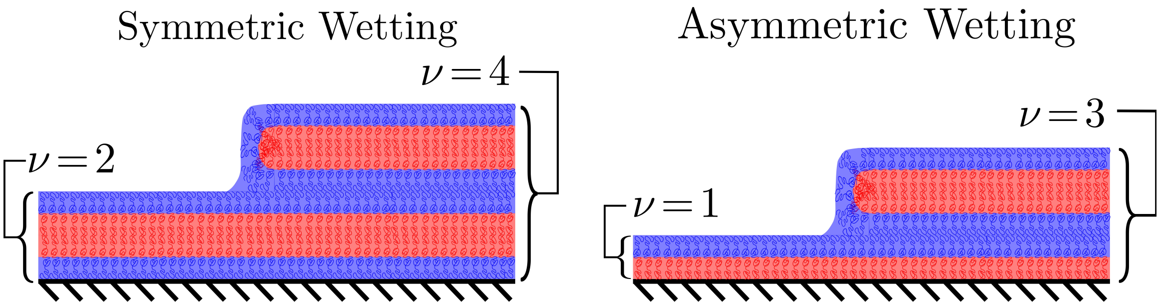

Figure 1.6: Schematic of a diblock copolymer film on a substrate with a symmetric (left panel) and asymmetric (right panel) wetting condition. In the symmetric wetting case, the same block has preferential interactions with both interfaces, and as a result it is energetically favourable to have even numbers of molecular monolayers $\nu = \{2, 4, 6, \dots\}$. On the other hand, if one block has a preferential interaction with the substrate while the other has an affinity for the air, then odd numbers of monolayers $\nu = \{1, 3, 5, \dots\}$ are favoured.

no static microphase separated structure.

When a diblock copolymer is confined to a thin film there are some added features. Typically, there is a energetic preference for one of the two chemical blocks at each interface. This makes it energetically favourable for the film to form discrete numbers of layers stacked parallel to the interfaces. If both interfaces favour interaction with the same block (symmetric wetting condition), the film will form even numbers of molecular monolayers ν. On the other hand, if the two interfaces prefer different blocks (asymmetric wetting condition), films with an odd number of molecular monolayers are energetically favourable. The two different wetting conditions are shown schematically in figure 1.6.

As a result of the interfacial interactions, a diblock copolymer film will have a free energy that strongly depends on film thickness. In the next section the free energy of a polymer film will be examined in more detail for both a polymer with a single molecular species (a homopolymer), and a diblock copolymer.

1.3 Equilibrium state of the fluid

The free energy of a thin film can be divided into two parts. First, there is a bulk free energy cost of creating interface, which is the surface tension. Second, as a film

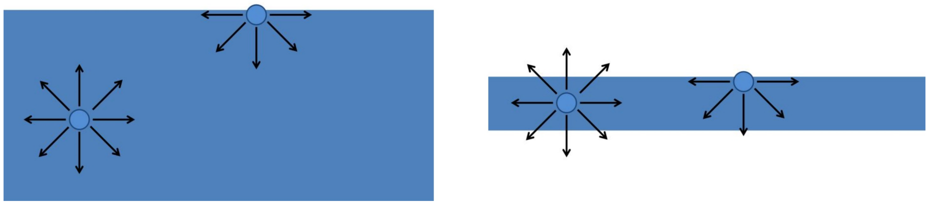

Figure 1.7: Schematic of two fluid films of different thickness. The film on the left has a bulk-like thickness, where the free energy cost of creating interface is the bulk surface tension. A molecule at the top interface has fewer interactions than the one in the bulk of the fluid leading to the free energy cost of creating interface. The film on the right has a free energy cost to create interface that is different than the bulk. The characteristic lengthscale of interaction (shown schematically as the black arrows) is larger than the film thickness. In this case the free energy cost per unit area is the surface tension plus an additional contribution from the effective interface potential.

becomes confined, there are modifications to this free energy which are described by the effective interface potential. These two effects will be described below.

1.3.1 Surface tension

Surface tension is an energy cost per unit area of a fluid interface which is the result of molecules at the interface having fewer interactions than those in the bulk [17]. For a thin film the surface-to-volume ratio increases, which increases the relative contribution of surface tension to the free energy. The left panel of figure 1.7 shows a pictorial representation of a molecule at the interface compared to one in the bulk. Due to a difference in the interactions felt by each of the two cases, this gives a free energy cost of creating interface: the surface tension γ. The surface tension is given in terms of the derivative of the Helmholtz free energy $\mathcal{F}$ with respect to the change in surface area A at constant temperature, volume and number of particles:

$$\gamma = \left(\frac{\partial \mathcal{F}}{\partial A}\right)_{T,V,N}. \tag{1.22}$$

The surface tension of a liquid depends on the chemical properties of the material, temperature and for polymeric liquids, the molecular weight. The temperature dependence of the surface tension is well-described by a linear approximation for most polymeric liquids in experimentally accessible temperature ranges. Thus,

$$\gamma(T) = \gamma_0 + \frac{d\gamma}{dT}T, \tag{1.23}$$

where the material dependent parameters γ_0 and $\frac{d\gamma}{dT}$ are given in table 1.2 for four common polymers. Three of the polymers are studied in this thesis: PS, P2VP, and PMMA. The other polymer, poly(dimethylsiloxane) (PDMS), has a particularly low surface tension. There is a low energy cost to creating extra surface area for this liquid, which results in PDMS spreading to coat many surfaces. This makes PDMS well suited to its use as a coating in vacuum applications. On the other hand, as a result of the higher surface tensions of PS, P2VP, and PMMA, there are many surfaces these fluids do not coat. This leads to dewetting which will be discussed in section 1.3.4.

Table 1.2: Temperature dependent surface tension parameters for common polymeric liquids [18–20] as defined in Eq. (1.23).

	$\gamma_0 = \gamma(T = 0°\text{C})$ (mJ/m^2)	$\frac{d\gamma}{dT}$ (mJ/m °C)
PS	41.5	-0.068
P2VP	46.7	-0.063
PMMA	42.1	-0.072
PDMS	22.7	-0.067

The surface tension of all four of the polymers listed in table 1.2 have a similar temperature dependence. The surface tension weakly decreases as temperature is increased. Physically, the cohesive forces between molecules become effectively weaker at higher temperature, which results in less of a free energy cost for having a molecule at the interface.

The surface tension of polymeric liquids also depends on the number average molecular weight M_n. For the same material at the same temperature, a higher molecular weight gives a larger surface tension. Two different empirical relations have been used to describe $\gamma(M_n)$, both of which are a power law in M_n of the form:

$$\gamma(M_n, T) = \gamma(T) - \frac{k_\gamma}{M_n^\beta}, \tag{1.24}$$

where $\gamma(T)$ is the extrapolated surface tension at large molecular weight, and k_γ is a constant that depends on the polymer. The exponent β is different for each of the two empirical models. The first is derived from a free-volume argument [21] and predicts $\beta = 2/3$. The second empirical relation can be derived from a difference between chain ends and the backbone of the polymer chains [22], and gives $\beta = 1$. Experimentally, high molecular weight data is best described by $\gamma \propto M_n^{-1}$, while low molecular weight data is better fit by $\gamma \propto M_n^{-2/3}$ [23]. Recently, a self-consistent field theory study has shown that the two different scalings arise from a complete exclusion of the polymer from the coexisting phase across the interface at intermediate molecular weight [24].

The temperature dependence of the surface tension ($\frac{d\gamma}{dT}$) from equation (1.23) is nearly independent of molecular weight [25], and so to a good approximation the temperature dependence and molecular weight dependence can be separated, as it has been in equation (1.24).

1.3.2 Effective interface potential

Up to this point in the discussion of the free energy of a thin film, we have only considered the bulk surface tension. This works well for films which have a thickness larger than the characteristic lengthscale of molecular interactions. However, when the film is thin enough that the molecular interaction lengthscale is smaller than the overall film thickness, the free energy cost per unit area of creating interface is modified from its bulk value of the surface tension. This situation is shown schematically in figure 1.7. The film on the right is thin enough such that the cost of having a molecule at the interface is different than the thick, bulk-like film on the left. In other words, in order to describe the free energy of the confined film per unit area Δf, there is a modification from the bulk surface tension value as:

$$\Delta f = \gamma + \Phi, \tag{1.25}$$

where Φ is the effective interface potential [26]. The effective interface potential depends on the fluid as well as interactions with the surrounding materials. For example, the effective interface potential has been shown to depend on the interactions of the fluid with a solid substrate [27]. The effective interface potential also depends on film thickness. Another way to think about the effective interface potential is as a difference between the free energy cost per unit area of creating interface $f(h)$ for a film of thickness h compared to an infinitely thick film:

$$\Phi(h) = f(h) - f(h \to \infty). \tag{1.26}$$

In this thesis three combinations of polymer films and substrates were investigated: PS films on a silicon substrate with a native oxide layer (SiOx/Si), PS-P2VP diblock copolymer films on SiOx/Si, and freely-suspended PS films with no substrate (see table 1.3 for a summary). The effective interface potential for each of these three systems will be discussed in turn.

Table 1.3: The combinations of polymer films and substrates used in this thesis, along with their corresponding reference to the papers in Chapter 3.

Polymer	Substrate	Paper #
PS homopolymer	SiOx/Si	III, IV
PS-P2VP diblock copolymer	SiOx/Si	I, II
PS homopolymer	none (freestanding)	IV, V

PS homopolymer on SiOx/Si

In figure 1.8, the effective interface potential of a PS film on a silicon substrate is plotted against the thickness of the PS film (blue curve). For thick films, the effective interface potential goes to zero, meaning that there is no modification of the free energy cost per unit area. As the film thickness is decreased the free energy cost is modified.

To understand this modification in homopolymer thin films, there are two competing effects to consider, van der Waals interactions and short-ranged steric repulsion [30]. The effective interface potential can be written as a sum of these two contributions as [28]

$$\Phi(h) = \Phi_{\mathrm{vdW}}(h) + \Phi_{\mathrm{steric}}(h). \tag{1.27}$$

The steric repulsion term is due to the repulsion of electron orbitals, which are important for films with sub-nanometre thickness and are typically described by a

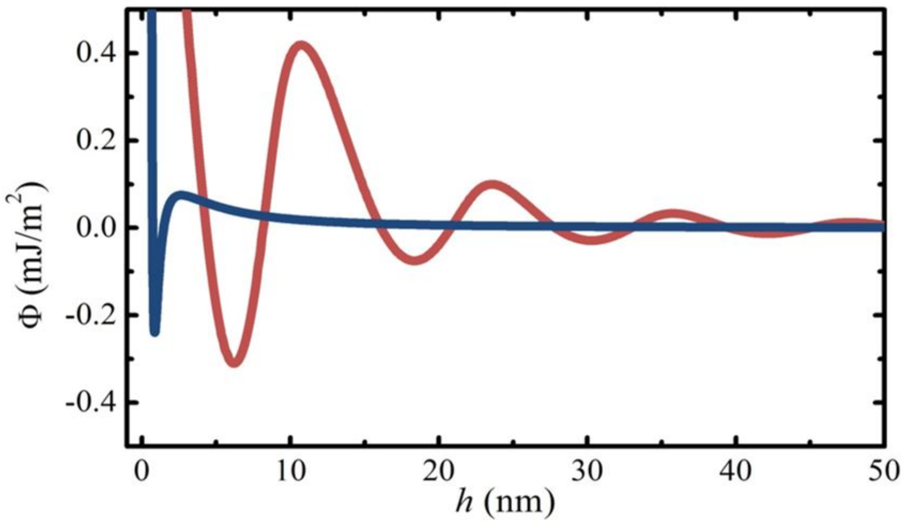

Figure 1.8: The effective interface potential plotted as a function of film thickness for a PS homopolymer film on a native oxide silicon substrate [28] (blue), and for a PS-P2VP diblock copolymer film on a native oxide silicon substrate [29]. The molecular order in the diblock film which is induced by the substrate causes an oscillatory potential with a long range decay in amplitude.

h^{-8} power law in the effective interface potential [28]

$$\Phi_{\mathrm{steric}}(h) = \frac{C}{h^8}, \tag{1.28}$$

with C a positive constant. For PS on an oxidized silicon wafer C was experimentally determined to be $C = 1.8 \times 10^{-77}\,\mathrm{J\,m}$ [31].

On the other hand, van der Waals interactions describe the molecular attraction between molecules which are not due to covalent or ionic bond formation, nor are due to electrostatic interactions. They are the result the interactions between the fluctuating dipole moment of molecules [32]. When two surfaces are brought into close proximity, there is a net attraction between each molecule from the one surface and all the molecules of the other surface. For two flat, infinite surfaces parallel to one another at a distance d, the free energy potential is given by [28, 33, 34]:

$$\Phi_{\mathrm{vdW}} = \frac{-A}{12\pi d^2}, \tag{1.29}$$

where A is the Hamaker constant of the system, and is determined by the indices of refraction of the liquid and the surrounding media. For a polymeric liquid with dielectric constant ϵ_{p} and index of refraction n_{p} on a substrate with dielectric constant ϵ_{sub} and index of refraction n_{sub}, the Hamaker constant is given by:

$$\begin{aligned} A \approx \frac{3k_BT}{4}\left(\frac{1-\epsilon_{\mathrm{p}}}{1+\epsilon_{\mathrm{p}}}\right)\left(\frac{\epsilon_{\mathrm{sub}}-\epsilon_{\mathrm{p}}}{\epsilon_{\mathrm{sub}}+\epsilon_{\mathrm{p}}}\right) + \\ \frac{3h\nu_e}{8\sqrt{2}}\frac{\left(1-n_{\mathrm{p}}^2\right)\left(n_{\mathrm{sub}}^2-n_{\mathrm{p}}^2\right)}{\sqrt{(1+n_{\mathrm{p}}^2)}\sqrt{(n_{\mathrm{sub}}^2+n_{\mathrm{p}}^2)}\left[\sqrt{(1+n_{\mathrm{p}}^2)}+\sqrt{(n_{\mathrm{sub}}^2+n_{\mathrm{p}}^2)}\right]}, \end{aligned} \tag{1.30}$$

which gives $A_{\mathrm{Si}} = -2.2\times10^{-19}$ J for PS on a silicon substrate, and $A_{\mathrm{SiOx}} = 1.8\times10^{-20}$ J for PS on an oxidized silicon substrate [28]. Here the electronic absorption energy is given as $h\nu_e \approx 2\times10^{-18}$ J and $k_BT \approx 7\times10^{-21}$ J. The opposite signs of A_{Si} and A_{SiOx}, indicate that the silicon substrate favours thicker PS films, while the oxidized silicon favours thinner PS films. In other words, for PS on silicon wetting is favourable, while PS on oxidized silicon dewetting is favoured.

The substrates used in the experiments contained in this thesis are a mix of silicon and oxidized silicon. These substrates typically have 1.7 nm of oxidized silicon coating approximately 1 mm of crystalline $< 100 >$ silicon. In that case, the van der Waals interaction potential depends on the Hamaker constants of both materials as [28]:

$$\Phi_{vdW}(h) = -\frac{A_{\mathrm{SiOx}}}{12\pi h^2} + \frac{A_{\mathrm{SiOx}} - A_{\mathrm{Si}}}{12\pi\left(h + 1.7\,\mathrm{nm}\right)^2}. \tag{1.31}$$

PS-P2VP diblock copolymer on SiOx/Si

The free energy cost of confining a lamellar-forming diblock copolymer is markedly different than the homopolymer case. The red curve in figure 1.8 shows the effective interface potential of a PS-P2VP diblock copolymer film above the order-disorder transition temperature, but with phase separation locally induced by favourable interactions of P2VP with the SiOx/Si substrate and PS with the air [29]. The effective interface potential is calculated using self-consistent field theory as has been done previously [35]. Self-consistent field theory (SCFT) is a mean field theory for determining the equilibrium state and free energy of a system. For polymer systems, SCFT treats the interactions between polymer chains as an interaction between a single chain and an effective field created by other polymer chains [36]. For the case of a diblock copolymer film of a fixed thickness, the spatial density profiles of each of the two blocks is calculated to get the effective field. Assuming an initial field, a modified diffusion equation can be solved to give the density profiles. From those profiles a new effective field is calculated, and the process iterated until a self-consistent solution is reached. The equilibrium density profile of the two blocks is the one which satisfies the self-consistency condition. From that equilibrium state, the equilibrium free energy can be calculated. This process is repeated for many different film thicknesses to give the free energy as a function of film thickness. The effective interface potential is then determined from the difference in free energy compared to a film approaching the limiting value at infinite thickness, as in equation 1.26.

One notable feature from figure 1.8 is that the potential energy is larger for the diblock copolymer compared to the PS homopolymer on SiOx/Si. The contribution to the effective interface potential from Φ_{vdW} or Φ_{steric} is small compared to the free energy contributions from the connectivity and resulting phase separation of diblock molecules $\Phi_{\text{molecular}}$ [35].

The effective interface potential of the diblock is a decaying, oscillatory function of the film thickness. The decaying component can be understood as a competition between a bulk disordered phase and the surface induced ordering. For thin films, the two interfaces are close enough that the film thickness is smaller than the characteristic lengthscale over which the order decays. By phase separating at the interfaces, this satisfies the boundary conditions, which causes a reduction in the free energy. But since the thin film does not have much material, the unfavourable segregation away from the interfaces is minimized. On the other hand, the segregation induced by the interfaces in thick films is able to decay into the centre of the film. Since this segregation away from the interface is energetically unfavourable, this cancels out the energy reduction caused by segregation and leads to the decay of the free energy with film thickness.

The oscillatory component of the effective interface potential is due to the competition between the entropic cost of chains stretching and the enthalpic interaction of the two chemical blocks. This sets an equilibrium lamellar spacing of the layers in the film. When the film thickness matches the lamellar spacing of the diblock molecules, while also simultaneously satisfying the interfacial interactions, there is a minimum in the free energy. The difference between successive minimums in figure 1.8 is the equilibrium lamellar spacing $L_0 \approx 13\,\mathrm{nm}$.

PS homopolymer with no substrate (freestanding)

For the final system studied in this thesis, a PS homopolymer which is freely-suspended, the effective interface potential is similar to that of the PS homopolymer supported on a SiOx/Si substrate. The steric repulsion should be similar, although this has never been experimentally determined. The van der Waals interaction is

$$\Phi_{vdW}(h) = \frac{-A_{\mathrm{PS}}}{12\pi h^2}, \tag{1.32}$$

where the Hamaker constant for PS with two air interfaces can be calculated from equation 1.30 by setting $n_{\mathrm{sub}} = 1$,

$$A_{\mathrm{PS}} \approx \frac{3k_BT}{4}\left(\frac{1-\epsilon_{\mathrm{p}}^2}{1+\epsilon_{\mathrm{p}}^2}\right)^2 + \frac{3h\nu_e}{16\sqrt{2}}\frac{\left(1-n_{\mathrm{p}}^2\right)^2}{\left(1+n_{\mathrm{p}}^2\right)^{3/2}}. \tag{1.33}$$

For a PS film surrounded by air the Hamaker constant is $A_{\mathrm{PS}} = 6.5 \times 10^{-20}\,\mathrm{J}$ [33]. The positive Hamaker constant means the film is unstable. The Hamaker constant is larger for the freestanding PS film compared to the SiOx/Si supported PS film. This means that a freestanding PS film is less stable than a PS film supported by a SiOx/Si substrate.

1.3.3 Total free energy

Now we can put together the contributions to free energy from both surface tension and the effective interface potential. For the surface tension, we need to consider the total surface area of the film given by the surface $h(x, y)$. This gives the overall free energy $\mathcal{F}$ as a function of film thickness $h(x, y)$

$$\mathcal{F}(h) = \int\int dx\, dy \Bigg[\left(\gamma_0 + \frac{d\gamma}{dT}T - \frac{k_\gamma}{M_n} \right) \sqrt{1 + (\nabla h)^2} \\ + \Phi_{vdW}(h) + \Phi_{\text{steric}}(h) + \Phi_{\text{molecular}}(h) \Bigg]. \quad (1.34)$$

Writing $\gamma = \gamma_0 + \frac{d\gamma}{dT}T - \frac{k_\gamma}{M_n}$ and $\Phi(h) = \Phi_{vdW}(h) + \Phi_{\text{steric}}(h) + \Phi_{\text{molecular}}(h)$, and taking the limit of small gradients in h, the difference in free energy per unit area compared to a flat film simplifies to

$$\Delta f(h) = \frac{\gamma}{2}(\nabla h)^2 + \Phi(h). \quad (1.35)$$

From the total free energy of the system, the pressure which drives flow can be derived [5, 37]. A clear and instructive derivation is presented in reference [37], but here only the final expression for the pressure is quoted:

$$p(x, y) = -\gamma \nabla^2 h(x, y) + \Phi'(h(x, y)). \quad (1.36)$$

In both the free energy per unit area and pressure, there is a great deal of complexity buried in the effective interface potential. In particular, the stability of a film greatly depends on the effective interface potential, as discussed in the next section.

1.3.4 Stability and dewetting of a thin liquid film

Complete, partial, and pseudopartial wetting

One interesting consequence of equation 1.36 is that for a film with uniform thickness, $h(x, y) = h_0$, the pressure is only given by the derivative of the effective interface potential $p = \Phi'(h_0)$. Depending on the film thickness dependence of the effective interface potential, the fate of a film can differ. If the derivative of the effective interface potential is negative, then the film is driven to become thinner. Since polymeric liquids are for the most part incompressible, for one region of the film to become thinner another region has to becomes thicker than its initial thickness h_0.

Three different wetting regimes are shown in figure 1.9. The important distinction

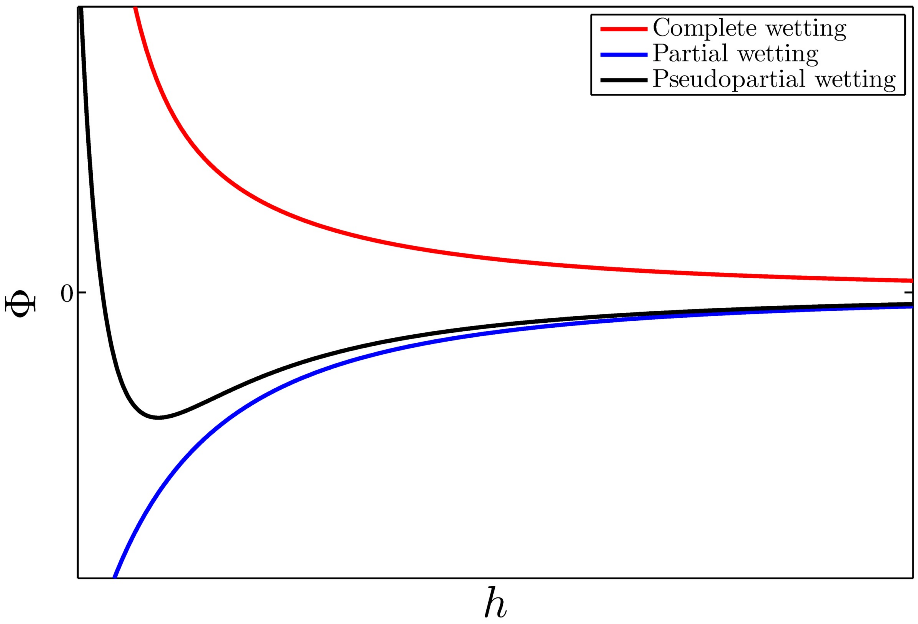

Figure 1.9: The effective interface potential for complete, partial, and pseudopartial wetting.

between the three regimes is the concavity of the effective interface potential. To understand why the concavity of Φ is important, consider the free energy cost of creating a thicker region with $h_{\text{thick}} = h_0 + \delta$, and a thicker region $h_{\text{thin}} = h_0 - \delta$. To second order in δ, the effective potential in these two regions is

$$\Phi(h_{\text{thick}}) = \Phi(h_0) + \Phi'(h_0)\delta + \Phi''(h_0)\frac{\delta^2}{2} \tag{1.37}$$

$$\Phi(h_{\text{thin}}) = \Phi(h_0) - \Phi'(h_0)\delta + \Phi''(h_0)\frac{\delta^2}{2}. \tag{1.38}$$

The average free energy of these two regions is

$$\Phi_{\text{avg}}(h_0) = \frac{1}{2}\left(\Phi(h_{\text{thick}}) + \Phi(h_{\text{thin}})\right) = \Phi(h_0) + \frac{1}{2}\Phi''(h_0)\delta^2. \tag{1.39}$$

When $\Phi''(h_0) < 0$, $\Phi_{\text{avg}}(h_0) < \Phi(h_0)$, which means the system can lower the free energy by creating thinner and thicker regions. On the other hand, when $\Phi''(h_0) > 0$, $\Phi_{\text{avg}}(h_0) > \Phi(h_0)$, meaning there is an energetic cost to creating thicker and thinner regions.

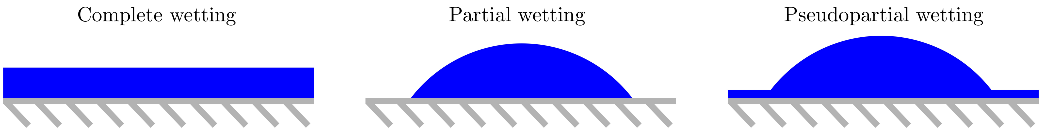

Figure 1.10: Schematic of complete, partial, and pseudopartial wetting.

Returning now to the first of three cases of wetting in figure 1.9, the red curve has $\Phi''(h) > 0$ for all h, which means that there is an energetic cost for a uniform film to create any non-uniform regions. This means a uniform film of any thickness is stable. Conversely, if a drop of fluid is placed on a substrate where the effective potential is described by the red curve, then the free energy can be reduced by the droplet spreading to coat the substrate. In other words, the fluid will completely wet the substrate, which is why this is referred to as the "complete wetting" regime.

The blue curve of figure 1.9 is concave down, with $\Phi''(h) < 0$ for all h. This means that for any uniform film thickness, it is energetically favourable for the spontaneous creation of thinner and thicker regions. Since a film of any thickness is unstable, the film will dewet from the substrate. Alternatively, if a drop of fluid is placed on a dry substrate where the effective interface potential is described by the blue curve, spreading to coat the substrate is not energetically favoured, and the fluid will only partially coat the substrate (hence the "partial wetting" regime).

Finally, the black curve of figure 1.9 describes the effective interface potential for the pseudopartial wetting regime, which has characteristics of both complete wetting and partial wetting. In this case the effective interface potential starts off concave up for thin films, but then switches over to concave down for thicker films. In the pseudopartial wetting regime, a uniform film will dewet, but will leave behind a thin wetted film with thickness h_{min}, which is the film thickness at which the effective interface potential is at a minimum. If a droplet is brought into contact with a dry substrate in the pseudopartial regime, a thin prewetting film will wet the substrate, coexisting with a droplet that only partially covers the substrate. Figure 1.10 schematically shows the equilibrium state of each of the three wetting regimes.

Dewetting

In the previous section, it was shown that a film with an initially uniform thickness can be unstable in the partial or pseudopartial wetting regime. In either case, there are two different mechanisms by which a film can dewet: nucleation of a thin region followed by growth, or spinodal dewetting. Depending on the shape of the effective interface potential and the initial thickness of the film, nucleated or spinodal dewetting can dominate [26]. Consider the two interfacial potentials sketched in figure 1.11. For the unstable film, $\Phi''(h) < 0$ for all h and the film will spontaneously dewet. The dewetting will occur uniformly in the film, which is referred to as spinodal dewetting [38]. Fluctuations with a characteristic wavelength grow in time, which can be described by a linear stability analysis of the equations governing flow (for details see "Linearization" in Section 1.4.2).

In the case of a metastable film, $\Phi''(h) > 0$ for thicker films which means that there will not be a spontaneous dewetting occurring uniformly in the film. However, because the free energy eventually becomes lower at thinner films, it is still energetically favourable for the film to dewet. Dewetting can only occur through a nucleated process. Once a thinner region is nucleated, either through thermal fluctuations (homogeneous nucleation) or from an impurity in the film (heterogeneous nucleation), it is energetically favourable for it to grow [26]. The maximum in the effective interface potential for the metastable film is a free energy barrier to dewetting which has to be overcome by nucleation.

Equilibrium state of dewetted droplets

If the dewetting of a film is allowed to proceed until equilibrium is reached, the film will break up into droplets covering the substrate. When gravity is unimportant, the shape of the droplets can be described by a spherical cap (a section of a sphere created by slicing it with a plane). In this section, an expression for the angle at the edge of a droplet in equilibrium will be derived in terms of the free energy of the system. The pseudopartial wetting case will be considered first, from which the partial wetting case can be derived. This section follows closely the pedagogical derivation presented in reference [39].

Consider a spherical cap droplet shown schematically in figure 1.12 with base

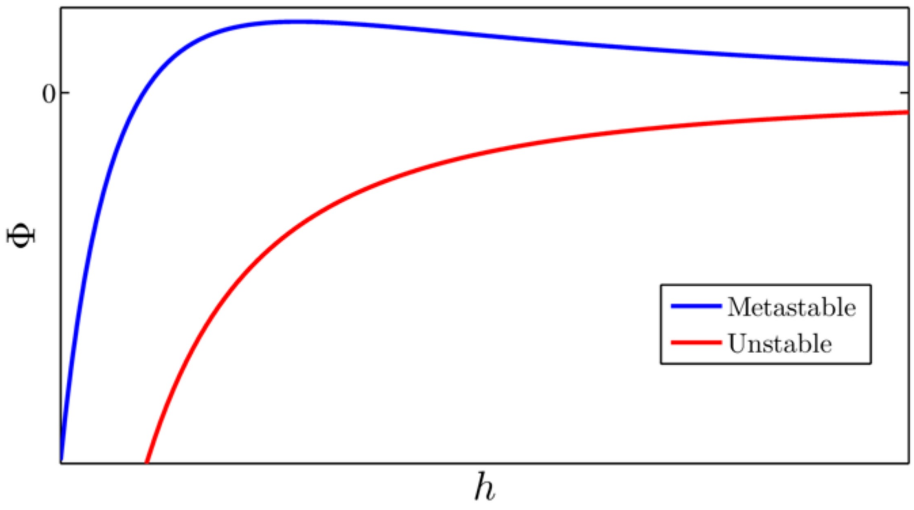

Figure 1.11: The effective interface potential for an unstable and metastable film. For an unstable film, dewetting will occur spontaneously for any film thickness (spinodal dewetting). A metastable film has an energy barrier in the effective interface potential, and dewetting occurs as a nucleated process.

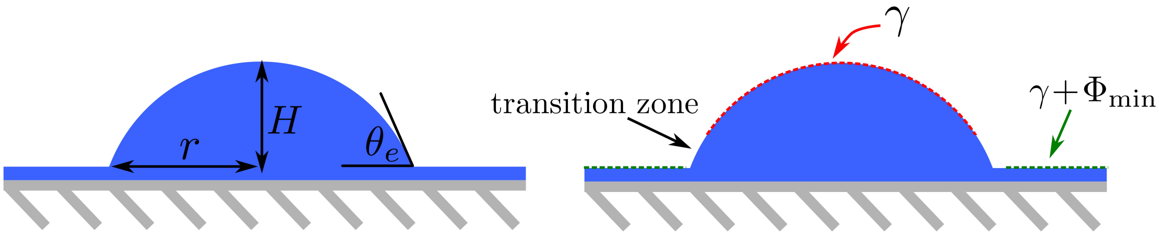

Figure 1.12: Schematic of a partially wetting droplet in equilibrium. The equilibrium geometry of a spherical cap droplet is defined in the left schematic in terms of its maximum height H, base radius r and equilibrium contact angle θ_e. The free energy cost of creating interface can be broken down into three regions. First, a region at the top of the droplet where the surface tension is the only contribution to the energy cost (red dashed line). Second, the wetting layer (green dashed line) where the energy cost is the result of surface tension plus the effective interface potential. Third, a transition zone between these two regions where the energy cost is varying. For a droplet which has a height much larger than the wetting layer thickness, the transition zone makes a relatively small contribution to the overall energy cost and can be ignored.

radius r, maximum height H, and equilibrium contact angle θ_e. If the maximum height of the droplet is much larger than the thickness of the wetting layer, as is typically the case, the free energy cost for creating interface at the top part of the droplet is just the surface tension γ times the total surface area at the top of the droplet A_{surface} [red dashed line in figure 1.12]. On the other hand, regions where there is only a wetting layer and no droplet have a free energy cost per unit area of $\gamma + \Phi_{\text{min}}$ [green dashed lines in figure 1.12]. If the area of the transition zone between the two regions is small, the change in free energy of the system can then be written as

$$d\mathcal{F} = -\left(\gamma + \Phi_{\text{min}}\right) dA_{\text{base}} + \gamma dA_{\text{surface}}, \tag{1.40}$$

where the base area of the droplet is $A_{\text{base}} = \pi r^2$, and $A_{\text{surface}} = \pi r^2 + \pi H^2$. Substituting the differential of these two areas into equation 1.40 gives

$$d\mathcal{F} = -\left(\gamma + \Phi_{\text{min}}\right)\left(2\pi r\, dr\right) + \gamma\left(2\pi r\, dr + 2\pi H\, dH\right). \tag{1.41}$$

The expression for the change in free energy in equation 1.41 depends on both the radius r and height H of the droplet. To proceed, one of these two variables can be eliminated by enforcing a conservation of volume Ω in the droplet. The volume of a spherical cap is:

$$\Omega = \frac{1}{6}\pi H\left(3r^2 + H^2\right), \tag{1.42}$$

and volume conservation implies

$$d\Omega = \pi H r\, dr + \frac{1}{2}\pi\left(r^2 + H^2\right) dH = 0. \tag{1.43}$$

$$\implies dH = -\frac{2Hr\, dr}{r^2 + h^2}. \tag{1.44}$$

Using this expression for dH along with $\cos\theta_e = (r^2 - h^2)/(r^2 + h^2)$ [39] in equation 1.41 gives

$$d\mathcal{F} = 2\pi r\, dr\left(-\gamma - \Phi_{\text{min}} + \gamma\cos\theta_e\right). \tag{1.45}$$

At equilibrium $d\mathcal{F} = 0$, which gives the final expression for the contact angle in terms of the free energy costs per unit area

$$\cos\theta_e = \frac{\Phi_{\text{min}} + \gamma}{\gamma}. \tag{1.46}$$

This equation is valid for the pseudopartial wetting regime where the dewetted droplet coexists with a wetting layer whose thickness matches the minimum in the effective interface potential. The expression for the equilibrium contact angle of a droplet in the partial wetting regime can be found by modifying the Φ_{min} term. For a droplet which does not coexist with a wetting layer, $\Phi_{\text{min}}(h = 0)$ needs to be considered. In the limiting case of no liquid film, the effective interface potential is the difference between the free energy cost for a dry substrate γ_{SV} (the solid-vapour interfacial energy), and the free energy cost for a substrate coated with a bulk film $\gamma + \gamma_{\text{SL}}$ (the surface tension plus the solid-liquid interfacial energy). By letting $\Phi_{\text{min}} = \gamma_{\text{SV}} - (\gamma + \gamma_{\text{SL}})$ in equation 1.46, this yields the Young-Dupré equation describing the equilibrium contact angle of a partially wetting droplet

$$\cos\theta_e = \frac{\gamma_{\text{SV}} - \gamma_{\text{SL}}}{\gamma}. \tag{1.47}$$

For the case of either partial wetting or pseudopartial wetting, the equilibrium contact angle is related in fairly simple terms to the free energy costs per unit area in the system. Thus, an experimental measurement of θ_e is one way to access information about these energy costs. In Paper I of Chapter 3, the equilibrium contact angle of diblock copolymer droplets is measured. Knowing γ and θ_e, Φ_{min} is determined by making use of equation 1.46.

In this section the equilibrium state of a polymer fluid in a thin film has been considered. We will now turn to the dynamics of fluid flow in thin films.

1.4 Flow of polymeric liquids at small lengthscales

We start our description of fluid flow with the Cauchy momentum equation [5], which gives the momentum transport in a continuum system as

$$\rho\frac{\partial\vec{u}}{\partial t} + \rho\vec{u}\cdot\nabla\vec{u} = -\nabla p + \nabla\cdot\overset{\leftrightarrow}{\tau}, \tag{1.48}$$

where $\overset{\leftrightarrow}{\tau}$ is the shear-stress tensor, ρ is the density, and $\vec{u}$ is the velocity of the fluid. For a purely viscous flow, $\overset{\leftrightarrow}{\tau} = \eta\nabla\vec{u}$, and assuming that gravity and inertial forces are small, this leads to Stokes' equations of creeping flow (slow viscous flow) of incompressible fluids

$$\eta\nabla^2\vec{u} = \nabla p \tag{1.49}$$

$$\nabla\cdot\vec{u} = 0 \tag{1.50}$$

Written out explicitly in terms of the three spatial coordinates $\vec{x} = (x, y, z)$ and corresponding velocities $\vec{u} = (u, v, w)$ Stokes' equation is given by

$$\eta\left(\frac{\partial^2 u}{\partial x^2} + \frac{\partial^2 u}{\partial y^2} + \frac{\partial^2 u}{\partial z^2}\right) = \frac{\partial p}{\partial x} \tag{1.51}$$

$$\eta\left(\frac{\partial^2 v}{\partial x^2} + \frac{\partial^2 v}{\partial y^2} + \frac{\partial^2 v}{\partial z^2}\right) = \frac{\partial p}{\partial y} \tag{1.52}$$

$$\eta\left(\frac{\partial^2 w}{\partial x^2} + \frac{\partial^2 w}{\partial y^2} + \frac{\partial^2 w}{\partial z^2}\right) = \frac{\partial p}{\partial z} \tag{1.53}$$

$$\frac{\partial u}{\partial x} + \frac{\partial v}{\partial y} + \frac{\partial w}{\partial z} = 0, \tag{1.54}$$

where z is the direction perpendicular to the plane of the film. At this point, we make the lubrication approximation which assumes that because the film thickness $h(x, y)$ is much smaller than typical horizontal lengthscales, the flow in the z direction can be neglected and $w \approx 0$. For simplicity, the case with $h(x, y) = h(x)$ will be developed, which means $v = \frac{\partial p}{\partial y} = 0$. With these assumptions Stokes' equations become

$$\eta\left(\frac{\partial^2 u}{\partial x^2} + \frac{\partial^2 u}{\partial z^2}\right) = \frac{\partial p}{\partial x} \tag{1.55}$$

$$\frac{\partial p}{\partial z} \approx 0 \implies p(x, z) = p(x) \tag{1.56}$$

$$\frac{\partial u}{\partial x} = -\frac{\partial w}{\partial z}. \tag{1.57}$$

We will use equations 1.55-1.57 to develop a differential equation to describe the height profile $h(\vec{x}, t)$ in each of the following flow geometries studied in this thesis: 2D flow on a substrate, 2D flow in a freestanding film, and 3D axisymmetric flow

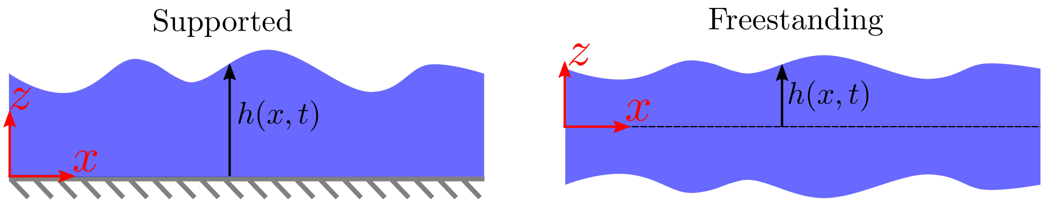

Figure 1.13: Schematic of a supported film (left) and freestanding film (right). For the supported film, the z axis is perpendicular to the film substrate (the substrate is semi-infinite and depicted in grey), and $z = 0$ at the liquid-solid interface. For the freestanding film, the pressure equilibrates rapidly in the vertical direction which causes an axis of symmetry to develop in the film (shown as the dashed black line). The z axis in this case is perpendicular to the axis of symmetry, and $z = 0$ at the axis of symmetry. In both cases the film thickness profile is defined by $z = h(x,t)$.

on a substrate. The boundary conditions for a supported film versus a freestanding film are different, which leads to a non-trivial difference in the differential equation describing thin film flow. So before proceeding, the different boundary conditions on a film will be examined.

1.4.1 Boundary conditions

Figure 1.13 shows a schematic of a supported film (left) and freestanding film (right) defining the coordinate system used. For the supported film $z = 0$ corresponds to the liquid-solid interface, while $z = h(x,t)$ is the air interface. For the freestanding film, there are two air interfaces. Because the vertical lengthscales are much smaller than the horizontal lengthscale and the pressure is independent of z, the freestanding film establishes the mid-plane of the film as a plane of symmetry. This plane defines $z = 0$ for the freestanding case.

For the supported film, there is a no shear boundary condition at the liquid-air interface. This gives

$$\frac{\partial u}{\partial z} = 0, \qquad \text{at } z = h(x,t). \tag{1.58}$$

The boundary condition at the substrate $z = 0$ depends on the details of the molecular interactions between the liquid at the solid. For many liquid-solid interfaces these interactions lead to a large frictional coefficient, which means that the horizontal velocity of the fluid goes to zero at the substrate

$$u = 0, \qquad \text{at } z = 0 \quad \text{(no-slip)}. \tag{1.59}$$

On the other hand, for liquid-solid combinations which have a lower interfacial friction, liquid molecules at the interface can slide and $u(z = 0) \neq 0$. This molecular sliding is referred to as slip. A way to parameterize the effect of slip is through the slip length b. The slip length is defined by the slip boundary condition as

$$u = b\frac{\partial u}{\partial z}, \qquad \text{at } z = 0 \quad \text{(slip)}. \tag{1.60}$$

The no-slip boundary condition is recovered by setting the slip length to zero ($b = 0$ in equation 1.60).

The velocity profiles near the liquid-solid interface are shown in figure 1.14 for three cases: no-slip ($b = 0$), weak-slip ($b << h$), and strong-slip ($b \to \infty$). In the strong-slip regime, the horizontal velocity profile is nearly constant along the thickness of the film (known as plug flow). In the weak-slip and no-slip regimes, the horizontal velocity profile changes substantially along the thickness of the film. This difference between the strong-slip compared to both the weak and no-slip regimes is important for determining the relative importance of the two terms on the left hand side of equation 1.55. For the no-slip and weak-slip case, because the horizontal gradients are much smaller than the vertical gradients

$$\frac{\partial^2 u}{\partial x^2} << \frac{\partial^2 u}{\partial z^2}, \tag{1.61}$$

and equation 1.55 becomes

$$\eta\frac{\partial^2 u}{\partial z^2} = \frac{\partial p}{\partial x} \quad \text{(no-slip and weak-slip)}. \tag{1.62}$$

The strong-slip case is more complicated and requires a careful analysis of an expansion of Stokes' equations and boundary conditions in terms of the ratio of vertical to horizontal characteristic lengthscales, which leads to two coupled non-linear differential equations [40]. In what follows here, for viscous flow on a substrate only the no-slip and weak-slip regime will be considered.

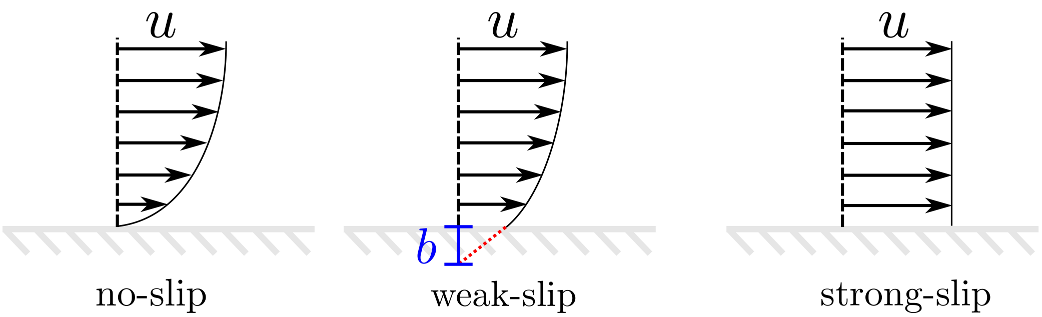

Figure 1.14: Horizontal velocity profiles for no-slip, weak-slip, and strong-slip boundary conditions. For the no-slip case, $u = 0$ at the liquid-solid interface. In the weak-slip regime the horizontal velocity is non-zero at the liquid-solid interface. The slip length b (shown in blue) is defined by equation 1.60 and is the extrapolation of the slope $\frac{\partial u}{\partial z}$ at $z = 0$ to $u = 0$ as depicted by the red dotted line. In the strong-slip regime, $b \to \infty$ and there is no change in the horizontal velocity along the thickness of the film.

In a freestanding film, there are two no shear boundary conditions at the liquid-air interfaces

$$\frac{\partial u}{\partial z} = 0, \qquad \text{at } z = \pm h(x,t). \tag{1.63}$$

As it is in the strong-slip case, the horizontal velocity profile is also constant along the thickness of the film in the freestanding case. Since the interfacial friction is zero, the flow profile in a freestanding film is an ideal plug flow with $\frac{\partial u}{\partial z} = 0$. Therefore, in the freestanding case, equation 1.55 reduces to

$$\eta \frac{\partial^2 u}{\partial x^2} = \frac{\partial p}{\partial x} \qquad \text{(freestanding)}. \tag{1.64}$$

With the effect of the boundary conditions in mind, differential equations to describe the variation of the height profile will now be developed: first for supported films in the no-slip or weak-slip regime, and second for a freestanding film.

1.4.2 2D flow on a substrate

For flow on a substrate, the horizontal velocity can be found by integrating 1.62 twice with respect to z, which gives

$$\eta u = \frac{\partial p}{\partial x}\frac{z^2}{2} + C_1 z + C_2, \tag{1.65}$$

where C_1 and C_2 are constants of integration which depend on the boundary conditions. Using the boundary condition at $z = 0$ from equation 1.60 gives $C_2 = bC_1$. Applying the liquid-air boundary condition of equation 1.58 yields the horizontal velocity of the film

$$u(x, z, t) = \frac{1}{\eta}\frac{\partial p}{\partial x}\left(\frac{z^2}{2} - h(z+b)\right). \tag{1.66}$$

The continuity condition means that the flux $Q = \int_0^h u\,dz$ is related to the film thickness by $\frac{\partial h}{\partial t} = \frac{-\partial Q}{\partial x}$. Using continuity gives the time evolution of the film thickness profile as

$$\frac{\partial h}{\partial t} = \frac{\partial}{\partial x}\left[\frac{1}{\eta}\frac{\partial p}{\partial x}\left(\frac{h^3}{3} + bh^2\right)\right]. \tag{1.67}$$

Finally, by using the pressure derived from the interfacial free energy given by equation 1.36, this gives the 2D supported thin film equation:

$$\eta\frac{\partial h}{\partial t} = \frac{\partial}{\partial x}\left[\left(\frac{h^3}{3} + bh^2\right)\left(-\gamma\frac{\partial^3 h}{\partial x^3} + \frac{\partial \Phi'(h)}{\partial x}\right)\right]. \tag{1.68}$$

This nonlinear differential equation includes both the effect of weak-slip in the term bh^2, and the effective interface potential in the term $\frac{\partial \Phi'(h)}{\partial x}$. By setting b and Φ equal to zero, this equation reduces to the more commonly used thin film equation for capillary driven flow on a no-slip substrate [41, 42].

$$\frac{\partial h}{\partial t} = \frac{-\gamma}{3\eta}\frac{\partial}{\partial x}\left(h^3\frac{\partial^3 h}{\partial x^3}\right). \tag{1.69}$$

Self-similarity

There is a special feature of the 2D thin film equation with $\Phi = 0$: the existence of self-similar solutions. For equation 1.68 with no effective interface potential, there exist solutions $h(x, t)$ that depend on x and t only through the ratio of $x/t^{1/4}$ [43].

This can be demonstrated by letting $h(x,t) = f(u)$, with $u = x/t^{1/4}$, and making this substitution for h in equation 1.68. This gives

$$\frac{uf'}{4} = \frac{\gamma}{\eta}\left[\left(\frac{f^3}{3} + bf^2\right)f'''\right]', \tag{1.70}$$

which only contains the variables f, u, derivatives of f with respect to u, and constants. Since it does not contain any explicit dependence on h, x, or t, there exist solutions to equation 1.68 of the form $h(x,t) = f(u)$ subject to the constraint given by equation 1.70. Self-similarity is not only an interesting mathematical concept, but also allows robust experimental measurements of flow as will be detailed in Section 1.5.1.

Linearization

Knowing the film thickness profile at a given time t_1, $h(x,t_1)$, the profile can be calculated at a later time $h(x,t_2)$ by numerically iterating the differential equation subject to a given set of boundary conditions [42]. To make progress analytically, one can look at small amplitude perturbations from a film of thickness h_0. The profile can be written as $h(x,t) = h_0 + \delta(x,t)$, with $\frac{\delta(x,t)}{h_0} << 1$. Expanding equation 1.68 in terms of δ gives

$$\begin{aligned}\eta\frac{\partial\delta}{\partial t} = \frac{\partial\delta}{\partial x}\left[\left(h_0^2 + 2bh_0\right) + 2\left(h_0 + b\right)\delta + \delta^2\right] \times \left[-\gamma\frac{\partial^3\delta}{\partial x^3} + \frac{\partial\delta}{\partial x}\sum_{n=1}^{\infty} n\Phi^{(n+1)}(h_0)\delta^{n-1}\right] \\ + \left[\left(\frac{h_0^3}{3} + bh_0^2\right) + \left(h_0^2 + 2bh_0\right)\delta + \left(h_0 + b\right)\delta^2 + \frac{\delta^3}{3}\right] \times \\ \left[-\gamma\frac{\partial\delta^4}{\partial x^4} + \sum_{n=1}^{\infty}\left[\frac{\partial^2\delta}{\partial x^2}n\Phi^{(n+1)}(h_0) + \left(\frac{\partial\delta}{\partial x}\right)^2(n+1)\,n\Phi^{(n+2)}(h_0)\right]\delta^{n-1}\right],\end{aligned} \tag{1.71}$$

where $\Phi^{(n)}(h_0)$ is the nth derivative of $\Phi(h)$ evaluated at $h = h_0$. This infinite series is still an exact series expansion of the 2D supported thin film equation. Taking terms first order in δ

$$\eta\frac{\partial\delta}{\partial t} = \left(\frac{h_0^3}{3} + bh_0^2\right)\left(-\gamma\frac{\partial^4\delta}{\partial x^4} + \frac{\partial^2\delta}{\partial x^2}\Phi''(h_0)\right), \tag{1.72}$$

gives the linearized supported thin film equation. One way to proceed from equation 1.72 is by seeking solutions of the form $\delta(x,t) = \delta_0 e^{ikx+\omega t}$ to find the dispersion relation. Putting this solution into equation 1.72 gives the frequency ω in terms of the wave vector k as

$$\omega = -\frac{k^2}{\eta}\left(\frac{h_0^3}{3} + bh_0^2\right)\left(\gamma k^2 + \Phi''(h_0)\right). \tag{1.73}$$

The dispersion relation gives some important physical insight into the dynamics described by the linearized 2D thin film equation (Eq. 1.72). For all k such that $\omega(k) < 0$, this describes decaying modes in the film. If a film with thickness h_0 is made with a small sinusoidal perturbation of wavelength $\lambda = 2\pi/k$ corresponding to a decaying mode, the perturbation will relax back towards a uniform film with a characteristic timescale $\tau = \omega^{-1}$. However, for wave vectors with $\omega(k) > 0$, these modes are unstable. Instead of relaxing towards a flat film, any perturbation with an unstable mode will grow. It is instructive to look at a normalized version of equation 1.73 by letting $\beta = \frac{\gamma}{\eta}\left(h_0^3/3 + bh_0^2\right)$ and $\psi = \frac{\Phi''(h_0)}{\gamma}$, which allows the dispersion relation to be written as

$$\hat{\Omega} = -\beta\left(\hat{K}^4 + \psi\hat{K}^2\right). \tag{1.74}$$

Figure 1.15 shows the normalized dispersion relation plotted for $\beta = 1$ and for various values of ψ. The parameter ψ gives the relative contribution of the effective interface potential. For $\psi = 0$ (black curve) the curvature of the interface potential is zero, and $\hat{\Omega} < 0$ for all $\hat{K}$ meaning that the film is stable. Since $\psi = 0$ corresponds to the case of purely surface tension acting as the driving force, a stable film is to be expected. Stable films are also found for $\psi > 0$. This corresponds to the case where the effective interface potential is concave up, meaning any variations in film thickness are energetically unfavourable. On the other hand, when the effective interface potential is concave down, there is a band of modes $\hat{K} \in (0, \sqrt{-\psi})$ where $\psi < 0$ (red curves). These unstable modes drive dewetting. The peak in the dispersion relation can be found by setting $\frac{\partial\hat{\Omega}}{\partial\hat{K}} = 0$, which gives the characteristic fastest growing mode $\hat{K}^* = \sqrt{-\psi/2}$.

Translating back to the variables used in equation 1.73, when $\Phi''(h_0) < 0$ there is a band of unstable modes which will can cause the film to dewet. A fastest growing

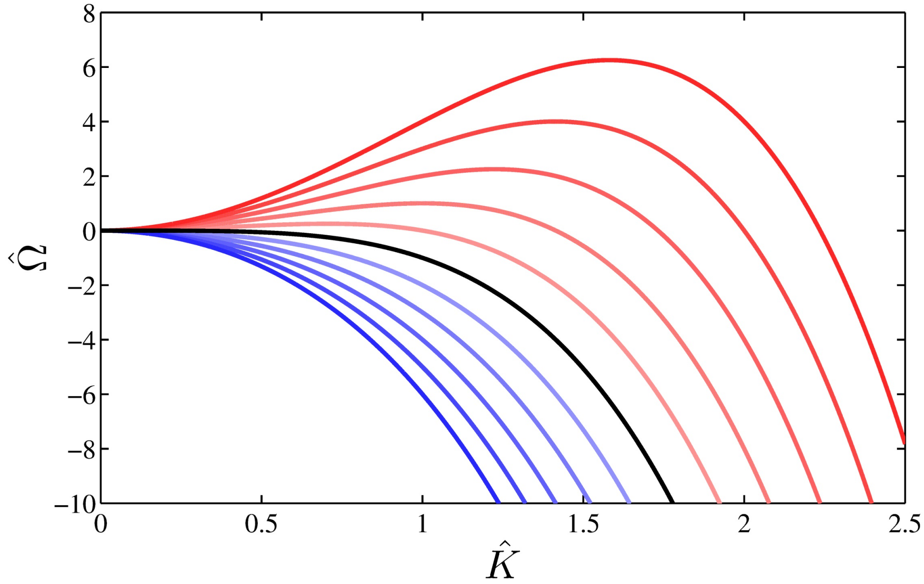

Figure 1.15: Normalized dispersion relation for the linearized thin film equation (Eq. 1.73). Plotted is the function $\hat{\Omega} = -\hat{K}^4 - \psi\hat{K}^2$, where ψ gives the relative contribution of the effective interface potential. From bottom to top $\psi = \{5, 4, 3, 2, 1\}$ (blue curves), $\psi = 0$ (black curve), and $\psi = \{-1, -2, -3, -4, -5\}$ (red curves). As the effective interface potential becomes negative a band of unstable modes emerges where $\hat{\Omega}(\hat{K}) > 0$. These unstable modes drive the film towards dewetting.

mode is given by the peak in the dispersion relation $k^* = \sqrt{-\Phi''(h_0)/2\gamma}$ which selects a characteristic wavelength $\lambda^* = 2\pi/k^* = 2\pi\sqrt{2\gamma/\Phi''(h_0)}$. This mode grows with a characteristic time $\tau^* = \omega^{*-1}$ as

$$\tau^* = \frac{4\eta}{\gamma}\left(\frac{h_0^3}{3} + bh_0^2\right)^{-1}\left(\frac{\gamma}{\Phi''(h_0)}\right)^2. \tag{1.75}$$

There is one other tunable parameter in the normalized dispersion relation of equation 1.74. Although the characteristic mode K^* is independent of β, the overall dispersion relation still does depend on β as shown in figure 1.16. Shown is the dispersion relationships for a fixed $\psi = -0.5$, but with β changing. By increasing the ratio of the slip length to the film thickness b/h_0 for a fixed h_0, the parameter β is increased. Since it is the weak-slip regime, b/h_0 needs to be small for the dispersion relation to be valid. In fact, for the case of strong-slip, the dispersion relation has a different functional form and the characteristic mode decreases with increasing slip [44]. The dispersion relation in figure 1.16 shows that increasing the contribution of slip in the weak-slip regime increases the peak frequency without changing the characteristic wavelength. This means that ω^* increases as slip becomes more important, and as a result decreases the characteristic time τ^*. In other words, decreasing the liquid-solid interfacial friction speeds up the dewetting of an unstable viscous film.

Returning now to the linearized thin film equation (Eq. 1.72), instead of looking at the dispersion relation of this equation there are other ways to gain insight into this differential equation. Equation 1.72 includes contributions from weak-slip and the effective interface potential. In the case where these two effects are negligible (as is the case for a PS film with $h \gtrsim 50\,\text{nm}$ on a SiOx/Si substrate), equation 1.72 reduces to the linearized capillary-driven supported thin film equation found previously [41]

$$\frac{\partial\delta}{\partial t} = -\frac{\gamma h_0^3}{3\eta}\frac{\partial^4\delta}{\partial x^4}. \tag{1.76}$$

Recently, it was shown that for any non-pathological initial condition $h(x,0)$, the rescaled solution to equation 1.76 converges to a universal solution [45]. More plainly, if one was to add two arbitrary perturbations $\delta_1(x,0)$ and $\delta_2(x,0)$ to two different initially flat films, at some point in time the profiles of those two perturbations would have an identical shape. A little more precisely, there exists a finite time $\tilde{t}$ such that

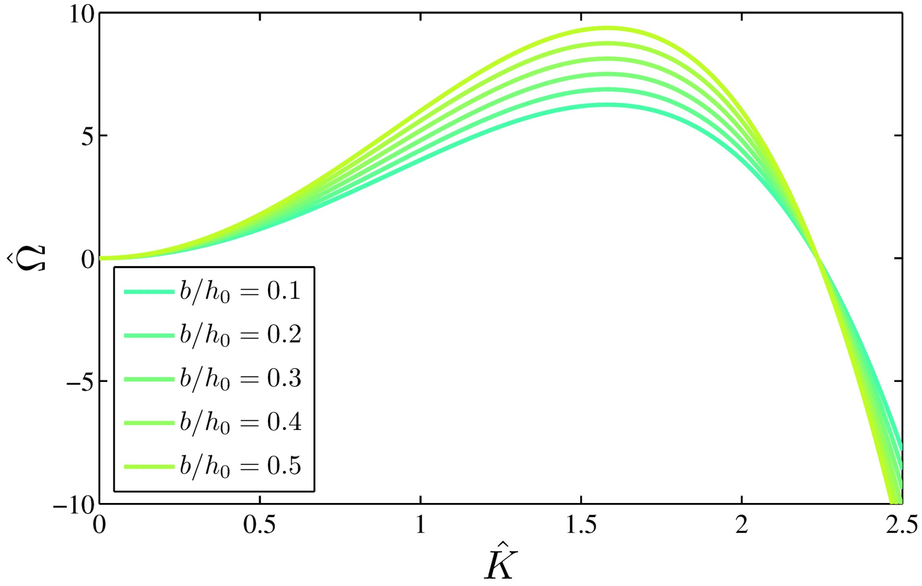

Figure 1.16: Normalized dispersion relation for the linearized thin film equation (Eq. 1.73) varying the slip length b. Plotted is the function $\hat{\Omega} = -\beta(\hat{K}^4 - 5\hat{K}^2)$, with modifying β. As the ratio of the slip length to the average film thickness b/h_0 becomes larger, this increases the peak in the dispersion relation but it does not alter the characteristic mode. For weak-slip the characteristic spinodal wavelength does not change, but since the peak frequency increases with increasing b/h_0, the dewetting process occurs more rapidly with the presence of slip.

for all $t > \tilde{t}$ there exists a horizontal and vertical scale factor $\tilde{x}$ and $\tilde{\delta}$ such that $\delta_1(x/\tilde{x}, t)/\tilde{\delta} = \delta_2(x, t)$. These universal solutions are called universal attractors, and are described in more detail in Paper III.

1.4.3 2D flow in a freestanding film

In contrast to the well-studied case of 2D flow on a substrate, we now explore 2D flow in a freestanding film (right panel of figure 1.13). We return to the relevant Stokes equation for 2D flow in a freestanding film (equation 1.64), with the no shear boundary condition at the liquid-air interfaces (equation 1.63). For simplicity, we assume that the film is thick and the effective interface potential contribution to the pressure can be ignored, which means the pressure is strictly due to excess surface area of the film, $p(x) = -\gamma \frac{\partial^2 h}{\partial x^2}$. Integrating equation 1.64 with respect to x yields

$$\eta \frac{\partial u}{\partial x} = -\gamma \frac{\partial^2 h}{\partial x^2}, \tag{1.77}$$

where the constant of integration is zero because there is no flow gradient for a flat film. Integrating once more with respect to x results in the horizontal velocity

$$u = -\frac{\gamma}{\eta} \frac{\partial h}{\partial x}, \tag{1.78}$$

where the constant of integration is once again zero because there is no flow for a flat film. Just as was done for the supported film case, the horizontal velocity can be integrated to get the flux $Q = \int_0^h u \, dz$ and then is related to the film thickness by $\frac{\partial h}{\partial t} = \frac{-\partial Q}{\partial x}$. This results in the capillary driven freestanding thin film equation

$$\frac{\partial h}{\partial t} = \frac{\gamma}{\eta} \frac{\partial}{\partial x} \left(h \frac{\partial h}{\partial x} \right). \tag{1.79}$$

Remarkably, the capillary driven flow in a freestanding film can be described by a diffusion equation. The diffusion coefficient is identified as $D = \gamma h/\eta$, which corresponds to a "concentration" dependent diffusion coefficient. Since the thickness profile $h(x, t)$ gives the amount of material at a specific plane x, there is a 1D diffusion of mass. The flow in this regime with no interfacial friction is described by a diffusion of fluid in 1D with a local diffusion coefficient that depends on the amount of fluid in the same plane.

Self-similarity

Comparing this freestanding thin film equation to the capillary driven supported thin film equation (Eq. 1.69), the freestanding case has two spatial derivatives compared to four in the supported case. Since the four spatial derivatives and one time derivative in the supported thin film equation lead to self-similar solutions in the variable $x/t^{1/4}$, a natural ansatz for self-similarity in the freestanding thin film equation is the variable $x/t^{1/2}$.

Letting $h(x,t) = f(u)$ with $u = x/t^{1/2}$ in equation 1.79 gives a differential equation in terms of u, f, and derivatives of f:

$$\frac{uf'}{2} = -\frac{\gamma}{\eta}\left(f'^2 + ff''\right). \tag{1.80}$$

Since this equation does not have any terms with h, x, or t, this demonstrates the existence of self-similar solutions for $h(x,t)$ in the variable $u = x/t^{1/2}$.

Linearization

The linearization of equation 1.79 is straightforward compared to the supported case. Letting $h(x,t) = h_0 + \delta(x,t)$ gives to first order in δ

$$\frac{\partial \delta}{\partial t} = \frac{\gamma h_0}{\eta}\frac{\partial^2 \delta}{\partial x^2}. \tag{1.81}$$

This is mathematically equivalent to the heat equation, which is the diffusion equation with a constant diffusion coefficient. By letting $\delta = \delta_0 e^{ikx+\omega t}$, the dispersion relation for the linearized freestanding thin film equation is

$$\omega = -\frac{\gamma h_0}{\eta}k^2, \tag{1.82}$$

which is plotted in figure 1.17. Since the effective interface potential was not included for the freestanding case, there is no disjoining pressure to destabilize the film in this model, and as a result all modes are stable with $\omega < 0$. If an initial perturbation is

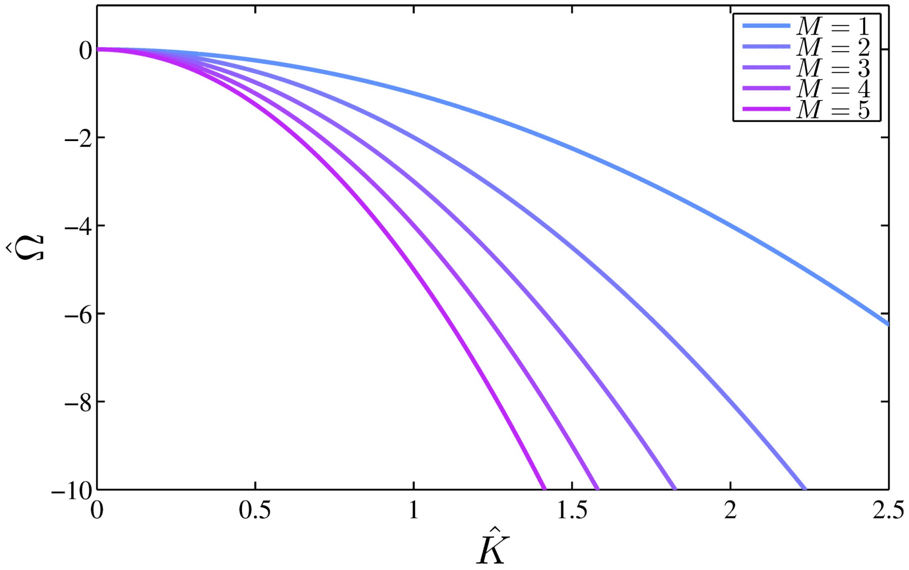

Figure 1.17: Normalized dispersion relation for the capillary driven linearized free-standing thin film equation. Plotted is the function $\hat{\Omega} = -M\hat{K}^2$. As the parameter $M = \gamma h_0/\eta$ becomes larger, the relaxation dynamics of a perturbation speed up.

made in a film with a particular wave vector k, the frequency dictates how quickly the perturbation will relax. The larger the absolute value of the frequency $|\omega|$, the faster the relaxation. For larger wave vectors, there is more curvature which drives relaxation, and therefore a larger $|\omega|$. Increasing the surface tension or film thickness, or decreasing the viscosity, also results in a faster relaxation as shown by the prefactor $\gamma h_0/\eta$ in the dispersion relation.

1.4.4 3D axisymmetric flow on a substrate

When the film thickness profile has an axis of symmetry perpendicular to the plane of the film, the profile can be written as a function of a radial variable r, such that $h(\vec{x}, t) = h(r, t)$. This situation arises in several practical situations including the spreading of droplets on a substrate and the growth of a dewetted hole in a film. The thin film equation in the 2D supported case can be generalized to 3D as

$$\eta\frac{\partial h}{\partial t} = \nabla \cdot \left[\left(\frac{h^3}{3} + bh^2\right)\nabla\left(-\gamma\nabla^2 h + \Phi'(h)\right)\right]. \tag{1.83}$$

Using the gradient operator in cylindrical coordinates in equation 1.83 gives [46]

$$\eta \frac{\partial h}{\partial t} = \frac{1}{r}\frac{\partial}{\partial r}\left[r \left(\frac{h^3}{3} + bh^2 \right) \left[-\gamma \left(\frac{\partial^3 h}{\partial r^3} + \frac{1}{r}\frac{\partial^2 h}{\partial r^2} - \frac{1}{r^2}\frac{\partial h}{\partial r} \right) + \frac{\partial \Phi'(h)}{\partial r} \right] \right]. \tag{1.84}$$

Linearization

Proceeding as in the 2D cases shown in the previous sections, we let $h(r,t) = h_0 + \delta(r,t)$. Substituting this into equation 1.84 and taking only terms which are first order in δ gives the linearized axisymmetric thin film equation

$$\begin{aligned}\eta \frac{\partial h}{\partial t} = \left(\frac{h_0^3}{3} + bh_0^2 \right) \Bigg[& \left(-\gamma \frac{\partial^4 \delta}{\partial r^4} + \frac{\partial^2 \delta}{\partial r^2} \Phi''(h_0) \right) \\ & + \frac{1}{r} \left(-2\gamma \frac{\partial^3 \delta}{\partial r^3} + \frac{\partial \delta}{\partial r} \Phi''(h_0) \right) - \frac{1}{r^2}\frac{\partial^2 \delta}{\partial r^2} + \frac{1}{r^3}\frac{\partial \delta}{\partial r} \Bigg]. \end{aligned} \tag{1.85}$$

The right hand side of this equation has increasing orders of inverse powers of r. An interesting limit is for objects with a large radius. In this case, terms with $1/r^n$ drop off and what is left is equivalent to the 2D linearized thin film equation (Eq. 1.72). Another interesting limit is for the case where the effective interface potential can be ignored. Then there are self-similar solutions in the variable $u = r/t^{1/4}$ [42]. Also, just like there was for the 2D case, there is a universal attractor to which all initial axisymmetric profiles converge for the 3D axisymmetric thin film equation driven by surface tension [47]. The attractor for 3D axisymmetric flow is discussed in detail in Paper III of Chapter 3.

1.5 Measurement of flow at small lengthscales

The measurement of flow in bulk systems has been textbook knowledge for decades [48]. Commercial rheometers which probe the response of a test volume of liquid to a range of shear rates are used commonly by industry. Although traditional rheometers have been used to study molecular-level problems such as interfacial friction [49], the results can be difficult to interpret.

Since thin films are often used in technological applications there is a strong motivation to probe the flow properties, namely the viscosity of the thin film. There have been several interesting observations of how flow in thin films is different from flow in thick films. In certain circumstances, the measured viscosity depends on film thickness [48, 50, 51] and on the molecular weight of the polymer in unconventional ways [52]. Viscoelastic effects have been measured [53, 54] in thin PS films above their glass transition temperature, where the strain-rate depended on both the stress and stress-rate. The flow of the near surface region in polymer thin films below their glass transition temperature has been a particularly active field of research over the past decade [55–63]. As well, flow in thin films has been used to probe the effect of a slip substrate [49, 52, 64–87], where the fluid has a non-zero horizontal velocity at the fluid-sold interface.

With this motivation, we examine the current state of the art in measuring flow in thin films. Since traditional methods for measuring viscosity are ineffective at small lengthscales, new techniques have been developed over that last two decades. A common way that many of these techniques developed was the observation and careful characterization of a viscosity dependent process. An excellent example which fits into this paradigm is dewetting. By understanding the dynamics of dewetting, the observation of this physical process has turned into an experimental technique. Arguably, surface fluctuations, capillary levelling, and droplet spreading also fit into this paradigm. A review of some of the major techniques used to study nano-rheology is presented in the next section, before describing some of the findings relevant to this thesis.

1.5.1 Techniques

Surface fluctuations

When spin cast, polymer films start off with a surface roughness that is flatter than their equilibrium value [88]. The equilibrium square-amplitude of surface fluctuations A_k^2 is given by the equipartition theorem [88] as

$$A_k^2(t \to \infty) = \frac{k_B T}{\gamma k^2 + \Phi''(h_0)}. \qquad (1.86)$$

By measuring $A_k^2(t)$ as it evolves towards $A_k^2(t \to \infty)$, the viscosity can be fit to

$$A_k^2(t) = A_k^2(0) + \left(A_k^2(t \to \infty) - A_k^2(0)\right)\left(1 - e^{-2\Gamma_k t}\right), \tag{1.87}$$

where the wave vector dependent relaxation frequency Γ_k is given by [89]

$$\Gamma_k = \frac{h_0^3 k^2}{3\eta} \frac{k_B T}{A_k^2(t \to \infty)}, \tag{1.88}$$

with h_0 being the average film thickness. This dispersion relation is equivalent to equation 1.73, with $b = 0$.

In other words, if films are created which are initially flat, then by measuring the wavelength dependence of the surface fluctuation spectrum over time, the viscosity can be extracted based on how quickly the spectrum evolves. The surface fluctuation spectrum has been measured either using grazing incidence small-angle x-ray scattering (GISAXS) [90], atomic force microscopy (AFM) [52, 88, 90–92], or x-ray photon correlation spectroscopy (XPCS) [51, 93, 94]. One advantage of the technique is that it can be applied to films down to $h = 3\,\text{nm}$ [52]. A disadvantage of the technique is that the films being measured are always out of equilibrium, and the role of initial stresses in the film or out of equilibrium conformations of the polymer chains might affect the results [95].

The XPCS measurements have the added ability to look at correlations in the same region of the film. By recording the intensity autocorrelation function, the random thermal fluctuations of the surface modes can be observed. The autocorrelation function decays with a wave vector dependent relaxation time $\tau(k) \propto \frac{\eta}{k\gamma}$, from which the viscosity can be extracted.

Surface force apparatus

A surface force apparatus (SFA) measures the viscous force F_v on a curved surface as it is moved into and out of contact with a thin film [73, 96, 97]. The gap between the sphere and the substrate is measured using interference fringes between the semi-transparent substrate and sphere as observed from above. The force is extracted from a piezoelectric element connected to a cantilever supporting the substrate. Other variations exist, such as using an AFM with a sphere glued to the tip [98, 99] or a dynamic surface force apparatus where there are two precise distance measurements made to completely decouple the force measured and gap distance [79]. For all of these cases the force can be written in terms of the gap distance D, the relative velocity of the sphere and substrate $\dot{D}$, the viscosity of the film, and the radius of the sphere R as [79]

$$F_v = \frac{6\pi\eta R^2 \dot{D}}{D} f^*, \tag{1.89}$$

where f^* determines the effect of slip at the liquid-solid interface and is given by

$$f^* = \frac{1}{4}\left[1 + \frac{3D}{2b}\left(\ln\left[(1 + 4b/D)^{1+4b/D}\right] - 1\right)\right], \tag{1.90}$$

which depends on the slip length b.

Knowing $\dot{D}$ and R, the force versus gap distance curve can be fit to equation 1.89. From this fit, either the viscosity can be extracted assuming a no-slip boundary condition, or knowing the viscosity, the slip length can be determined.

Dewetting

For a purely viscous film dewetting a solid substrate with a no-slip boundary condition, the horizontal velocity of the dewetting rim v is given by [100]

$$v_{\mathrm{no-slip}} \propto \frac{\gamma}{\eta}\theta_e^3, \tag{1.91}$$

where θ_e is the equilibrium Young's contact angle of the liquid on the solid substrate. The dynamics of a dewetting front has been measured for the case of a 2D straight edge [75], but is more frequently measured in the case of a dewetting hole [101–103]. For a dewetting hole, since the velocity given by equation 1.91 is independent of the radius of the hole R, this means that the size of the hole grows linearly in time

$$R_{\mathrm{no-slip}} \propto \frac{\gamma}{\eta}\theta_e^3 t. \tag{1.92}$$

On the other hand, if instead of a no-slip boundary condition at the liquid-solid interface there is a strong interfacial slippage, the slip velocity v_{slip} has been determined to be [104]

$$v_{\text{slip}} \propto \frac{\eta}{\gamma}\theta_e \frac{b}{\sqrt{h_0 R}}, \tag{1.93}$$

where h_0 is the thickness of the film. Integrating to get the dynamics of a growing hole yields

$$R_{\text{slip}} \propto \left(\frac{\eta}{\gamma}\theta_e b t\right)^{2/3}. \tag{1.94}$$

Another, perhaps more reliable [105], way to extract details of the molecular friction at the liquid-solid interface is by using the shape of the dewetting rim profile. At the edge of the hole material builds up into a rim, and the height profile of the outer half of the rim follows a damped harmonic oscillation which is altered in the presence of viscoelasticity [106] or slip [107]. For the case of strong-slip, the height profile of the outer edge of the rim $h(x,t)$ can be described by a damped oscillatory profile $h(x,t) = h_0 + \delta h_0 e^{k\xi}$, where ξ is the horizontal position relative to the rim. The wave vector k is related to the film thickness, slip length and velocity of the rim v by [107]

$$\left(1+\frac{h_0}{3b}\right)(h_0 k)^3 + 4\frac{\eta v}{\gamma}\left(1+\frac{h_0}{2b}\right)(h_0 k)^2 = \frac{\eta v}{\gamma}\frac{h_0}{b}. \tag{1.95}$$

By measuring a rim profile with AFM and fitting this profile to a damped harmonic oscillation, the damping wave vector can be determined. Knowing $\eta v/\gamma$, the measured damping wave vector can be used in equation 1.95 to extract the slip length b.

In short, by observing the dewetting of a film, rheological properties of the fluid can be determined. Examining the growth dynamics of holes or the height profile of the outer edge of the dewetting rim leads to quantitatively similar results [66]. This consistency check provides a distinct advantage to using dewetting as an experimental technique. One potential drawback of dewetting is the theoretical uncertainty in how to treat the contact line at the trailing edge of the dewetting rim. Theoretically, there is a singularity in the energy dissipated at the contact line which requires a microscopic cutoff lengthscale to be introduced [108].

Droplet spreading

When a droplet is placed on a solid substrate, the spreading dynamics depend on the equilibrium state of the droplet. As is the case for dewetting, the presence of a contact line can cause complications in describing the motion of a droplet.

The problem becomes tractable for the case of a droplet spreading on a prewetted film of the same fluid [46]. In that case the dynamics of a spreading droplet can be described by the axisymmetric thin film equation. The droplet height h, the droplet contact angle θ, and droplet radius r follow a power law decay, where the power law exponents depend on the initial droplet volume Ω, the surface tension, the viscosity, the thickness of the prewetted film, and initial radius of curvature of the droplet. In the limit that the prewetted film thickness goes to zero, Tanner's law [109] is recovered:

$$\theta(t) \propto \left(\frac{t}{\tau}\right)^{-3/10}, \tag{1.96}$$

where the relaxation time τ is given by

$$\tau = \frac{\Omega^{1/3}\eta}{\gamma}. \tag{1.97}$$

Tanner's law describes the spreading of droplets which completely wet the substrate, but with no prewetted film. An alternate derivation of Tanner's law is given by examining the dissipation at the contact line and equating that to the work done by the driving force: a procedure known as Frenkel's method [110]. As the droplet spreads, the contact line moves radially outward. The dissipation in the droplet can be approximated by the dissipation in a wedge of fluid near the contact line [111]. In that case the power dissipated by a spreading droplet can be written as [110, 112]

$$\mathcal{P} = \frac{\eta r}{\theta}\left(\frac{dr}{dt}\right)^2. \tag{1.98}$$

The driving force for complete wetting is given by the derivative of the excess free energy with respect to r as $F = -\frac{\partial \Delta \mathcal{F}}{\partial r} \approx \pi r \gamma \theta^2$. Setting $\mathcal{P} = F\left(\frac{dr}{dt}\right)$ yields

$$\frac{dr}{dt} \propto \frac{\gamma}{\eta}\theta^3. \tag{1.99}$$

Making a change of variables by using $\frac{d\theta}{dr} = \frac{-2\theta^{4/3}}{\Omega^{1/3}}$ for a spherical cap droplet at small contact angles [112], and integrating gives

$$\theta^{-10/3} \propto \frac{\gamma t}{\eta \Omega^{1/3}}, \tag{1.100}$$

which is equivalent to Tanner's law (equation 1.96).

In the partial wetting case, where in equilibrium the droplet comes to a non-zero contact angle θ_e, a similar energy dissipation argument can be made as the complete wetting case, except the driving force is given by a difference between the instantaneous and equilibrium contact angle $F \approx \pi r \gamma (\theta^2 - \theta_e^2)$. Using the same steps as the complete wetting case, the velocity of the contact line in the partial wetting case is given by [113]

$$\frac{dr}{dt} \propto \frac{\gamma}{\eta} \theta (\theta^2 - \theta_e^2). \tag{1.101}$$

For droplets which start off with an initial contact angle θ_i close to their equilibrium contact angle, the solution to this differential equation is an exponential relaxation

$$\frac{\theta^2 - \theta_e^2}{\theta_i^2 - \theta_e^2} = e^{-t/\tau}, \tag{1.102}$$

with the relaxation time

$$\tau \propto \frac{\eta \Omega^{1/3}}{\gamma \theta_e^{10/3}}. \tag{1.103}$$

Comparing the dynamics of complete and partial wetting, the functional form of the contact angle relaxation is different (compare equation 1.96 and 1.102), but the relaxation times have a similar form (compare 1.97 and 1.103). In both cases, the relaxation time depends on the viscosity of the fluid.

Although in principle the contact angle dynamics could be used as a method to measure the viscosity of a fluid, the unknown constants of proportionality make this impractical. Instead, droplet spreading can give information about any extra driving forces such as van der Waals interactions for small droplets [114] or information about the interfacial friction [115] based on deviations from the contact line scaling laws derived above.

Capillary levelling

In the final category of experimental techniques, excess surface area is purposefully created in a thin film using a variety of methods, and then by monitoring the time evolution of the film's surface under the driving force of surface tension, the rheological properties of the film are extracted. Initial perturbations have been created by the embedding and dissolution of gold nanoparticles into the surface of a PS film (nanohole relaxation) [58], by imprinting and subsequent removal of a carefully designed nanoimprinting mold (nanoimprint reflow) [53, 116–119], or by stacking a second film of the same material with a well characterized edge onto the original film [13, 47, 120, 121].

For the nanoimprint measurements, the patterns created were uniform along one spatial direction, which means their viscous relaxation can be described by the results of Section 1.4.2. The mold used has either been a repeating pattern with a specific wavelength [116, 117], or a repeating pattern with a modulating wavelength [53, 54, 118, 119]. Often when using this technique, the amplitude of the patterns created are much smaller than the film thickness, which means the relaxation follows the linearized dispersion relation from figure 1.15. By measuring the decay of modes in the patterned film and comparing the decay to the dispersion relation, the prefactor $\frac{\gamma}{\eta}(h_0^3/3 + bh_0^2)$ can be determined.

Capillary levelling experiments performed by the Dalnoki-Veress group have focused on creating initial conditions with different geometries by using films with an initially sharp edge. One geometry in particular, known as step levelling, has been used as a convenient geometry to study flow. In step levelling, a film with a sharp edge that is uniform along one spatial dimension is stacked onto a second film of the same material. The initial condition is a Heaviside step profile. Because the edge of the step has excess surface area, the step broadens over time with a width that scales with $t^{1/4}$. The step profiles are a self-similar solution of the capillary driven thin film equation ("Self-similarity" in Section 1.4.2) - the profile at a later time t_2 is just a horizontal stretch of the profile measured at an earlier time t_1 such that $h(x/t_1^{1/4}, t_1) = h(x/t_2^{1/4}, t_2)$. The self-similar experimental profiles are compared to a numerically calculated solution of the supported thin film equation to extract the prefactor $\frac{\gamma}{\eta}(h_0^3/3 + bh_0^2)$.

Both capillary levelling experiments and surface fluctuation measurements benefit from having no contact line at the liquid-solid interface which simplifies the analysis compared to dewetting or droplet spreading. Capillary levelling has the added benefit of being able to measure films which have been pre-annealed for many reptation times. In contrast, to measure surface fluctuations the film needs to start in a non-equilibrium state where chain conformations can potentially be different due to the spin coating process [122]. The step levelling geometry in particular allows for long annealing times. Although the perturbation broadens with time in step levelling, it does not disappear over time as it does for other geometries. For example, a cylindrical hole will fill in over time, and its depth will decrease [47], which increases measurement noise for long annealing times.

1.5.2 Literature results

With those main classes of experimental techniques in mind, a brief review will be provided for the three areas introduced at the beginning of the thesis where polymer physics and fluid mechanics intersect: molecular anisotropy and heterogeneity, initial state of the film, and interfacial friction.

Molecular anisotropy and heterogeneity

One way to induce molecular anisotropy of a polymer molecule is to confine it to a film with thickness $h < R_g$. Since the molecule is only confined in one spatial dimension, the conformation of the chains will differ compared to the bulk, resulting in a different horizontal and vertical characteristic lengthscale. Surface fluctuations have been used to probe the confinement of entangled PS films well above the PS glass transition temperature [52]. For large molecular weights, it was found that the effective viscosity becomes independent of molecular weight. This effect was attributed to the onset of an effective slip boundary condition. The description of these results is in contrast to XPCS measurements which found reduced viscosity at the free surface above the glass transition temperature, and attributed this effect to reduced entanglements at the surface [51]. The XPCS measurements had gold nanoparticles embedded in the surface of the film, and the fluctuations of the gold was measured to determine the fluctuations of the surface.

It is difficult to decouple the effect of confinement and the effect of interactions with the substrate. The thinner the film, the larger the fraction of molecular segments interacting with the substrate. The more confined a polymer chain is in a supported film, the more likely that chain is to be found close to the substrate which means it has a larger effective interaction with the interface. Previous studies using a surface forces apparatus found that an adsorbed polymer layer creates an effective slip boundary condition [84], which could explain the onset of slip observed in the surface fluctuation measurements. It has also been shown using a surface force apparatus that an anisotropic structured fluid demonstrates slip behaviour [68].

Another system in which there is non-uniformity is a polystyrene film at temperatures below the glass transition temperature. It has been shown that there is a mobile surface layer $\sim 5 - 10\,\mathrm{nm}$ thick at the free surface of glassy polymers [55, 58, 59, 123]. The viscosity of this layer can be orders of magnitude smaller than the bulk of the film. Surface fluctuations have been used to measure the effective viscosity of this mobile surface layer. Because the measured mobility was identical for all films thinner than 9 nm, this put a bound on the thickness of the mobile surface region to less than 3 nm thick [91]. Step levelling has been used to quantitatively measure the mobility prefactor $\gamma h^3/3\eta$ in samples with a bulk-like thickness. The step broadened at temperatures below the glass transition temperature, and the results agreed with a modification to the thin film equation where there was a no-slip boundary condition at a fixed distance from the air interface h_m. This parameter describes the thickness of the mobile surface layer, with reduced viscosity η_m. The ratio η_m/h_m was found to be non-divergent at low temperature, and deviates from the extrapolation of the VFT equation (Eq. 1.21) at high temperatures.

Initial state of the film

To prepare a thin polymer film, polymer is first dissolved in a volatile solvent with a small concentration of polymer. A thin layer of this solution is spread onto a substrate (typically by spin coating), the solvent then evaporates leaving behind a polymer film. The process of solvent evaporation leaves behind residual stress in the film. Typically, polymer films are annealed after preparation to remove these stresses. However, to measure surface fluctuations, the film starts in the as-cast state with no pre-annealing. The question of whether residual stresses exist in surface fluctuation measurements was addressed by examining the viscoelastic behaviour of thin PS films. For films thinner than 10 nm, there was a measurable elastic component attributed to insufficiently long annealing time [124]. Other studies using XPCS found a similar viscoelastic behaviour but attributed it to the formation of an irreversibly adsorbed layer of polymer at the substrate [94]. Other measurement techniques have also found viscoelastic effects, even in pre-annealed films [53]. In that measurement, a nanoimprint pattern was pressed into a pre-annealed film well above the glass transition temperature, and then rapidly quenched to room temperature and removed. The capillary levelling was then measured using AFM before and after a short 30 second annealing at 140°C. The large wave vector relaxation was consistent with a viscoelastic response in the film [53].

The entanglement density can also vary for as-cast films. Surface fluctuations have been used to study the inter-chain entanglements of spin cast PS in decalin. Decalin has a Θ temperature near room temperature. The Θ temperature of a polymer in a solvent is the specific temperature in which $R_g \propto \sqrt{M_w}$ in the solvent. Using the measurement of surface fluctuations, it was found that the films start off with a lower effective viscosity [92]. The viscosity increased with time with a characteristic relaxation time that depended on the temperature at which the film was prepared [92]. This preparation dependence was ascribed to an onset of inter-chain entanglements for films prepared above the Θ temperature. Other work has shown that as-cast films can have an entanglement density that is different than the entanglement density in equilibrated films [122].

The initial state of the film does not just depend on the out of equilibrium chain conformations due to spin coating. Films can be purposefully prepared with an initial profile $h(x, t = 0)$ which affects the relaxation towards a flat film. For example, higher wave vector modes relax more quickly than shorter wave vectors as was shown in the dispersion relation of the supported thin film equation. Another way that the initial profile affects flow is through the dimensionality. The depth of surface profiles decay with a power law that depends on their dimensionality. For example, the depth of a 2D trench decays with a power law in time of $t^{-1/4}$ [120], while the depth of a 3D axisymmetric cylindrical hole decays with a faster power law of $t^{-1/2}$.

Interfacial friction

The existence of systems with reduced liquid-solid interfacial friction that leads to a slip boundary condition has gained strong experimental confirmation only within the past few decades. As a result, a surge of recent experiments have attempted to probe the exact nature of interfacial slip and what parameters affect the slip length.

Surface force apparatus measurements have revealed many interesting properties of slip. SFA results have shown that the measured slip length can depend on dissolved gas in the liquid as a result of gas reducing friction at the liquid-solid interface [83]. It has also been shown that the slip length can depend on shear rate [73] or not depend on shear rate [99] depending on the liquid-solid system. As well, surface roughness of the substrate can reduce the effect of slip in certain circumstances [125]. For partially wetting fluids, slip has been shown to be affected by the contact angle of the liquid on the substrate and the polarizability of the liquid molecules [68].

The dewetting of polymeric liquids has also been extensively used to study slip. Dewetting often occurs readily in slip systems as the substrates are typically unfavourable for most polymeric liquids. The slip length primarily depends on the polymer-substrate combination [126]. For one such combination, PS on AF1600 (Teflon), slip depends on the molecular weight of PS [66]. For low molecular weights the slip length is small, but at high molecular weights the slip length increases as $b \propto M_w^3$. Dewetting measurements have shown that the slip length measured is sensitive to the sample preparation and annealing procedure [105].

Recently, the effect of slip on droplet dynamics was examined. Slip at the liquid-solid interface influences both droplet shape and contact line movement [115].

1.5.3 Overview of Thesis Work

This thesis is comprised of work which examines viscous flow in thin polymer films. Each of the 3 major areas outlined in the previous section are touched upon: Molecular anisotropy in films of diblock copolymer is explored using droplet spreading. The initial state of a film is studied by patterning specific symmetries in the initial thickness profiles of PS films, and measuring the capillary levelling of those profiles. Interfacial friction is examined by measuring the step levelling of freestanding PS films.

More detail about the specific papers will be provided in Chapter 3, but first the details about how these experiments were performed will be presented in Chapter 2.

Chapter 2

Experimental

The experimental procedures used in the papers of Chapter 3 are summarized in the main text of each respective paper. Since each paper was written in a “letter” style, the experimental descriptions provided are concise. This chapter will serve as a supplement to those experimental sections and will outline the major experimental procedures used in this thesis work. In what follows, the technique used to create thin polymer films, spin coating, will be explained. Spin coating is typically used to produce films with a uniform thickness. However, because the experiments in this thesis involve droplet spreading or capillary levelling, non-uniformity in the film thickness had to be induced. Details about how perturbations in the initial thickness profile were created are described in Section 2.2. Finally, the methods used to measure the evolution of the thickness profile in both droplet spreading and capillary levelling experiments will be summarized in Section 2.3.

2.1 Creating thin polymer films

To create a polymer film with thicknesses ranging from nanometres to tens of microns, a substrate is typically coated with a solution of the polymer in a volatile solvent. After the solvent evaporates, only the polymer remains. Different techniques exist for coating a substrate with a dilute polymer solution.

Dip coating [127] is perhaps the most intuitively obvious way to coat a substrate. It involves dipping the substrate into the solution and then pulling it out. The residual liquid that is left on the substrate after retraction from the solution will dry, leaving behind a polymer coating. The larger the concentration of polymer in the liquid left behind, the thicker the polymer coating. For the same concentration of polymer, the more liquid solution left behind after the retraction, the thicker the resulting coating will be. To get a uniform film thickness, the retraction speed needs to be constant, and the receding front of liquid needs to be in a non-inertial regime, requiring slow retraction speeds.

A related technique to dip coating is flow coating [128]. Flow coating involves the retraction of a substrate from fluid trapped between a knife edge (typically a glass slide is used) and the substrate. By adjusting the clearance height of the knife edge and substrate, or by changing the retraction speed of the substrate, films of different thickness can be created.

The coating technique used in this thesis work (as well as in many other papers in the literature) is spin coating. In spin coating, the substrate is placed on a disc connected to motor. The motor can spin the disc and substrate at angular speeds of up to thousands of rotations per minute. Polymer solution is deposited onto the substrate, typically with a pipette, creating a droplet of fluid which coats the substrate. The substrate is then rapidly accelerated to a set angular speed. Excess fluid is ejected radially, causing the droplet to flatten. The residual solvent quickly evaporates, decreasing the thickness of the film. At some point the concentration of solvent is low enough such that the polymer chains lose mobility and the film vitrifies.

Two main parameters control the thickness of the film created by spin coating: the mass fraction of polymer in the solution c, and the angular speed of rotation ω. An approximate relation for the final film thickness h_0 in terms of these two variables is given by [129]

$$h_0 \propto c^{3/2}\omega^{-1/2}. \tag{2.1}$$

Lower polymer concentrations or faster speeds lead to thinner films. Interestingly, a faster spinning speed in spin coating has the opposite effect of a faster retraction speed in dip coating. In either case, it is the amount of solution left on the substrate as the evaporation begins that is important for the final thickness. For dip coating, a faster retraction speed leaves more fluid on the substrate because the fluid has less time to drain away from the substrate. For spin coating, a faster spinning speed has a larger centrifugal force, ejecting more fluid from the substrate and leaving less fluid behind.

Another important parameter for the creation of uniform films is the angular acceleration. If the substrate takes a long time to achieve its final angular velocity, a non-uniform thickness profile can occur with striations in the film thickness pointing radially outward from the centre of the film. Using a larger acceleration has been shown to give a more uniform film [130].

For the experiments in this thesis, a commercial spin coater (Headway Research Inc., Model PWM32) was used to spin coat polymer films. Dilute solutions with concentration $0.5-10\%$ were used in combination with angular speeds of $500-6000\,\mathrm{rpm}$. For the experiments with polymer films on SiOx/Si substrates, films were spin cast directly onto the SiOx/Si substrates. On the other hand, for freestanding films, the films were spin cast onto mica substrates and pre-annealed to remove residual stresses in the film. Mica, which has a much lower surface energy than silicon, provides a substrate for which it is relatively easy to remove the films. For the freestanding levelling experiments in Paper IV, films were transferred directly into the freestanding state. While the pore formation experiments required an additional transfer of the films onto SiOx/Si substrates to create pores, as described in section 2.2.3.

2.2 Creating perturbations in thin polymer films

Creating uniform films is often the goal of the coating procedures described in the previous section. However, to study the surface tension driven flow of a viscous liquid without any contribution from the effective interface potential, excess surface area needs to be created in the film. This section details the various ways a non-uniform thickness profile was created for films studied in this thesis.

2.2.1 Non-uniform spin coating

A simple way to create a non-uniform film thickness is to do an intentionally poor job of spin coating. By using a slow acceleration or modulating the speed during the spin coating process, a film with a varying thickness can be made. Typically, this gradient in thickness is too small to be of practical use in capillary levelling experiments. The variation in film thickness is usually only nanometres over a horizontal lengthscale of microns. The driving force due to the extra surface area is too small to cause an appreciable flow on experimental time scales. One way to explicitly estimate the timescale for flow is by looking at the linearized 2D supported thin film equation (Eq. 1.76). Using the 192 kg/mol reference polymer from Section 1.2.2 at 140°C, $\gamma/\eta \approx 2.2 \times 10^{-4}\,\mu\text{m/min}$. Assuming a film thickness $h_0 \sim 100\,\text{nm}$ and a film thickness gradient $\nabla h \sim 10^{-3}$, the rate of change of film thickness is found to be $\frac{\partial h}{\partial t} \sim 1\,\text{nm/year}$. Therefore, these gradients are far too small to observe capillary driven flow.

In this thesis, however, we were able to use non-uniform spin coating to study diblock copolymer films. Recall the effective interface potential for a diblock copolymer film in its disordered state with interfacially-induced order from figure 1.8. The potential energy is a decaying and oscillatory function of the film thickness. For a film with such an effective interface potential, the lowest energy state is a dewetted droplet coexisting with a wetting layer. The thickness of the wetting layer is given by the position of the global minimum in the effective interface potential. For a thick and uniform film, there are many potential energy barriers to creating thinner regions of the film. The global minimum cannot be reached through a spontaneous dewetting of the film. Instead, thinner regions have to nucleate for the film to reach its minimum energy state. Once nucleated, any material at the edge of a thinner region would be driven towards thicker regions. Therefore, a significant driving force in the fluid is only present after the nucleation of a thinner region. By purposefully spin coating films of non-uniform thickness, the diblock copolymer films are able to reach their minimum energy state in an experimentally measurable time because thin regions already exist in the film.

To accomplish this, diblock copolymer solution is dripped onto a $2 \times 2\,\text{cm}^2$ SiOx/Si substrate [Fig. 2.1(a)]. Then, the substrate is rotated at a relatively slow angular speed ($\approx 500\,\text{rpm}$). At this low speed, the solvent ejection is minimal, and fluid that is forced radially outward by centrifugal forces builds up at the edge of the substrate [Fig. 2.1(b)]. Finally, the angular speed is rapidly increased ejecting the solvent. An instability develops, which causes an undulatory thickness profile in the film as the solvent evaporates [Fig. 2.1(c)].

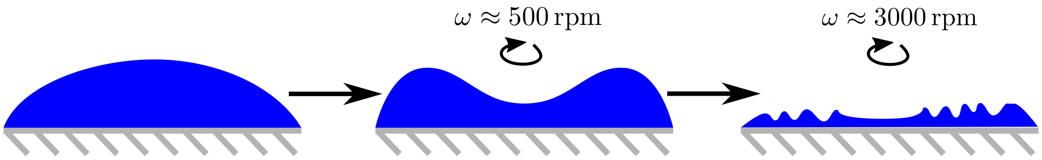

Figure 2.1: Schematic of the process to create non-uniform spin cast films.

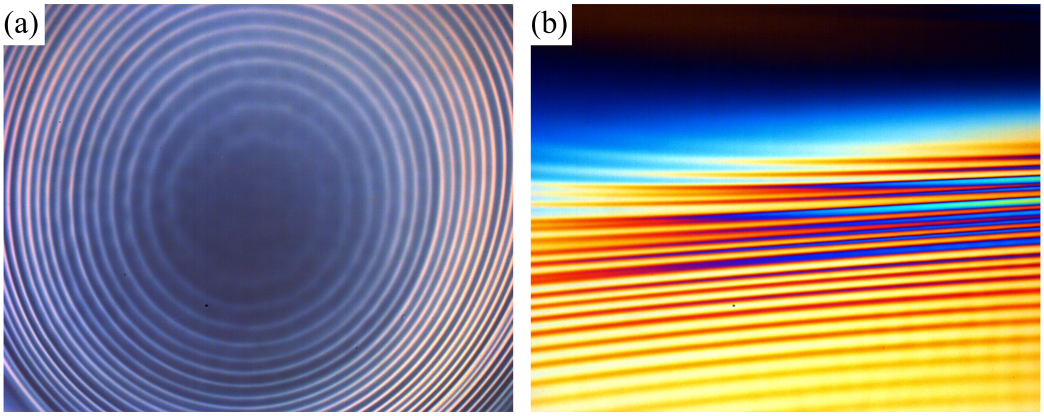

Figure 2.2: Optical microscopy images of spin cast films with non-uniform thickness. (a) The thickness variations radiating out from the centre of a film are visible as variations in the colour observed with the optical microscope. Here the width across the entire image is $\sim 1.2\,\mathrm{mm}$. (b) A different film, zoomed in on a region $\sim 600\,\mu\mathrm{m}$ wide, closer to the edge of the film.

Examples of films created using this spin coating technique are shown in figure 2.2. These optical microscopy images are taken looking at the film from above. Due to the thin film interference of the polymer film on the reflective silicon substrate, the film has an apparent colour which depends on the thickness and index of refraction of the film. The different colours in these images are the result of the non-uniform film thickness.

Another example of a non-uniform film is shown in figure 2.3(a). This film is a PS-P2VP diblock copolymer film, and has thin and thick regions. When the film is heated to 190°C to allow flow to occur, material is pushed from the edge of the thin regions into the thick regions [Fig. 2.3(b-f)]. Over time, the area fraction of the thinner region increases, while the thick regions grow even thicker and break up into droplets. The equilibrium shape of these droplets is examined in Paper I, while the

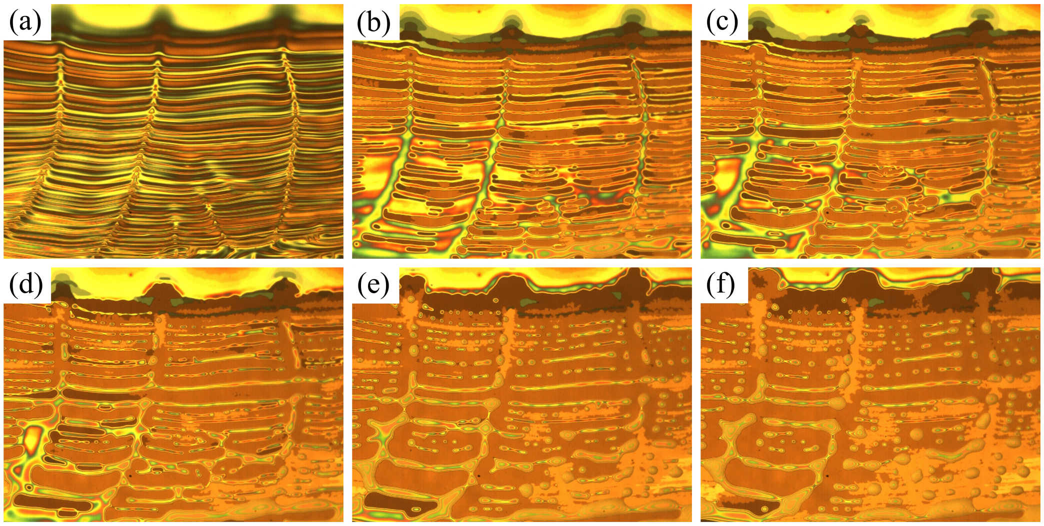

Figure 2.3: Optical microscopy images of a non-uniform diblock copolymer film dewetting. Each image is ∼ 1.2 mm across. The colours are due to the thin film interference of light. The thickness of the coloured regions are (from thinnest to thickest): brown (∼ 50 nm), blue (∼ 100 nm), yellow (∼ 200 nm), green (∼ 300 nm), pink (∼ 500 nm). Then the colour alternates between green and pink as the film gets thicker. (a) The diblock copolymer PS-P2VP film as cast with a purposefully non-uniform film thickness. (b-f) The time evolution of the film held at 190°C for (b) 100 minutes, (c) 200 minutes, (d) 400 minutes, (e) 800 minutes, and (f) 1200 minutes. The thicker regions of the film break up into diblock copolymer droplets which coexist with wetting layers of the same fluid.

dynamics of the droplets as they approach equilibrium is described in Paper II.

2.2.2 Stepped films

A second way to create excess surface area in a film is by making a "stepped film" - the films described in the step capillary levelling experiments in Section 1.5.1. In this thesis step levelling is used to study flow in freestanding films. To make a freestanding step, PS (55 kg/mol) was spin cast from a dilute toluene solution onto a mica substrate. The PS film on mica was pre-annealed to remove residual stress and then floated off of the mica onto a deionized water bath (18.2 MΩ cm). The film was picked up onto a grid with holes, which provided support for the film while still allowing regions ∼ 1 mm across where the film was freely-suspended. The film was allowed to dry and then heated above its glass transition temperature for approximately ten minutes to remove any wrinkles in the film created during the transfer to the grid. A second film was floated off of mica and onto the water bath, and by tapping at the edge of the floating film with tweezers, the film was broken into pieces. The pieces had long, sharp, and clean edges. These pieces were then transferred onto the first PS film on the grid. After drying, the freestanding stepped film was ready to measure.

2.2.3 Focused laser spike annealing

The final method to create a film which has excess surface area is by using focused laser spike annealing. Focused laser spike annealing (Flask) is a technique used to pattern thin films. The temperature dependence of the surface tension described in Section 1.3.1 plays a vital role in the mechanism behind this technique: thermocapillary flow. Although described in detail elsewhere [131], the mechanism of focused laser spike annealing ties in well with concepts introduced earlier in this thesis, and will be described here.

In Flask, a laser is focused onto a silicon substrate with a polymer coating (in this thesis a Verdi V2 laser with $\lambda = 532\,\mathrm{nm}$ was used). The silicon has a large absorption coefficient, which causes the substrate to locally heat up at the focus of the laser. Thus, a radial temperature gradient in the plane of the substrate is created. Because the polymer coating is thin, the temperature of the silicon $T(x, y)$ is equal to the temperature of the film at the same point in the x-y plane. The increase in temperature lowers the viscosity of the polymer film so that it is able to flow, while at the same time, the higher temperature regions have a reduced surface tension. A gradient in temperature means that a gradient in surface tension occurs in the film. This drives the flow of fluid away from regions of low surface tension to regions of high surface tension. In other words, the laser is used to effectively push fluid away from the centre of its focal point.

In this thesis, Flask is used to create 3D axisymmetric perturbations as well as 2D perturbations. A 3D axisymmetric feature is created by focusing the laser at a single point on the substrate. This results in a divot (hole) surrounded by a rim of fluid. By increasing the power of the laser or exposure time, features with a larger depth and wider horizontal extent can be created. A 2D feature is created by exposing the polymer film on the substrate to the laser while simultaneously translating a motorized stage holding the substrate. This allows the patterning of 2D features which are similar to a trench with a rim at its edges. The depth and width of the trench can be increased by using a higher laser power or by translating the sample stage more slowly.

Paper III in Chapter 3 utilizes Flask to create a variety of 2D and 3D features. By combining combinations of holes and trenches arbitrary patterns can be created. In Paper V, holes were made with a depth that went down to the substrate with varying horizontal extent. By transferring the film into the free-standing state we are able to create a thin freestanding membrane with pores.

2.3 Measuring perturbations in thin polymer films

There were two main experimental techniques used in the papers contained in this thesis: optical microscopy (OM) and atomic force microscopy (AFM). For measuring the thickness profile of droplets, the thin film interference of light was measured with OM (Papers I and II). For capillary levelling experiments, AFM was used to measure the surface profile of the films (Papers III, IV). Paper V used both OM and AFM in order to determine the radius of pores in freestanding films. Here, more detail will be provided about how OM was used to measure droplet spreading followed by how AFM was used to measure capillary levelling.

2.3.1 Droplet spreading

When a thin film on a reflective substrate is observed from above using OM, the measured intensity of light is proportional to the reflectance [12, 132]

$$R(h) = \frac{A - B + C\cos\left(4\pi n_p h/\lambda\right)}{A + B + C\cos\left(4\pi n_p h \lambda\right)}, \tag{2.2}$$

where $A = (1 + n_p^2)(n_p^2 + n_{\text{sub}}^2)$, $B = 4n_p^2 n_{\text{sub}}$, and $C = (1 - n_p^2)(n_p^2 - n_{\text{sub}}^2)$. The reflectance depends on the index of refraction of the polymer n_p and substrate n_{sub}, as well as the wavelength of light λ. The reflectance is plotted as a function of h/λ in figure 2.4 for a typical polymer on a silicon substrate. The intensity of reflected light is a periodic function of the film thickness, repeating every $\lambda/2n_p$. The periodicity of

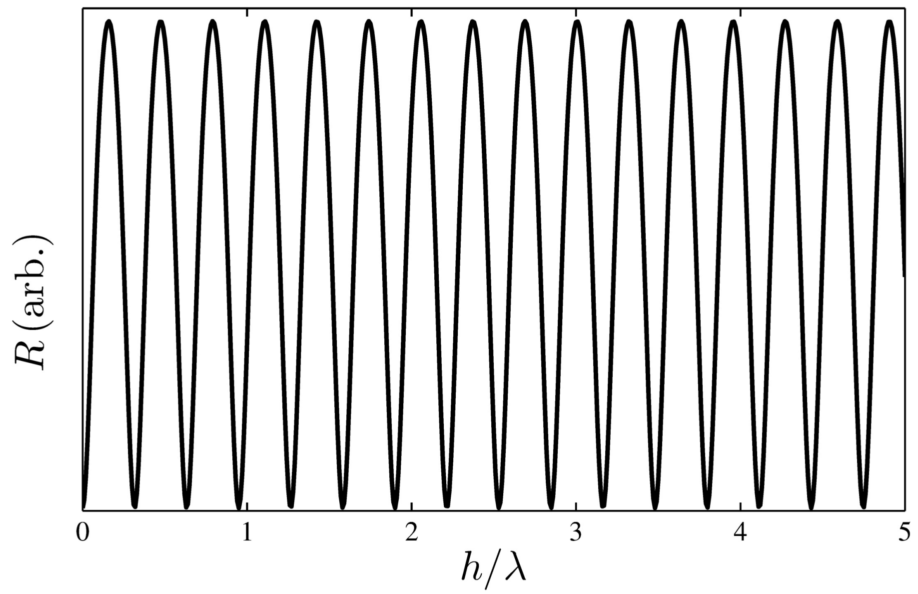

Figure 2.4: Film thickness dependence of the optical reflectance for a polymer film on a reflective substrate. The reflectance is calculated from equation 2.2 for a normal incidence of light with wavelength λ. The intensity of reflected light observed using OM depends on the film thickness. Knowing information about the shape of the surface profile, allows the determination of the film thickness $h(x, y)$.

the reflectance means that the thickness cannot unambiguously be determined for an arbitrary film thickness profile $h(x, y)$. However, if there is extra information about the surface profile (e.g. if the profile is a monotonically decreasing function), the film thickness profile can be extracted from the intensity of reflected light.

The dewetted diblock copolymer droplets discussed in the previous section are one such example where quantitative information about the thickness profile can be determined. An example of a droplet with a slightly irregular shape is shown in figure 2.5. The image on the left was obtained using OM with a monochromatic filter. The top of the droplet is the light grey circle in the centre of the image. By assuming the thickness decreases away from the centre of the droplet, the droplet profile can be determined from the locations of the maximums and minimums of intensity (shown in the second image "Intensity extrema"). Each thin white ring in the second image defines a band of constant film thickness. Moreover, the difference in thickness between bands is given by the half-periodicity of the reflectance $\lambda/4n_p$.

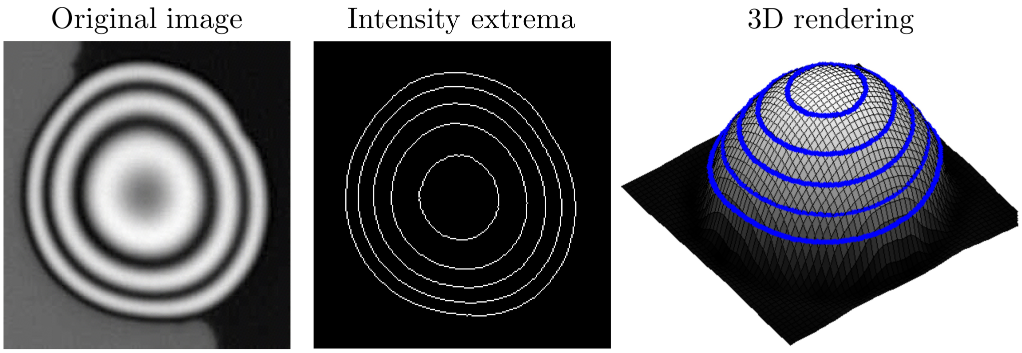

Original image Intensity extrema 3D rendering

Figure 2.5: Image processing steps to extract the profile of a droplet from interference optical microscopy. The original image is measured with optical microscopy and a monochromatic filter $\lambda = 420\,\mathrm{nm}$. It shows a diblock copolymer droplet with a slightly irregular shape coexisting with two different thicknesses of wetting layer on the left and right. Local maximums and minimums in intensity which form a closed shape are extracted in the second image. From the periodicity of the reflectance curve, the droplet shape can be interpolated between the maximums and minimums, as shown on the right. An atypical droplet with an irregular shape is shown here to demonstrate a general case the droplet image processing can successfully handle.

This allows for a 3D reconstruction of the droplet shape [right image of figure 2.5]. Paper I and II of this thesis use the locations of the maximums and minimums in intensity measured by OM to extract the contact angle of droplets.

2.3.2 Capillary levelling

Although OM has been used to study capillary levelling [12], AFM is primarily used as it provides better resolution of the film thickness profile. Briefly, AFM uses a sharp tip attached to the end of an cantilever which can be used to map out the topography of a sample. In tapping mode (intermittent contact mode), the cantilever is driven at its base by a piezo with a fixed amplitude and frequency (the amplitude is typically $\sim 100\,\mathrm{nm}$). A laser is reflected off the back of the cantilever and onto a split photodiode to detect variations in the frequency and amplitude of the oscillating tip. As the tip is brought near a film, the measured tip oscillation gives information about the distance between the cantilever and sample, as well as any energy dissipation that occurs. From this information, a height profile of the surface can be determined by rastering the cantilever tip across the surface.

Technical details required to perform capillary levelling experiments are described in reference [133]. Here, some of the important aspects of capillary levelling developed in this thesis work will be explained.

In capillary levelling experiments performed in the Dalnoki-Veress group, a film with a given initial perturbation is measured using AFM (Veeco, Caliber) at different annealing times $\{t_1, t_2, ..., t_N\}$. This gives a set of profiles $\{h(x, t_1), h(x, t_2), ..., h(x, t_N)\}$. The experimentally measured profiles should be self-similar to ensure a robust comparison to theory. As detailed in Section 1.4, the profiles should be self-similar in $x/t^{1/\beta}$, where $\beta = 4$ for a supported film, while $\beta = 2$ for a freestanding film. Profiles measured for short annealing times might not be self-similar due to extra driving forces such as residual stresses from interfacial healing between the two stacked films. The sample should be annealed until profiles measured at two different annealing times collapse onto the same self-similar profile – $h(x/t_{N-1}^{1/\beta}, t_{N-1}) = h(x/t_N^{1/\beta}, t_N)$. Typically profiles are considered self-similar if they agree to within less than 5% error. Once self-similarity is reached, the final profile can be compared to a non-dimensionalized numerical solution of the thin film equation $H(U)$.

For the case of a supported film of thickness h_1 with a sharp step of thickness h_2 stacked on top, this means fitting the normalized film thickness to the theory:

$$(h(x/t^{1/4}, t) - h_1)/h_2 = H(\alpha U). \tag{2.3}$$

Here α is a fitting parameter and represents the horizontal stretch factor required to match the theory and the experiment. Figure 2.6 shows the measured horizontal stretch factor plotted as a function of annealing time, for a PS film supported on a SiOx/Si substrate. The stretch factor increases as a function of time before coming to a plateau. If the profile is self-similar the stretch factor should be constant. For this sample, only profiles taken at annealing times $\gtrsim 2000$ min should be used to fit to the theory. In the case of a supported film with a no-slip boundary condition, the stretch factor is related to the mobility prefactor as

$$\alpha^4 = \gamma h_0^3/3\eta. \tag{2.4}$$

Ensuring self similarity is essential for the success of a capillary levelling experiment.

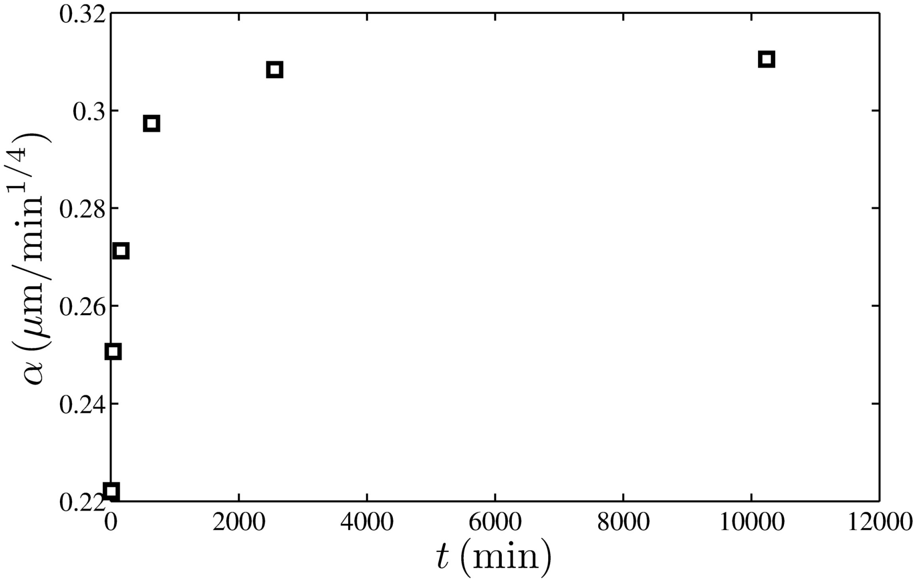

Figure 2.6: The approach towards self-similarity in a capillary levelling experiment performed at 140°C. The horizontal stretch factor α to fit the theory to the experiment is plotted as a function of time. Due to residual stresses in the film, the fit factor changes before reaching a plateau. If an earlier time was used to extract rheological parameters, incorrect values would have been calculated. It is important to use self-similar profiles, where α reaches a plateau.

Using profiles that are not self-similar will give improper values for any rheological parameters that are extracted. If a small difference in annealing times between successive profile measurements is chosen, the profiles might appear falsely self-similar because the step hasn't sufficiently broadened. A good rule of thumb for the supported case is to choose $t_N = 2t_{N-1}$ so that any features will broaden by a factor of $2^{1/4} \approx 1.2$. Measuring a 20% increase in the width of a feature ensures that appreciable flow has occurred, so that it can be determined if the profile is truly self-similar.

For the freestanding films, features broaden with a stronger power law in time, and as a result self-similarity is more easily achieved. The process of fitting to a theoretically calculated profile for a freestanding film is similar to the supported case. However, the measurement of freestanding films with AFM is a difficult experimental challenge. Since the surface profile is measured by tapping the AFM tip onto the surface of the film, vibrations in the freely-suspended can be induced, much like the tapping of a drum head. To avoid noise in the surface profile measurement there are some added precautions that are required for freestanding films. First, the PI parameters that control the feedback loop of the AFM have to be set lower for a freestanding film than in a supported film. For the Veeco Caliber in the Dalnoki-Veress lab, $P \approx 0.2$ and $I \approx 0.02$ worked well. Second, acoustic noise has to be minimized by using a noise insulating cover for the AFM. Finally, the setpoint of the feedback loop has to be carefully monitored to ensure that the tip does not drift away from the surface. AFM measurements of freestanding films were performed for the capillary levelling experiments in Paper IV, and also for the measurements of pores in a polymer membrane in Paper V. In the case of the pore measurements, a difficulty arises when the AFM scans over an open pore. Over the pore the tip experiences no force, and as a result the piezo extends to the end of its range, and the tip is plunged several microns through the pore. The blunt edge on the side of the tip will then run into the opposite edge of the pore which can cause damage to the film. To avoid this unwanted effect, the AFM was mechanically raised so that the piezo was operating near the end of its range for the entire scan. That way when the tip experienced no force, the piezo only extended a small distance and the tip was not plunged through the film.

Chapter 3

Papers

3.1 Paper I - Dewetting and interface potential of a diblock copolymer

Mark Ilton, Pawel Stasiak, Mark W. Matsen, and Kari Dalnoki-Veress "Quantized Contact Angles in the Dewetting of a Structured Liquid", Physical Review Letters, **112**, 068303 (2014).

3.1.1 Preface to Paper I

In this work, we observed droplets of diblock copolymer fluid coexisting with layers of the same fluid. The diblock copolymer droplets were in equilibrium and did not spread on a fluid film of the same material. This phenomenon had previously been observed in a small number of other liquids for sufficiently thin layers of fluid, and had been termed "autophobic" deweting, self dewetting, or pseudopartial wetting. What had not been observed previously was pseudopartial wetting for such thick wetting layers. Compared to other systems where the wetting layer is a few nanometres thick, this diblock copolymer system had droplets coexisting with wetting layers up to 100 nanometres thick. Moreover, we observed that droplets could coexist with any odd integer number of monolayers. In the same sample, we observed droplets coexisting with $\nu = 1, 3, 5, ..., 15$ ordered monolayers.

We measured the contact angle of the diblock copolymer droplets using optical microscopy. Instead of measuring a single contact angle for these droplets, we observed a discrete spectrum of contact angles. The contact angle measured for a given droplet depended on the number of underlying diblock monolayers coexisting with the droplet. Droplets coexisting with a single monolayer $\nu = 1$ had the largest contact angle, while droplets coexisting with $\nu = 3$ monolayers had a smaller contact angle. Having more underlying diblock monolayers coexisting with the droplet, resulted in a smaller droplet contact angle.

The contact angles depended on temperature. As the temperature changed, the spectrum shifted. Droplets coexisting with $\nu > 3$ ordered monolayers had a decreasing contact angle as the temperature increased, while droplets coexisting with $\nu = 1$ ordered monolayer had an increasing contact angle with increasing temperature. For droplets coexisting with $\nu = 3$ diblock monolayers, the behaviour was non-monotonic with temperature.

The diblock copolymer used has an order-disorder transition temperature $T_{\mathrm{ODT}} = 160°\mathrm{C}$. For the temperatures used in these experiments, the polymer should be in the disordered state, where the formation of droplets is favourable. However, interactions with the interfaces induce a local order in the wetting layers. A self consistent field theory calculation of the free energy for a diblock copolymer in the disordered state with an interfacially induced order was performed by our collaborators Pawel Stasiak and Mark Matsen. The calculation revealed that the different temperature dependencies of the contact angle comes from the interplay between the bulk free energy of the film which favours disorder, and the interface contributions which favour order.

In this work, I made the original observation of the dewetting, performed the experiments, analyzed the data, wrote the first draft of the paper, and took part in the revising of the manuscript.

PRL **112,** 068303 (2014) PHYSICAL REVIEW LETTERS week ending 14 FEBRUARY 2014

Quantized Contact Angles in the Dewetting of a Structured Liquid

Mark Ilton,[1] Pawel Stasiak,[2] Mark W. Matsen,[2,3] and Kari Dalnoki-Veress[1,4,*]
[1]*Department of Physics and Astronomy and the Brockhouse Institute for Materials Research,*
McMaster University, Hamilton, Ontario L8S 4M1, Canada
[2]*School of Mathematical and Physical Sciences, University of Reading, Whiteknights, Reading RG6 6AX, United Kingdom*
[3]*Waterloo Institute for Nanotechnology, University of Waterloo, Waterloo, Ontario N2L 3G1, Canada*
[4]*Laboratoire de Physico-Chimie Théorique, UMR CNRS Gulliver 7083, ESPCI, Paris, France*

(Received 3 October 2013; revised manuscript received 10 December 2013; published 14 February 2014)

We investigate the dewetting of a disordered melt of diblock copolymer from an ordered residual wetting layer. In contrast to simple liquids where the wetting layer has a fixed thickness and the droplets exhibit a single unique contact angle with the substrate, we find that structured liquids of diblock copolymer exhibit a discrete series of wetting layer thicknesses each producing a different contact angle. These quantized contact angles arise because the substrate and air surfaces each induce a gradient of lamellar order in the wetting layer. The interaction between the two surface profiles creates an effective interface potential that oscillates with film thickness, thus, producing a sequence of local minimums. The wetting layer thicknesses and corresponding contact angles are a direct measure of the positions and depths of these minimums. Self-consistent field theory is shown to provide qualitative agreement with the experiment.

DOI: 10.1103/PhysRevLett.112.068303 PACS numbers: 82.35.Jk, 68.08.Bc, 68.15.+e

The dewetting of a simple liquid from a solid substrate is a familiar process, such as when water droplets form on the waxy surface of an automobile. Small droplets, where gravity can be ignored, form spherical caps (see schematic in Fig. 1) with a contact angle, θ, given by

$$\Phi(h_{\mathrm{min}}) = \gamma(\cos\theta - 1), \tag{1}$$

where γ is the interfacial tension of the liquid-air surface and $\Phi(h) \equiv [F(h) - F(\infty)]/A$ is the effective interface potential between the two surfaces of the liquid film [1–3]. The latter is defined in terms of the free energy, $F(h)$, of a film with uniform thickness h and area A. In general, dewetting leaves behind a microscopically thin residual wetting layer of thickness h_{min}, corresponding to the minimum in $\Phi(h)$ [3]. For simple liquids such as water, $\Phi(h)$ has a single minimum as illustrated by the dashed curve in Fig. 1, which leads to droplets with a single contact angle. The behavior becomes more interesting for complex liquids such as liquid crystals in their isotropic (disordered) state, where surface-induced smectic (lamellar) order fades towards the center of the film. This should produce a series of minimums in $\Phi(h)$ with decaying depths, resulting in a discrete spectrum of contact angles. Although dewetting is a well-studied phenomenon in physics, these quantized contact angles have never been observed despite some experiments that come tantalizingly close to revealing such behavior [4–7]. Experiments on liquid crystalline polymers have shown a stepwise thinning of the wetting layer [4], a process which occurs reversibly in films of n alkanes [7]. A partial reconstruction of $\Phi(h)$ around its global minimum was performed based on measurements of low molecular weight lubricant oils [5] as well as lamellar-forming diblock copolymers [6]. However, these studies did not observe discrete changes in the contact angle, though theoretically expected. Here, we examine the wetting behavior of a disordered melt of diblock copolymer on a silicon substrate. In this system, the different wetting layers are highly metastable (∼ days), which allows us to accurately resolve the quantized set of equilibrium contact

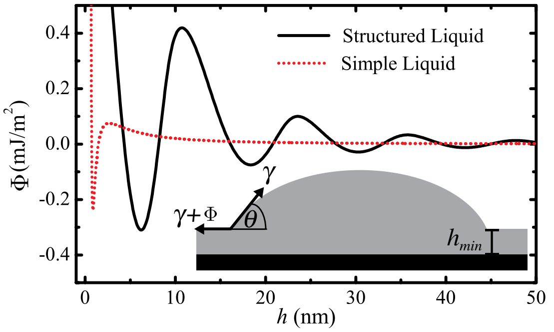

FIG. 1 (color online). Effective interface potential between the surfaces of a film as a function of the film thickness for simple and structured liquids. The inset shows the geometry of our experiment: partial dewetting of a film results in a thin wetting layer with $h = h_{\mathrm{min}}$ corresponding to a minimum in $\Phi(h)$ and a droplet with contact angle θ given by Eq. (1). The dashed curve is for polystyrene on an oxidized silicon substrate [2], and the solid line is calculated for diblock copolymer as described in the text.

© 2014 American Physical Society

angles. Furthermore, self-consistent field theory (SCFT) calculations for structured polymers [8] exhibit qualitative agreement with the experimental observations.

A diblock copolymer is a linear polymer with two blocks of chemically distinct segments, typically labeled A and B [9]; the polymerization index (total number of segments) is denoted by $N = N_A + N_B$ and the composition is specified by $f = N_A/N$. The interaction between the segments is characterized by a dimensionless Flory-Huggins interaction parameter χ, which varies inversely with temperature T. For most A-B combinations, $\chi > 0$, which implies a tendency for the unlike components to segregate into A- and B-rich domains. This tendency depends on the product of the interaction strength and the size of the copolymer chains, χN. When $\chi N \gtrsim 10$ (corresponding to low temperatures), the domains form ordered periodic morphologies with different geometries depending on f. For a symmetric composition ($f = 0.5$), the diblocks self-assemble into thin flat AB monolayers of alternating orientations, which creates a lamellar phase with a period equal to the AB/BA bilayer thickness, L_0. As the temperature increases (χ decreases) beyond the order-disorder transition (ODT) temperature, T_{ODT}, thermal fluctuations destroy the long-range order producing a disordered phase.

In the presence of a flat surface, the domains align to form lamellae parallel to the surface provided that the surface has a sufficient affinity for one of the two components. This can happen even when $T > T_{\mathrm{ODT}}$, although the order of the lamellar layers progressively deteriorates with increasing distance from the surface, resulting in an oscillating concentration profile of period L_0 [10] that decays in amplitude [11–14]. In a thin film, the concentration profiles from opposing surfaces can interfere with each other causing the free energy, $F(h)$, to oscillate with a period of L_0. The preferred thicknesses occur when $h = \nu L_0/2$, where ν is an even integer if the two surfaces have an affinity for the same component (symmetric wetting) and ν is odd if they have affinities for opposite components (asymmetric wetting). The solid curve in Fig. 1 shows the effective interface potential, $\Phi(h) \equiv [F(h) - F(\infty)]/A$, between two surfaces with opposite affinities, where the minimums occur for $\nu = 1, 3, 5, \ldots$. Since the effect of the surfaces diminishes towards the bulk of the film, the minimums become shallower as the film thickness increases. Consequently, the diblock copolymer films tend to dewet one AB/BA bilayer at a time ($\nu \rightarrow \nu - 2$), which should, theoretically, cause discrete jumps in the contact angle, given by Eq. (1), until the minimum thickness ($\nu = 1$) is reached. Although the thicker wetting layers ($\nu > 1$) are only metastable, the barriers between them can be relatively large, and thus, their lifetimes can be exceptionally long ($\sim$ days).

In our experiments, the polystyrene-poly(2-vinylpyridine) (PS-P2VP) diblock copolymer had a total number-averaged molecular weight of $M_n = 16.5$ kg/mol ($N = 158$), a polydispersity index of 1.09, and an equal composition of PS and P2VP (Polymer Source Inc., Canada). From previous studies, we know that $\chi = (97\ \mathrm{K})/T - 0.11$ [15] and $T_{\mathrm{ODT}} \approx 160$°C [14]. Thin films were prepared by spin coating from dilute toluene solutions onto silicon substrates using slow spin-coating speeds (500–1000 rpm) in order to intentionally prepare nonuniform films. The gradients in the surface topography caused instabilities in the film when heated above T_{ODT} in an inert nitrogen environment (see movie in Supplemental Material [16]). The instabilities lead to dewetting with metastable wetting layers of different thicknesses as shown in Fig. 2(a).

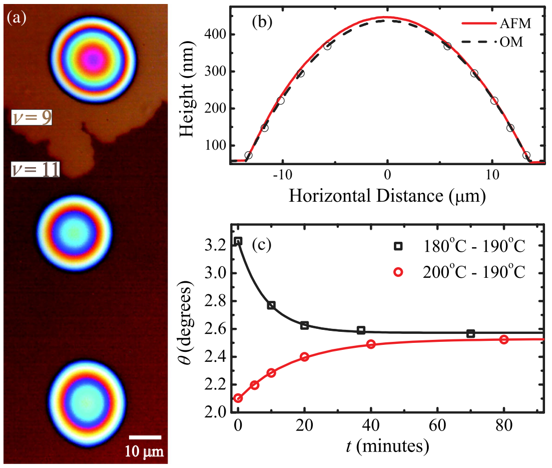

FIG. 2 (color online). (a) Color OM image of PS-P2VP diblock copolymer droplets coexisting with wetting layers of $\nu = 9$ (light brown) and $\nu = 11$ (dark brown). Differences in their contact angles are evident by the spacing of the optical interference rings. (b) Profile of the droplet with the $\nu = 9$ wetting layer measured by AFM (solid red curve) and OM (open circles denote thicknesses obtained from the interference fringes, and the dashed curve is a spherical fit). The heights from AFM and OM agree to within 10 nm, and the resulting contact angles are indistinguishable. (c) Measurements demonstrating that advancing (black squares) and receding (red circles) contact angles converge to within 0.1° in about an hour.

Contact angle measurements were performed with atomic force microscopy (AFM, Veeco, Caliber) and with optical microscopy (OM, Olympus, USA) using a monochromatic filter (460 nm wavelength) to create interference fringes from which the profile of the droplet was inferred [17,18]. AFM and OM yield the same profile to within a few percent resulting in nearly identical values for the contact angle [see Fig. 2(b)]. Consistent with previous measurements [17], the AFM error signal shows steps near the contact line, indicating a small amount of residual order at the base of the droplets. Since the OM measurements are more easily performed, results were predominantly obtained using this technique. Both advancing and receding contact angles were measured and were in agreement to within 0.1° [see Fig. 2(c)], indicating that our measurements are of the equilibrium contact angle and free from hysteresis or pinning effects. The metastable wetting layers were generally stable for several days, whereas the typical relaxation time for a droplet to reach its equilibrium contact angle is on the order of an hour [see Fig. 2(c)].

Dewetting was observed for temperatures ranging from 190°C to 240°C, well above $T_{\mathrm{ODT}} \approx 160\,^{\circ}\mathrm{C}$, and for wetting layer thicknesses from $\nu = 1$ to 15 ($h \approx 7$ to 96 nm). The contact angles ranged from 0.5° (the lower limit of our measurement technique) for the thickest wetting layer to 8.5° for the stable $\nu = 1$ wetting layer. As shown in Fig. 3(a), there is a spectrum of discrete contact angles indicating multiple minimums in the effective interface potential [Eq. (1)] corresponding to different values of ν. As the temperature is changed, the energy spectrum shifts. For thicker wetting layers, the contact angle decreases as a function of increasing temperature, while a more complex dependence is found for thinner wetting layers.

In order to develop a more complete understanding of the results, we calculate the free energy, $F(h)$, of a uniform film of symmetric diblock copolymer as a function of film thickness, h, using the standard SCFT for incompressible Gaussian chains [8]. Note that our calculations assume conformational symmetry, where the A and B segments occupy the same volume, ρ_0^{-1}, and have equal statistical segment lengths, a. Different values of temperature in the disordered phase, $T > T_{\mathrm{ODT}}$, are produced by varying $\chi N < 10.495$. The substrate and air surfaces were treated by imposing reflecting boundaries with delta-function potentials acting on the two polymer components, as described previously [19,20]. The affinity of the substrate for A-type segments was controlled by the dimensionless parameter, $\Lambda_{\mathrm{sub}} = (\gamma_{\mathrm{sub}/A} - \gamma_{\mathrm{sub}/B})/2k_B T \rho_0 a N^{1/2}$, where $\gamma_{\mathrm{sub}/\alpha}$ is the surface tension between the substrate and the $\alpha = A$ or B polymer component [19,21]. Likewise, an analogous parameter, Λ_{air}, was defined for the air surface, which we chose with an opposite sign so as to reproduce the asymmetric wetting conditions of the experiment. To match the strong surface affinities characteristic of the experiment, the dimensionless amplitudes were chosen large enough ($\Lambda_{\mathrm{sub}} N = -0.3$ and $\Lambda_{\mathrm{air}} N = 0.3$) such that the concentration of A and B segments at the substrate and air surfaces, respectively, were relatively pure. Increasing the affinities beyond these magnitudes had little effect on the contact angles.

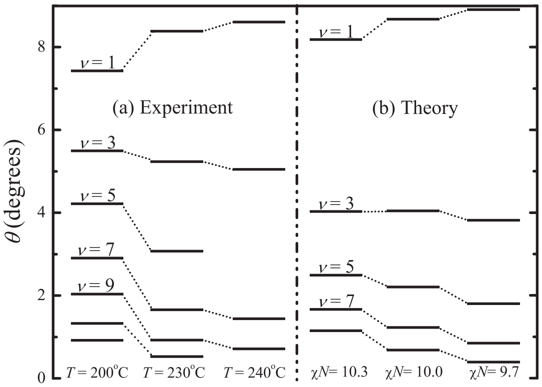

FIG. 3. The spectrum of quantized contact angles θ, shown for different numbers of diblock monolayers, ν, in the wetting layer. (a) Experimental and (b) theoretical results are presented for several different temperatures and values of χN, respectively.

The SCFT is performed in terms of reduced parameters such as $h/aN^{1/2}$ and $F(h)/nk_B T$, where n is the total number of molecules in the film. In order to explicitly evaluate $\Phi(h) \equiv [F(h) - F(\infty)]/A$ as a function of h, we estimated the volume occupied by a single diblock copolymer to be $N/\rho_0 \approx 26\ \mathrm{nm}^3$ and the average end-to-end of an unperturbed diblock to be $aN^{1/2} \approx 8.9$ nm [22]. The solid curve in Fig. 1 shows $\Phi(h)$ calculated for $\chi N = 10.3$. As expected, $\Phi(h)$ exhibits a series of minimums with decaying depths corresponding to odd-integer values of ν. Using Eq. (1) with an average air/polymer surface tension of $\gamma \equiv (\gamma_{\mathrm{air}/A} + \gamma_{\mathrm{air}/B})/2 \approx 31\ \mathrm{mJ/m^2}$ [23], we can then extract a contact angle, θ, for each of the free energy minimums.

In Fig. 3(b), the theoretical spectrum for θ is shown for three different values of χN, and compared to the experimental results in Fig. 3(a). The experimental and theoretical results all show a monotonic decrease with ν. Furthermore, there is an increase in the difference between the contact angles for $\nu = 1$ and $\nu = 3$ as the system becomes more disordered, indicating a complex dependence of the contact angle on temperature. The temperature dependence of the interface potential inferred by the experiment [obtained by measuring θ and making use of Eq. (1)] is shown in Fig. 4(a). Here, the data for $\nu = 1$ have been omitted because they exhibit a larger scatter, which we attribute to a partial ordering of the droplets close to the

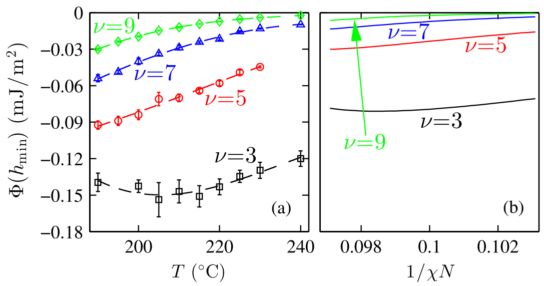

FIG. 4 (color online). The effective interface potential plotted as a function of (a) temperature for the experiments and (b) $1/\chi N$ for theory. Results are shown for wetting layers with different numbers of diblock monolayers, ν. Further results up to $\nu = 15$ are provided in the Supplemental Material, Fig. S1 [16].

substrate as well as droplets pinning to small residual areas of $\nu = 3$ where an extra bilayer has not fully dewetted (see Figs. S2–S3 in the Supplemental Material [16]). The corresponding results from SCFT calculations are plotted in Fig. 4(b), with the temperature dependence mimicked by $(\chi N)^{-1}$. The calculations are in good qualitative agreement with the experimental data. For $\nu \geq 5$, the contact angle decreases monotonically as a function of T for the experiment or $(\chi N)^{-1}$ for the theory. Interestingly, this dependence becomes nonmonotonic at $\nu = 3$ in both theory and experiment. A complete data set from $\nu = 1$ to 15 is presented in the Supplemental Material (see Fig. S1) [16]. In addition to our results for PS-P2VP diblocks, we have observed similar behavior for PS-PMMA diblocks (see Supplemental Material, Fig. S4 [16]) where the substrate has a strong affinity for PMMA while the air has only a slight affinity for PS, which illustrates the generality of our observations.

This behavior is best observed at temperatures just above the ODT. At higher temperatures, the metastable minimums in $\Phi(h)$ will be too short lived to observe their contact angles. However, it is also essential that the system remains above the ODT so that $\Phi(h) \to 0$ as $h \to \infty$, or else there will be no driving force for films to dewet. Indeed, droplets of ordered diblock copolymer are known to slowly spread [24], indicative of the fact that they do not possess an equilibrium contact angle.

The physics of this dewetting behavior is relatively simple. The affinities of the substrate and air surfaces favor the formation of ordered lamellae so as to minimize the surface energy, but entropy favors disorder given that $T > T_{\mathrm{ODT}}$. So as to minimize the number of ordered layers in a thin film while still maintaining the order next to the two surfaces, polymer is transferred from the film to the droplet where it can exist in a disordered state of lower free energy. The increased preference for thinner wetting layers (i.e., smaller h_{min}) causes a quantized reduction in the effective interface potential. This leads to a change in the force balance at the contact line of the droplets, driving flow of material from the edge of the droplets towards their centers and, thus, a monotonic increase in θ with decreasing ν (see Fig. 3). The complicated temperature dependence of θ (see Fig. 4), on the other hand, is difficult to explain because of the numerous competing effects, such as the free energy difference between the ordered and disordered phases, the surface energies, and the decay length of the surface ordering. Nevertheless, SCFT captures the qualitative features. We note that accurate quantitative predictions should not be expected from SCFT because the mean-field approximation ignores composition fluctuations, which become important in the disordered phase [25].

The wetting layer is generally very thin for simple liquids, whereas it can be more than an order of magnitude thicker for structured liquids (compare the locations of the minimums in Fig. 1 for the two cases). It is for this reason that researchers [4,6,26] have referred to the latter case as autophobic dewetting, meaning that the droplet dewets from what is essentially itself. In true instances of autophobic dewetting, such as a homopolymer dewetting from a chemically identical polymer brush [27–34] or elastomer [35–37], the droplet actually sits on top of a polymeric substrate which is anchored. In contrast, the wetting layer here does not extend beneath the droplet but rather coexists side-by-side with the droplet. Although there are ordered layers at the base of the droplet, the number of layers and their detailed composition profile are distinct from those of the wetting layer. For instance, all three droplets in Fig. 2(a) would possess identical microstructure next to the substrate despite being in contact with two different wetting layers ($\nu = 9$ and 11). The only effect of ν, or rather the depth of the effective interface potential $\Phi(h_{\mathrm{min}})$, is to modify the amount of force pushing material into the droplet, which in turn alters the Laplace pressure inside the droplet and, thus, the curvature of the polymer-air surface.

In summary, we have discovered a series of quantized contact angles when a film of structured isotropic liquid dewets from a solid substrate, specifically a disordered melt of diblock copolymer from a silicon wafer. The behavior results from a subtle competition between surface interactions that tend to order the film and entropy which favors the disordered state. Because the induced order is unfavorable above the ODT temperature, the film dewets so as to produce droplets of disordered diblock copolymer. The wetting layer left behind remains relatively ordered, and consequently, it forms, in our case, an odd number of diblock monolayers ($\nu = 1, 3, \ldots, 15$). Since the surface-induced order decays at temperatures above the ODT, the monolayers at the center of a thick wetting layer will be somewhat disordered, and therefore, the tendency to dewet is relatively weak, resulting in a small contact angle. However, as the wetting layer thins, it becomes more ordered throughout, and consequently, the contact angle increases. It is this increase in contact angle due to the improved order of thinner wetting layers coupled with the step changes in thickness that creates the discrete spectrum of contact angles. We were able to observe the different angles with remarkable accuracy due to the long lifetimes of the metastable wetting layers ($\nu > 1$). In fact, the lifetimes were sufficient for us to carefully probe temperature dependence. Given that the set of θ and h_{min} is such a direct and accurate measure of the free energy, these experiments will provide a superb test for future calculations beyond SCFT [38,39]. Furthermore, the physics of this new dewetting behavior is reasonably generic to structured liquids, and thus, we expect it to occur in numerous other systems beyond the two lamellar diblock copolymer examples used in this Letter.

Financial support for this work was provided by NSERC (Canada) and EPSRC (U.K.).

[*] dalnoki@mcmaster.ca

[1] A. N. Frumkin, J. Phys. Chem. **12**, 337 (1938).
[2] R. Seemann, S. Herminghaus, and K. Jacobs, Phys. Rev. Lett. **86**, 5534 (2001).
[3] K. Jacobs, R. Seemann, and S. Herminghaus, in *Polymer Thin Films*, edited by O. K. C. Tsui and T. P. Russell (World Scientific, Singapore, 2008), Chap. 10, pp. 243–265.
[4] S. Sheiko, E. Lermann, and M. Möller, Langmuir **12**, 4015 (1996).
[5] R. Waltman, A. Khurshudov, and G. Tyndall, Tribol. Lett. **12**, 163 (2002).
[6] R. Limary, P. F. Green, and K. R. Shull, Eur. Phys. J. E **8**, 103 (2002).
[7] P. Lazar, H. Schollmeyer, and H. Riegler, Phys. Rev. Lett. **94**, 116101 (2005).
[8] M. W. Matsen, J. Phys. Condens. Matter **14**, R21 (2002).
[9] F. S. Bates, Science **251**, 898 (1991).
[10] Near an interface which has a chemical preference for one of the two blocks, the lamellar spacing increases slightly from its equilibrium bulk value L_0 and is a function of the distance from the interface.
[11] G. H. Fredrickson, Macromolecules **20**, 2535 (1987).
[12] A. Menelle, T. P. Russell, S. H. Anastasiadis, S. K. Satija, and C. F. Majkrzak, Phys. Rev. Lett. **68**, 67 (1992).
[13] P. Mansky, T. P. Russell, C. J. Hawker, J. Mays, D. C. Cook, and S. K. Satija, Phys. Rev. Lett. **79**, 237 (1997).
[14] A. B. Croll, A.-C. Shi, and K. Dalnoki-Veress Phys. Rev. E **80**, 051803 (2009).
[15] A. B. Croll, M. W. Matsen, A.-C. Shi, andK. Dalnoki-Veress, Eur. Phys. J. E **27**, 407 (2008).
[16] See Supplemental Material at http://link.aps.org/supplemental/10.1103/PhysRevLett.112.068303 for a time-lapsed video of the droplet instability and supplemental Figs. S1–S4.
[17] A. B. Croll and K. Dalnoki-Veress, Eur. Phys. J. E **29**, 239 (2009).
[18] S. Cormier, J. McGraw, T. Salez, E. Raphaël, and K. Dalnoki-Veress, Phys. Rev. Lett. **109**, 154501 (2012).
[19] M. W. Matsen, Macromolecules **39**, 5512 (2006).
[20] We neglected the long-range van der Waals interaction in our SCFT calculations because for PS-P2VP diblock copolymers this interaction only contributes a small correction to the effective interface potential. Including the van der Waals interaction would result in a $< 1°$ reduction in the contact angles for $\nu = 1$; the effect becomes negligible for the thicker wetting layers ($\nu = 3, 5, \ldots$).
[21] M. W. Matsen, J. Chem. Phys. **106**, 7781 (1997).
[22] L. J. Fetters, D. J. Lohse, D. Richter, T. A. Witten, and A. Zirkel, Macromolecules **27**, 4639 (1994).
[23] B. B. Sauer and G. T. Dee, Macromolecules **35**, 7024 (2002).
[24] A. B. Croll, M. V. Massa, M. W. Matsen, and K. Dalnoki-Veress, Phys. Rev. Lett. **97**, 204502 (2006).
[25] F. S. Bates, J. H. Rosedale, G. H. Fredrickson, and C. J. Glinka, Phys. Rev. Lett. **61**, 2229 (1988).
[26] M. W. J. van der Wielen, M. A. Cohen Stuart, and G. J. Fleer, Langmuir **14**, 7065 (1998).
[27] R. Yerushalmi-Rozen, J. Klein, and L. J. Fetters, Science **263**, 793 (1994).
[28] G. Reiter, P. Auroy, and L. Auvray, Macromolecules **29**, 2150 (1996).
[29] G. Reiter and R. Khanna, Phys. Rev. Lett. **85**, 5599 (2000).
[30] G. Reiter and R. Khanna, Langmuir **16**, 6351 (2000).
[31] A. Voronov and O. Shafranska, Langmuir **18**, 4471 (2002).
[32] J. H. Maas, G. J. Fleer, F. A. M. Leermakers, and M. A. Cohen Stuart, Langmuir **18**, 8871 (2002).
[33] G. Reiter, Macromol. Symp. **229**, 81 (2005).
[34] W. Béziel, G. Reiter, E. Drockenmuller, R.-V. Ostaci, S. Al Akhrass, F. Cousin, and M. Sferrazza, Europhys. Lett. **90**, 26008 (2010).
[35] T. Kerle and J. Klein, Europhys. Lett. **38**, 207 (1997).
[36] T. Kerle, R. Yerushalmi-Rozen, and J. Klein, Macromolecules **31**, 422 (1998).
[37] J. Jopp and R. Yerushalmi-Rozen, Macromolecules **32**, 7269 (1999).
[38] J. Qin and D. C. Morse, Phys. Rev. Lett. **108**, 238301 (2012).
[39] E. M. Lennon, K. Katsov, and G. H. Fredrickson, Phys. Rev. Lett. **101**, 138302 (2008).

Supplementary information to "Quantized contact angles in the dewetting of a structured liquid"

Mark Ilton,[1] Pawel Stasiak,[2] Mark W. Matsen,[2,3] and Kari Dalnoki-Veress[1,4,*]

[1]*Department of Physics & Astronomy and the Brockhouse Institute for Materials Research,*
McMaster University, Hamilton, Ontario, Canada
[2]*School of Mathematical and Physical Sciences,*
University of Reading, Whiteknights, Reading, U.K.
[3]*Waterloo Institute for Nanotechnology,*
University of Waterloo, Waterloo, Ontario, Canada
[4]*Laboratoire de Physico-Chimie Théorique,*
UMR CNRS Gulliver 7083, ESPCI, Paris, France

(Dated: October 3, 2013)

THE DEWETTING PROCESS

For thin films of PS-P2VP, dewetting was observed for all $T \geq 180$°C. The first supplemental movie (SupplementalMovie1.mp4) shows a time-lapsed optical microscopy video of a film dewetting over the course of ~ 24 hours at 180°C. The image focuses on a small area (~ 1 mm $\times$ 1 mm) near the edge of the sample, where a relatively thin region of the film is surrounded by a thicker region that appears bright. The thinner part of the film in the middle of the image exhibits discrete changes in brightness, which correspond to steps of partially ordered lamellae. As the sample is annealed, two processes occur. Firstly, the relatively flat areas of the film undergo layer-by-layer dewetting down to $\nu = 7$ ordered monolayers after the 24 hours of annealing. Secondly, areas possessing large gradients in thickness experience a Plateau-Rayleigh type instability and break up into droplets. The final state of the film at the end of the movie, after the initial annealing procedure, contains wetting layers of different thicknesses, which are labeled by the number of ordered monolayers, ν. The second supplemental movie (SupplementalMovie2.mp4) shows a different sample undergoing the initial annealing procedure over the course of 28 hours at 190°C

FULL EXPERIMENTAL RESULTS

For simplicity of presentation, the experimental results for PS-P2VP droplets in figure 4 of the main text were only shown for wetting layers up to $\nu = 9$. Here, figure S1 plots the experimentally measured contact angle as a function of temperature for all values of ν. For the thicker ordered layers where $\nu \geq 5$, the contact angle monotonically decreases with increasing temperature. In the case of the thickest wetting layers, the contact angle becomes too small to measure with optical microscopy; the technique is unable to resolve contact angles less than $\sim 0.5°$. As the wetting layer becomes thinner, the contact angle shows a non-monotonic temperature dependence, and increases as a function of temperature at $\nu = 1$. Figure S2 shows the contact angle with experimental error for the three thinnest wetting layers ($\nu = 1$, 3, and 5). The large scatter in the contact angles measured at $\nu = 1$ is likely due to the pinning of droplets onto areas of $\nu = 3$ that did not fully dewet. For example, figure S3 shows an optical microscopy image of droplets next to $\nu = 1$ ordered layers. The droplets show pinning at the contact line, which resulted in non-spherical cap morphologies. This pinning was not observed for thicker wetting layers, which is reflected by the smaller uncertainty in the contact angles measured for $\nu \geq 3$.

COMPARISON TO PS-PMMA

To probe the generality of the experimental results, we chose to study a second diblock copolymer system, polystyrene-poly(methyl methacrylate) (PS-PMMA). Samples of PS-PMMA with $M_n = 20,000$ g/mol and polydispersity index of 1.05, and an equal composition of PS and PMMA (Polymer Source Inc., Canada) were prepared in the same way as the PS-P2VP samples described in the main text. The molecular weight used here is similar to that used in a previous study of the effective interface potential of PS-PMMA near a $\nu = 1$ ordered substrate layer [1]. For PS-PMMA, χ is relatively insensitive to temperature compared to PS-P2VP [2] and is deeper in the disordered state with $\chi N \approx 8$ for the molecular weight used here. After annealing at 160°C in an inert environment, we observed droplets coexisting with wetting layers of ν = 1, 3, and 5. Droplets were not observed for thicker wetting layers, which is consistent with the system being further above ODT than the PS-P2VP one where droplets were observed up to $\nu = 15$. The contact angles of the PS-PMMA droplets were measured using the same technique as described in the main text. Figure S4 plots the experimentally measured contact angles as a function of temperature for the three different values of ν. Consistent with the PS-P2VP system, the PS-PMMA droplets show a monotonic decrease in contact angle with increasing temperature for the thickest ordered layers, with non-monotonic temperature dependence emerging as ν decreases. The absolute values of the contact angle are lower for PS-PMMA, which is consistent with PS-PMMA having a lower average surface tension than the PS-P2VP.

In order to compare the temperature dependence of PS-P2VP and PS-PMMA, the SCFT calculation described in the main text was extended further into the disordered phase (lower values of χN). The calculated contact angles are shown as a function of $1/\chi N$ in figure S5. Qualitatively, the PS-P2VP data from figure S1 corresponds well with the $1/\chi N$ interval immediately above the ODT, indicated by the arrows at the top of figure S5. The experimental PS-PMMA data in figure S4, on the other hand, is consistent with an interval further to the right deeper into the disordered phase, just as we would expect based on our estimated value of $\chi N \approx 8$. Hence, the SCFT captures the qualitative temperature dependence of

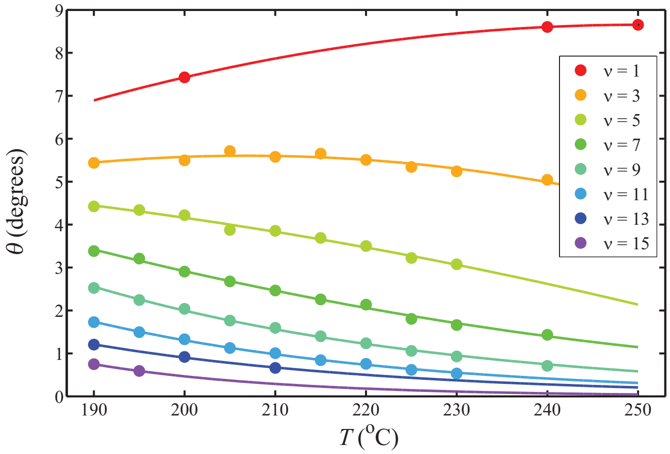

FIG. S1. The contact angle of dewetted PS-P2VP droplets plotted as a function of temperature for all observed residual wetting layer thicknesses. The circles are the experimentally measured contact angles and the solid lines are guides to the eye.

both materials, albeit in different regions of the disordered phase.

---

* dalnoki@mcmaster.ca

[1] R. Limary, P. F. Green, and K. R. Shull, The European Physical Journal E, **8**, 103 (2002), ISSN 1292-8941.

[2] T. Russell, R. H. Jr, and P. Seeger, Macromolecules, **23**, 890 (1990).

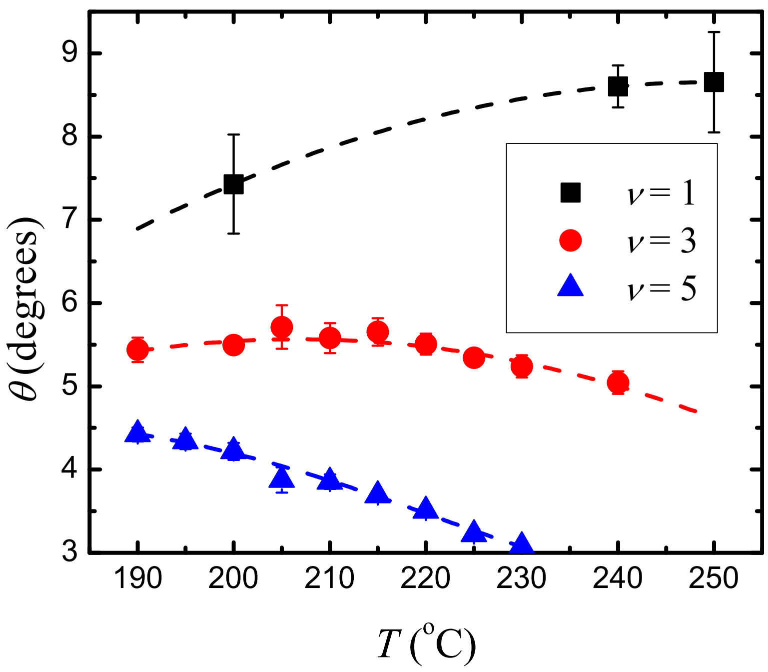

FIG. S2. Measured contact angles of PS-P2VP droplets with experimental error for $\nu = 1$, 3, and 5. The contact angle measurements of droplets coexisting with a $\nu = 1$ wetting layer showed a large scatter.

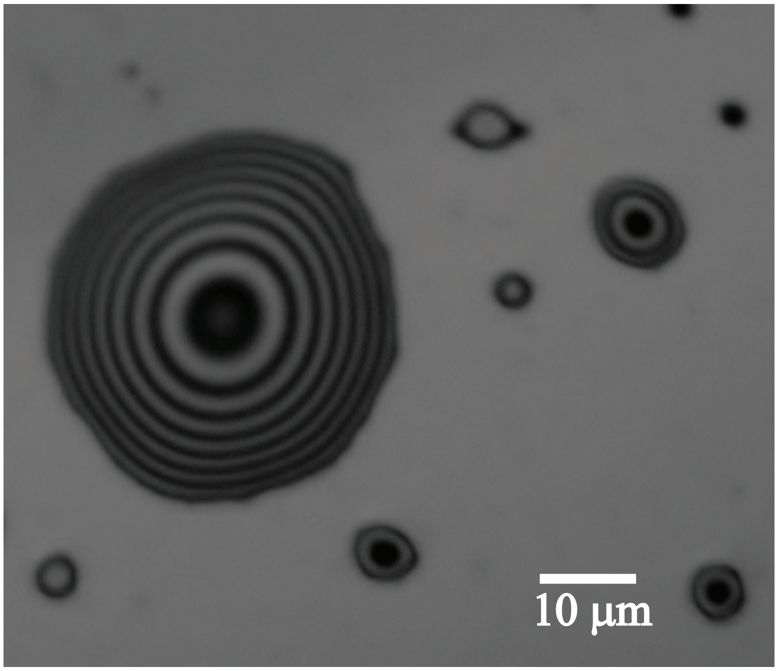

FIG. S3. An optical microscopy image of PS-P2VP droplets coexisting with a $\nu = 1$ wetting layer. The droplets show pinning at their edges.

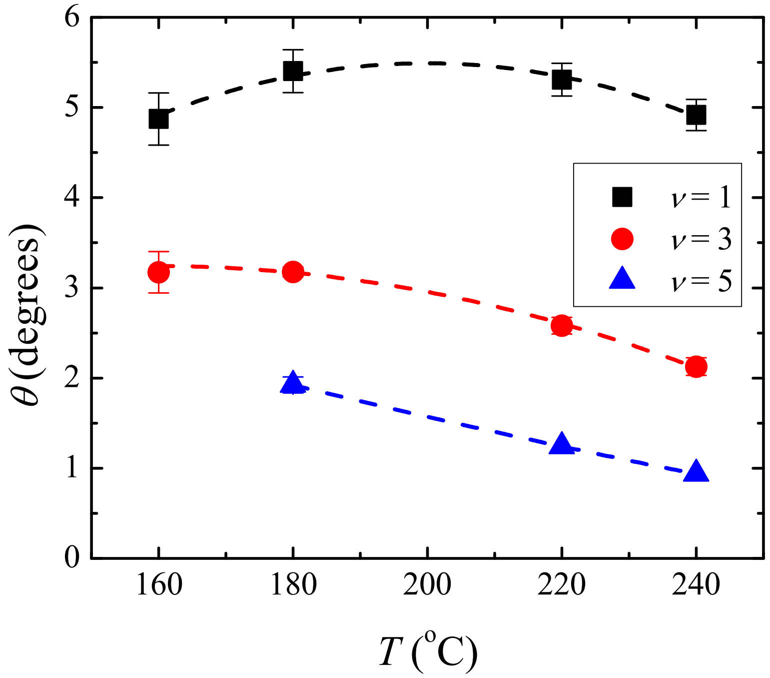

FIG. S4. Contact angle of PS-PMMA droplets shown as a function of contact angle. Results are shown for all layers that droplets were observed.

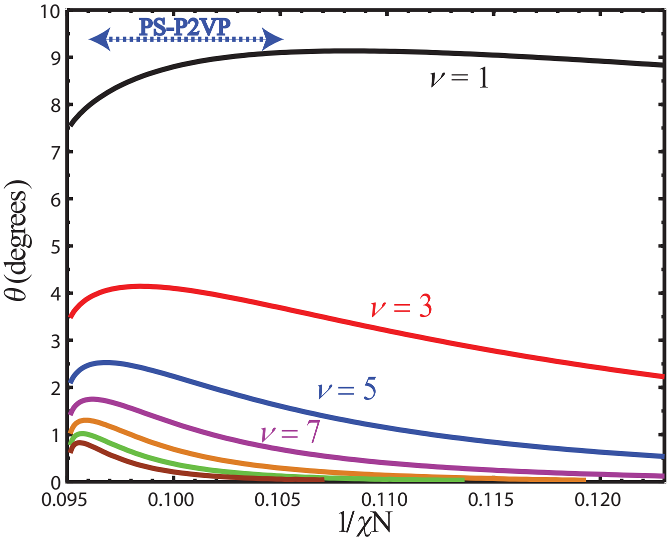

FIG. S5. The calculated contact angle from SCFT plotted as a function of $1/(\chi N)$ for PS-P2VP. The range of χN presented here is greater than was shown in Fig. 3 of the main text.

3.2 Paper II - Droplet spreading of a diblock copolymer

Mark Ilton, Oliver Bäumchen, and Kari Dalnoki-Veress "Onset of Area-Dependent Dissipation in Droplet Spreading", Physical Review Letters, **115**, 046103 (2015).

3.2.1 Preface to Paper II

In this paper we used the diblock copolymer system from Paper I to study the dynamics of partial wetting. Previous studies of partial wetting dynamics had found that the viscous energy dissipation scales with the length of the contact line, which is proportional to the perimeter or radius of the droplet. This is due to the large shear strain rates at the thin wedge of fluid near the edge of the droplet. One difficulty that plagues experiments on partially wetting fluids is contact line pinning. Any defects on the substrate can create regions where the contact line is impeded, which causes a longer measured relaxation time for droplets going to their final state.

The dewetted diblock copolymer provided an excellent system to study partial wetting dynamics. Nature provides a system in which the droplets spontaneously form and coexist with the same fluid. There are comparatively fewer defects in these films than for a system which is manually prepared.

A dynamic measurement was performed as follows. A droplet was monitored at a fixed temperature to ensure that it started in equilibrium. Then, the temperature was quickly changed by 10°C. From Paper I, the equilibrium contact angle of a droplet depends on the temperature, and so the equilibrium contact angle of the droplet changes with the 10°C temperature jump. Since the droplet has a large viscosity, it takes time for the droplet to respond and come to its new equilibrium contact angle. The relaxation of the droplet contact angle was found to be an exponential decay. By measuring the contact angle of the droplets as they approached their new equilibrium angle, a relaxation time could be extracted by fitting the evolution of the contact angle in time to an exponential decay.

For partially wetting fluids this relaxation time depends on three parameters: the capillary velocity of the fluid $v_c = \gamma/\eta$, the droplet volume, and the equilibrium contact angle. Another remarkable feature of the diblock copolymer system is that all three of these parameters could be tuned on the exact same sample: The capillary velocity could be changed by changing temperature. For any given sample, there were hundreds of droplets with different volume. As well, the equilibrium contact angle could be varied because there was a spectrum of contact angles.

We found that the relaxation time of the droplets was not consistent with a contact line scaling of the dissipation as it is for other partially wetting fluids. The dissipation depended on the base area of the droplets for this diblock copolymer fluid. This is consistent with the onset of an effective slip boundary condition at the liquid-solid interface, which we postulate is related to the anisotropy of the diblock copolymer molecules.

For this work I designed and performed the experiments, analyzed the data, developed a generalized model to describe the dissipation, wrote the first draft of the paper, and was involved in the revision of the manuscript.

PRL **115,** 046103 (2015) PHYSICAL REVIEW LETTERS week ending 24 JULY 2015

Onset of Area-Dependent Dissipation in Droplet Spreading

Mark Ilton,[1] Oliver Bäumchen,[2] and Kari Dalnoki-Veress[1,3,*]

[1]*Department of Physics and Astronomy and the Brockhouse Institute for Materials Research, McMaster University, Hamilton, Ontario L8S 4M1, Canada*

[2]*Max Planck Institute for Dynamics and Self-Organization (MPIDS), 37077 Göttingen, Germany*

[3]*Laboratoire de Physico-Chimie Théorique, UMR CNRS 7083 Gulliver, ESPCI ParisTech, PSL Research University, Paris, France*

(Received 16 January 2015; revised manuscript received 27 May 2015; published 22 July 2015)

We probe the viscous relaxation of structured liquid droplets in the partial wetting regime using a diblock copolymer system. The relaxation time of the droplets is measured after a step change in temperature as a function of three tunable parameters: droplet size, equilibrium contact angle, and the viscosity of the fluid. Contrary to what is typically observed, the late-stage relaxation time does not scale with the radius of the droplet—rather, relaxation scales with the radius squared. Thus, the energy dissipation depends on the contact area of the droplet, rather than the contact line.

DOI: 10.1103/PhysRevLett.115.046103 PACS numbers: 68.08.Bc, 47.55.D-, 68.15.+e, 82.35.Gh

The dynamics of a liquid wetting a solid substrate has applications in diverse technologies including oil recovery [1], coating deposition [2], electronic paper [3], capillary switches [4], and microfluidics [5]. Flow in liquids can be driven by a number of forces (e.g., gravity, surface tension, external electromagnetic fields), which are mediated by inertial and viscous forces in the fluid. Large inertial forces can lead to oscillatory motion [6–17], whereas viscous forces cause damping. The study of the viscous (i.e., low Reynold's number) motion of wetting fluids has been the focus of much research because it is typically dominant at the micrometer and nanometer length scales (for reviews see Refs. [18–23]), and it is the subject of the current Letter. For a viscous liquid droplet that wets a substrate there are two possible cases: complete wetting and partial wetting depending on the presence and interplay of short- and long-ranged intermolecular forces in the system [24]. In the case of complete wetting, the final equilibrium state is that of a flat liquid film of uniform thickness covering the substrate. The dynamics of this process is well understood in both the case of an initially dry substrate [24,25], as well as the case where the substrate is covered by a prewetted film of the same liquid [26]. On the other hand, in partial wetting the final equilibrium state is a droplet that makes a well-defined equilibrium contact angle θ_e with the substrate [24]. In this case, the dynamics of a droplet as it moves towards equilibrium is less well understood and there are unresolved fundamental questions [21], in particular involving the nature of energy dissipation as a droplet spreads.

Exponential relaxation is a generic feature of near-equilibrium partial wetting, having been observed in capillaries [27,28], droplet coalescence [29–31], stripe spreading [32], and droplet spreading [30,33–35]. For a system with a well-defined volume Ω the relaxation time τ of the exponential decay is a function of Ω, θ_e, and the fluid viscosity η. In the limit of small contact angles, there are several different predictions for $\tau(\Omega, \theta_e, \eta)$ [32,34–39], but there is a dearth of experimental systems where τ can be systematically probed as a function of all three variables. The lack of experiments is largely due to the fact that contact angle pinning is the bane of careful dynamics measurements especially at small contact angles [40] and can occur at even dilute concentrations of defects [41].

Here, we use a liquid-substrate system that allows the systematic probing of partially wetting droplets that coexist with a nanoscopically thin layer of the same liquid (known as pseudopartial wetting [42,43]), as shown schematically in Fig. 1(a). Droplets with a well-defined θ_e coexisting in equilibrium with a prewetted layer can arise from a single global minimum (or even multiple minima in the case of stratified films [44]) of the effective interface potential, i.e., the free energy of the system comprising repulsive and attractive intermolecular interactions. Little is known about the dynamics of moving contact lines in the partial wetting regime with a prewetting layer [45]. The dynamics depends on whether there is enough material to fully prewet the substrate [46,47], and previous measurements of liquids in a capillary subjected to a pressure difference saw no evidence of contact line pinning in the case of a prewetting layer, a problem that is common in partial wetting [45].

The system investigated here has negligible contact angle hysteresis [44] and is ideally suited to probe the exponential relaxation of droplets near equilibrium. The lack of hysteresis results from the self-assembly of the droplets on a metastable wetting layer of the same material (rather than defect prone manual preparation). We use a lamellar-forming diblock copolymer that dewets into droplets with a quantized spectrum of contact angles. While the details of the quantized droplet system can be found in our earlier study [44], we recall some of the salient features crucial to this work. The diblock copolymer liquid can self-assemble into stacks of monolayers below the

© 2015 American Physical Society

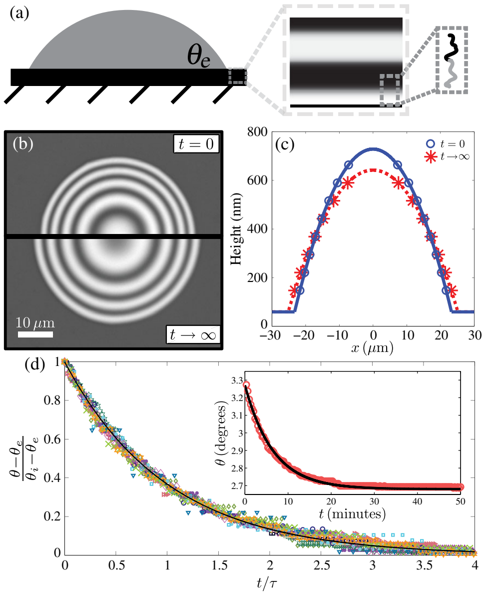

FIG. 1 (color online). (a) Schematic of a mostly disordered droplet, coexisting with an ordered wetting layer of the same liquid. (b) Interference optical microscopy images showing the relaxation of a droplet as it spreads. (c) Best fit spherical cap to the data points from the interference fringes of the droplet in (b) at $t = 0$ (solid line) and at equilibrium as $t \to \infty$ (dashed line). The height scale is exaggerated as compared to the lateral scale for clarity. (d) Normalized relaxation of the contact angle of 15 different representative droplets with different Ω and θ_e, which undergo both advancing and receding motion. The solid line is the function $\exp(-t/\tau)$. The inset shows the relaxation of the contact angle of the droplet from (b) and (c) as a function of time with an exponential fit (black line).

order-disorder transition temperature T_{ODT}, whereas order is destroyed above T_{ODT}. In our experiments we work above T_{ODT}; however, the substrate-liquid and air-liquid interactions have a tendency to induce local ordering. Thus, one can arrange the temperature of the experiment such that a mostly disordered "bulklike" droplet coexists with a wetting layer made up of a stack of monolayers [see the schematic in Fig. 1(a)]. The wetting layer thickness h_e and temperature T determine the free energy of the wetting layer. As a result, the droplet contact angle depends on h_e and T. An increase in T reduces the order in the wetting layer, resulting in a smaller θ_e, and the droplet spreads. Similarly, a decrease in T causes a droplet to recede. Because a change in temperature shifts θ_e, we can examine both advancing and receding droplet motion in a controlled manner simply by performing a step change in the temperature. Thus, we are able to systematically vary Ω, θ_e, and η using a single liquid on a homogeneous substrate with no chemical modification. By measuring the relaxation time of droplets as they approach equilibrium, one can probe the nature of energy dissipation in the droplets.

Previous work has shown that in the case of a simple liquid droplet on a substrate with a small contact angle the majority of the energy dissipation occurs near the contact line, where there is the greatest shear [20]. For late-stage relaxation, the instantaneous contact angle θ exponentially decays to θ_e with a relaxation time [20,38,48] (see the Supplemental Material [49])

$$\tau_L \propto \frac{\eta\,\Omega^{1/3}}{\gamma\,\theta_e^{10/3}}, \tag{1}$$

where γ is the liquid-air surface tension. To probe the energy dissipation in a structured liquid and the role of the prewetting layer, we examine the near-equilibrium ($\theta \approx \theta_e$) dynamics of droplets. We will show that, in contrast with the assumptions made leading to Eq. (1), the relaxation of the droplets is consistent with a contact area dependent dissipation mechanism being dominant.

As described previously [44], thin films of polystyrene-poly(2 vinyl pyridine) (PS-P2VP) diblock copolymer were spincast onto silicon wafers from a dilute solution of toluene at slow speeds to purposefully create films of nonuniform thickness (the PS-P2VP was obtained from Polymer Source Inc., Canada, $M_n = 16.5$ kg/mol with an equal block composition). Upon heating above $T_{\mathrm{ODT}} = 160\,^\circ\mathrm{C}$ the liquid dewets into droplets coexisting with ordered wetting layers. The contact angle of the droplets was measured from Newton rings using optical microscopy with a monochromatic filter (460 nm) as shown in Fig. 1(b) [26]. A relaxation measurement was performed as follows. The sample temperature is controlled using a high-precision ($\pm 0.1\,^\circ\mathrm{C}$) heating device (Linkam, UK). First, a droplet was held at $T = T_i$ until it reached its equilibrium initial contact angle θ_i. At time $t = 0$, the temperature of the system was changed by $10 \pm 0.1\,^\circ\mathrm{C}$ to T_f. The temperature equilibrates rapidly (within 10 sec) compared to the measurement time (tens of minutes). $\theta(t)$ was measured until the droplet reached its new equilibrium contact angle θ_e. Figures 1(b)–1(d) show a typical measurement of a droplet with an initial contact angle of 3.29°, just as the temperature is rapidly changed from 180 to 190 °C. The approach to the equilibrium contact angle of $\theta_e = 2.69°$ for this advancing droplet is shown in the inset of Fig. 1(d). Note that both the contact angle and the change in the contact angle are small, validating the small angle and $\theta \approx \theta_e$ approximations.

The relaxation time $\tau(\Omega, \theta_e, \eta)$ of 60 droplets was measured at different T_f (between 180–210 °C) for droplets of varying Ω and coexisting with different h_e (between 5–15 ordered monolayers). An exponential decay well describes the droplet relaxation for both advancing and receding contact angles [Fig. 1(d)]. There is negligible contact angle hysteresis ($< 0.1°$) [44]; thus, θ_e does not depend on whether the droplet is advancing or receding.

The relaxation time, however, does depend on whether the droplet is advancing or receding towards θ_e.

Previous studies [32,34–39] predict that, because the dominant mechanism for dissipation is viscous dissipation near the contact line, $\tau \propto \Omega^{1/3}$ [see Eq. (1)]. The data here, however, are not consistent with this scaling (see Fig. S1 in the Supplemental Material [49]). As the essential assumptions related to the contact angle are safely validated (i.e., $\theta \approx \theta_e < 10°$) and the droplet volume stays constant to within 5% as the droplet spreads, the only possible explanation for the deviation from $\tau \propto \Omega^{1/3}$ is that the assumption of contact line dissipation is wrong. If we write a generalized power dissipation as $\mathcal{P}(r,\theta) \propto K r^{\alpha} \theta^{\beta} \dot{r}^2$, then in the limit of near-equilibrium relaxation to a small θ_e, the contact angle dynamics follows an exponential decay with relaxation time (see the Supplemental Material [49])

$$\tau \propto \frac{K}{\gamma} \frac{\Omega^{\alpha/3}}{\theta_e^{(\alpha/3-\beta+2)}}. \tag{2}$$

In the case of purely viscous dissipation at the contact line, $K = \eta$, $\alpha = 1$, and $\beta = -1$, which recovers the contact line relaxation time of Eq. (1), as required. Here, the diblock copolymer is an anisotropic fluid near the substrate: the wetting layer consists of stacked monolayers and the base of the droplet is also ordered. We might then suspect that the base of the droplet could provide a mechanism for a contact area dependent dissipation. In that case $\alpha = 2$ and $\beta = 0$, resulting in $\tau \propto \Omega^{2/3}$. In Fig. 2(a) we plot τ as a function of $\Omega^{2/3}$ for four different values of T_f. Indeed, we find that the data are consistent with a straight line going through the origin.

For an area-dependent dissipation $\mathcal{P}_A \propto K r^2 \dot{r}(t)^2$ and using Eq. (2), the relaxation time is

$$\tau_A = \frac{\kappa}{\gamma} \frac{\Omega^{2/3}}{\theta_e^{8/3}}, \tag{3}$$

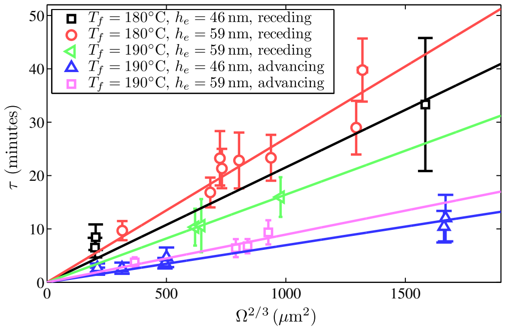

FIG. 2 (color online). The relaxation time τ as a function of $\Omega^{2/3}$ for different values of (T_f, h_e) (with correspondingly different θ_e) as indicated in the legend, for receding and advancing droplet motion. Solid lines are the best fit to a $\tau \propto \Omega^{2/3}$ scaling with zero intercept.

where $\kappa \propto K$. Just as $K = \eta$ for pure viscous dissipation at the contact line, here κ also governs the dynamics. Given $\gamma \approx 31$ mJ/m^2 for the experimental temperatures used [50], and by measuring τ, θ_e, and Ω experimentally, we can obtain κ for each droplet. We find that κ is not a constant, and depends on θ_e as shown in Fig. 3. Furthermore, κ decreases as temperature is increased, and also depends on whether the motion is advancing or receding.

For the diblock copolymer system, the dynamics represented by κ is more complex than η for a simple liquid. The dynamics depends on both the mobility, or friction, of the molecules as well as the degree of segregation of the two blocks within the monolayers. In the limit of an unsegregated wetting layer, the droplet will completely spread ($\theta_e \to 0$) since the wetting layer and droplet would form a homogeneous liquid. As $\theta_e \to 0$, the area-dependent dissipation must also vanish and $\kappa \to 0$ [26]. Conversely, with greater induced order in the monolayers the area-dependent dissipation increases. Since θ_e increases with greater segregation of the wetting layers [44], this means that κ must increase with θ_e. For small θ_e, and to first order, $\kappa \propto \theta_e$, consistent with the linear fits shown as the solid lines in Fig. 3. The molecular mobility at the base of the droplet, while not equivalent to the viscosity due to the presence of order, is still a molecular friction and can be expected to scale with the viscosity, $\kappa \propto \eta(T)$. Thus, we can then write $\kappa = \theta_e \eta / \Lambda$ with Λ a constant with a dimension of length. This gives the area-dependent relaxation time as

$$\tau = \frac{\eta \Omega^{2/3}}{\gamma \theta_e^{5/3} \Lambda}. \tag{4}$$

Our data are consistent with this relationship (Fig. 4). Here, we use $\eta/\gamma = 0.045$ min/μm at 180 °C for PS-P2VP [51], and the Williams-Landel-Ferry scaling of polystyrene [52] to calculate $\eta(T)/\gamma$. To recognize that the droplet relaxation might be different for advancing and receding motion, we allow Λ to differ for advancing Λ_a or receding Λ_r motion.

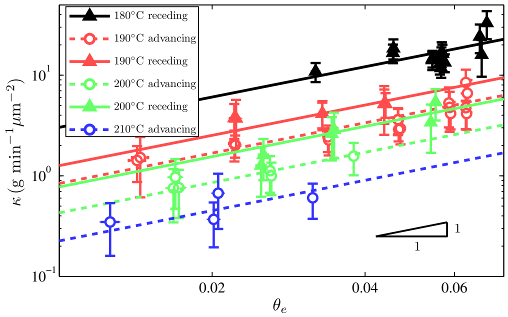

FIG. 3 (color online). The area-dependent relaxation prefactor κ plotted as a function of θ_e (shown on a double logarithmic plot for clarity of the data). κ is not a universal constant for the system, and depends on T as well as θ_e. The lines are fit to $\kappa \propto \theta_e$.

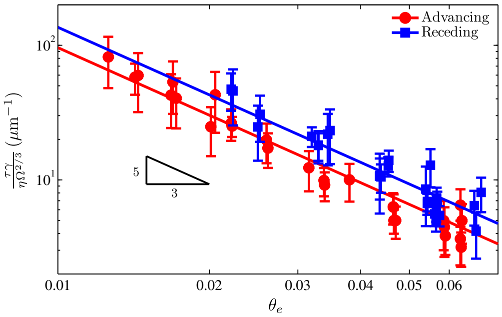

FIG. 4 (color online). The normalized relaxation time as a function of the final contact angle for advancing (circles) and receding (squares) contact line motion. The lines are the best fit of Eq. (4) to the data, with $\Lambda_a = 22 \pm 1$ μm and $\Lambda_r = 16 \pm 1$ μm.

The difference in Λ_a and Λ_r indicates that relaxation is faster for advancing than for receding when comparing droplets with the same Ω and θ_e. This result can be easily understood as follows. In a typical experiment the droplet radius changes by approximately 15%. For a given Ω and θ_e, receding droplets have a greater base area during the course of their evolution, resulting in a stronger power dissipation and slower relaxation times. We note that the ratio $\Lambda_a/\Lambda_r = 1.4$ roughly corresponds to the ratio of the average receding droplet area to the average advancing droplet area given the same volume and final contact angle.

The lack of contact angle pinning in this system has facilitated measurements of the relaxation of a structured liquid droplet in the partial wetting regime. A contact area dependent dissipation describes the data within error using only two adjustable parameters Λ_a and Λ_r. In previous work on the spreading of disordered diblock copolymer droplets in the absence of a prewetted film, a power law consistent with Tanner's law and proportional to $\Omega^{1/3}$ was observed [53]. Thus, a purely viscous dissipation mechanism dominates in the limit of no prewetted film for this system. In contrast, the experimental results show the onset of a secondary dissipation mechanism that is area dependent and originates from the presence of the ordered wetting layer.

The origin of the area-dependent dissipation could be from the onset of a hydrodynamic slip boundary condition at the base of the droplet, i.e., a nonzero horizontal velocity of the fluid at the interface [54]. Interfacial slip has previously been observed in a manifold of different systems, ranging from small molecule liquids, e.g., *n*-alkanes [55], which can have a prewetted layer similar to the system studied here [56], to large molecule liquids like polymers. In particular, slippage of polymeric liquids has been subjected to extensive theoretical and experimental studies (see Ref. [57] and the references therein), including slip at polymer-polymer interfaces in multilayered films [58]. The dissipated power of a slip mechanism due to friction at a fluid interface scales with the contact area between the moving fluid and the substrate, in contrast to viscous dissipation, which predominantly acts in the immediate vicinity of the contact line [24]. In thin polymer films dewetting from hydrophobic substrates, it is precisely the area dependence of the slip mechanism that has been shown to govern the growth dynamics of holes [57,59,60] as well as the appearance of characteristic instabilities of receding liquid fronts [61]. Thus, our observations on the area-dependent droplet relaxation dynamics are consistent with interfacial slip between the (disordered) droplet and the (well-ordered) wetting layer.

The onset of a hydrodynamic slip boundary condition could be the result of the structure of the diblock copolymer molecules near the interface and an anisotropy in their dynamics [62,63]. In a previous molecular dynamics study, the degree of hydrodynamic slip was shown to be related to the microscopic structure induced by the interfaces of a thin fluid film [64]. This idea has also been supported by experimental findings on the interfacial molecular structure of polymeric liquids that exhibit a significant amount of slip [65]. In the case of droplet dynamics, as the droplet spreads its height decreases to conserve volume, and this flow perpendicular to the layers would be hindered by the anisotropy in the dynamics leading to an apparent interfacial slip between successive layers of fluid.

In summary, we have measured the relaxation time of droplets of a structured liquid in the pseudopartial wetting regime as a function of three tunable parameters, droplet volume, equilibrium contact angle, and viscosity, $\tau = \tau(\Omega, \theta_e, \eta)$. For the first time, we are able to vary these parameters on the same sample leading to quantitatively comparable measurements. The diblock copolymer used provides a robust system for the measurement of contact angle dynamics because there is negligible pinning of the contact line ($< 0.1°$). The ideal nature of this system is the direct result of the pseudopartial wetting regime: rather than manually preparing droplets on an ideal surface, the droplets can self-assemble on a metastable wetting layer of the same material. In all 60 experiments we observe that the droplet relaxation scales with the base area of the droplet. This is in direct contrast with the spreading of simple liquids where the energy is dissipated near the contact line of the droplet, and scales with the radius. The area-dependent dissipation can be interpreted as arising from the presence of anisotropic molecular dynamics leading to an apparent interfacial slip.

The authors would like to thank NSERC (Canada) and the German Research Foundation (DFG) under Grant No. BA 3406/2.

---

[*] dalnoki@mcmaster.ca

[1] A. Paterson, M. Robin, M. Fermigier, P. Jenffer, and J. Hulin, J. Pet. Sci. Eng. **20**, 127 (1998).

[2] T. D. Blake, A. Clarke, and K. J. Ruschak, AIChE J. **40**, 229 (1994).
[3] R. A. Hayes and B. J. Feenstra, Nature (London) **425**, 383 (2003).
[4] A. H. Hirsa, C. A. López, M. A. Laytin, M. J. Vogel, and P. H. Steen, Appl. Phys. Lett. **86**, 014106 (2005).
[5] C. Cottin-Bizonne, J.-L. Barrat, L. Bocquet, and E. Charlaix, Nat. Mater. **2**, 237 (2003).
[6] K. Stoev, E. Ramé, and S. Garoff, Phys. Fluids **11**, 3209 (1999).
[7] L. M. Hocking and S. H. Davis, J. Fluid Mech. **467**, 1 (2002).
[8] A.-L. Biance, C. Clanet, and D. Quéré, Phys. Rev. E **69**, 016301 (2004).
[9] A. L. Yarin, Annu. Rev. Fluid Mech. **38**, 159 (2006).
[10] P. M. McGuiggan, D. A. Grave, J. S. Wallace, S. Cheng, A. Prosperetti, and M. O. Robbins, Langmuir **27**, 11966 (2011).
[11] X. Zhang and O. A. Basaran, J. Colloid Interface Sci. **187**, 166 (1997).
[12] A. Prosperetti, Phys. Fluids **24**, 032109 (2012).
[13] S. Ramalingam, D. Ramkrishna, and O. A. Basaran, Phys. Fluids **24**, 082102 (2012).
[14] J. B. Bostwick and P. H. Steen, Phys. Fluids **21**, 032108 (2009).
[15] O. A. Basaran, J. Fluid Mech. **241**, 169 (1992).
[16] J. C. Bird, S. Mandre, and H. A. Stone, Phys. Rev. Lett. **100**, 234501 (2008).
[17] J. B. Bostwick and P. H. Steen, Annu. Rev. Fluid Mech. **47**, 539 (2015).
[18] T. D. Blake, J. Colloid Interface Sci. **299**, 1 (2006).
[19] D. Bonn, J. Eggers, J. Indekeu, J. Meunier, and E. Rolley, Rev. Mod. Phys. **81**, 739 (2009).
[20] P.-G. de Gennes, Rev. Mod. Phys. **57**, 827 (1985).
[21] J. Ralston, M. Popescu, and R. Sedev, Annu. Rev. Mater. Res. **38**, 23 (2008).
[22] J. H. Snoeijer and B. Andreotti, Annu. Rev. Fluid Mech. **45**, 269 (2013).
[23] M. Ramiasa, J. Ralston, R. Fetzer, and R. Sedev, Adv. Colloid Interface Sci. **206**, 275 (2014).
[24] P.-G. de Gennes, F. Brochard-Wyart, and D. Quéré, *Capillarity and Wetting Phenomena: Drops, Bubbles, Pearls, Waves* (Springer, New York, 2004).
[25] L. Tanner, J. Phys. D **12**, 1473 (1979).
[26] S. Cormier, J. McGraw, T. Salez, E. Raphaël, and K. Dalnoki-Veress, Phys. Rev. Lett. **109**, 154501 (2012).
[27] R. Cox, J. Fluid Mech. **168**, 169 (1986).
[28] Y. Suo, K. Stoev, S. Garoff, and E. Ramé, Langmuir **17**, 6988 (2001).
[29] C. Andrieu, D. A. Beysens, V. S. Nikolayev, and Y. Pomeau, J. Fluid Mech. **453**, 427 (2002).
[30] R. Narhe, D. A. Beysens, and V. S. Nikolayev, Langmuir **20**, 1213 (2004).
[31] D. A. Beysens and R. D. Narhe, J. Phys. Chem. B **110**, 22133 (2006).
[32] G. McHale, C. V. Brown, and N. Sampara, Nat. Commun. **4**, 1605 (2013).
[33] F. Rieutord, O. Rayssac, and H. Moriceau, Phys. Rev. E **62**, 6861 (2000).
[34] M. Härth and D. Schubert, Macromol. Chem. Phys. **213**, 654 (2012).
[35] M. D. Ruijter, J. D. Coninck, and G. Oshanin, Langmuir **15**, 2209 (1999).
[36] J. Radulovic, K. Sefiane, and M. E. R. Shanahan, J. Phys. Chem. C **114**, 13620 (2010).
[37] R. Chebbi, J. Adhes. Sci. Technol. **25**, 1767 (2011).
[38] G. McHale, M. I. Newton, and N. J. Shirtcliffe, J. Phys. Condens. Matter **21**, 464122 (2009).
[39] T. Roques-Carmes, V. Mathieu, and A. Gigante, J. Colloid Interface Sci. **344**, 180 (2010).
[40] E. Pérez, E. Schäffer, and U. Steiner, J. Colloid Interface Sci. **234**, 178 (2001).
[41] M. Reyssat and D. Quéré, J. Phys. Chem. B **113**, 3906 (2009).
[42] F. Brochard-Wyart and P.-G. de Gennes, Adv. Colloid Interface Sci. **34**, 561 (1991).
[43] P. Silberzan and L. Leger, Phys. Rev. Lett. **66**, 185 (1991).
[44] M. Ilton, P. Stasiak, M. W. Matsen, and K. Dalnoki-Veress, Phys. Rev. Lett. **112**, 068303 (2014).
[45] L. Du, H. Bodiguel, C. Cottin, and A. Colin, Chemical Engineering and Processing **68**, 3 (2013).
[46] L. Leger and P. Silberzan, J. Phys. Condens. Matter **2**, SA421 (1990).
[47] F. Brochard-Wyart, J. D. Meglio, D. Quéré, and P.-G. de Gennes, Langmuir **7**, 335 (1991).
[48] G. McHale, S. Rowan, and M. Newton, J. Phys. D **27**, 2619 (1994).
[49] See Supplemental Material at http://link.aps.org/supplemental/10.1103/PhysRevLett.115.046103 for a derivation of the contact angle scaling laws.
[50] B. B. Sauer and G. T. Dee, Macromolecules **35**, 7024 (2002).
[51] R. D. Peters and K. Dalnoki-Veress, Eur. Phys. J. E **37**, 100 (2014).
[52] P. Lomellini, Polymer **33**, 4983 (1992).
[53] A. B. Croll and K. Dalnoki-Veress, Eur. Phys. J. E **29**, 239 (2009).
[54] C. L. M. F. Navier, Mem. Acad. Sci. Inst. Fr. **6**, 389 (1823).
[55] J.-H. Cho, B. M. Law, and F. Rieutord, Phys. Rev. Lett. **92**, 166102 (2004).
[56] P. Lazar, H. Schollmeyer, and H. Riegler, Phys. Rev. Lett. **94**, 116101 (2005).
[57] O. Bäumchen and K. Jacobs, J. Phys. Condens. Matter **22**, 033102 (2010).
[58] P. C. Lee, H. E. Park, D. C. Morse, and C. W. Macosko, J. Rheol. **53**, 893 (2009).
[59] C. Redon, J. Brzoska, and F. Brochard-Wyart, Macromolecules **27**, 468 (1994).
[60] R. Fetzer and K. Jacobs, Langmuir **23**, 11617 (2007).
[61] O. Bäumchen, L. Marquant, R. Blossey, A. Münch, B. Wagner, and K. Jacobs, Phys. Rev. Lett. **113**, 014501 (2014).
[62] T. P. Lodge and M. C. Dalvi, Phys. Rev. Lett. **75**, 657 (1995).
[63] A. B. Croll, M. W. Matsen, A.-C. Shi, and K. Dalnoki-Veress, Eur. Phys. J. E **27**, 407 (2008).
[64] P. A. Thompson and M. O. Robbins, Phys. Rev. A **41**, 6830 (1990).
[65] P. Gutfreund, O. Bäumchen, R. Fetzer, D. van der Grinten, M. Maccarini, K. Jacobs, H. Zabel, and M. Wolff, Phys. Rev. E **87**, 012306 (2013).

Transition to Area-Dependent Dissipation in Droplet Spreading (Supplementary Information)

Mark Ilton,[1] Oliver Bäumchen,[2] and Kari Dalnoki-Veress[1, 3, *]
[1]Department of Physics & Astronomy and the Brockhouse Institute for Materials Research,
McMaster University, Hamilton, Ontario, Canada
[2]Max Planck Institute for Dynamics and Self-Organization (MPIDS), 37077 Göttingen, Germany
[3]Laboratoire de Physico-Chimie Théorique, UMR CNRS 7083 Gulliver,
ESPCI ParisTech, PSL Research University, Paris, France

I. DERIVATION OF RELAXATION TIME FOR NEAR EQUILIBRIUM DYNAMICS WITH CONTACT-LINE DISSIPATION

In order to derive the relaxation time of the partially wetting droplets, we employ Frenkel's method [1] in which the dissipated power is equated to the rate of change in energy from the driving force. In this section we will show the derivation of for the case of dissipation solely at the contact line case. We first review some aspects of the spherical cap geometry.

A. Small angle approximation of a spherical cap

The volume Ω of a spherical cap is related to the droplet height h and base radius r by

$$\Omega = \frac{\pi}{6}h(3r^2 + h^2) \tag{1a}$$

$$\Omega \approx \frac{\pi}{2}hr^2 \qquad \text{(small angle approximation).} \tag{1b}$$

The contact angle θ is given by

$$\cos\theta = \frac{r^2 - h^2}{r^2 + h^2} \tag{2a}$$

$$\theta \approx \frac{2h}{r} \qquad \text{(small angle approximation).} \tag{2b}$$

Assuming a constant volume Ω, the relative change of droplet height with radius is given by taking d/dr of Eq. (1a), and using Eq. (2a)

$$\frac{dh}{dr} = \frac{r}{h}(\cos\theta - 1). \tag{3}$$

Using Eq. (1b) and Eq. (2b) with the small angle approximation for $\cos\theta$, gives the droplet contact angle in terms of the radius

$$\theta \approx \frac{4\Omega}{\pi r^3}, \tag{4}$$

and

$$\frac{d\theta}{dr} \approx \frac{-2\theta^{4/3}}{\Omega^{1/3}}. \tag{5}$$

---

[*] Electronic address: `dalnoki@mcmaster.ca`

B. The driving force of partial wetting

Here we consider a droplet of liquid with surface tension γ, initial radius r, height h, and contact angle θ. The droplet is spreading on a wetting layer with an effective interface potential of Φ. We assume that the droplet is much larger than the wetting layer so that the effective interface potential is zero inside that droplet, and the droplet volume Ω is conserved. The droplet, initially not at equilibrium, will spread towards an equilibrium radius r_f, height h_f and contact angle θ_e. The contact angle θ_e can be written as $\Phi = \gamma(\cos\theta_e - 1)$. The excess free energy of the system is

$$\Delta\mathcal{F} = (\Phi + \gamma)\pi(r_f^2 - r^2) + \gamma\pi(r^2 + h^2 - r_f^2 - h_f^2), \tag{6}$$

where the first term is energy difference due to the change in wetting layer area, and the second term results from the difference in the surface area of the droplet. The driving force pushing the contact line at the edge of the droplet towards r_f is

$$F = -\frac{\partial\Delta\mathcal{F}}{\partial r} = (\Phi + \gamma)2\pi r - \gamma 2\pi\left(r + h\frac{dh}{dr}\right). \tag{7}$$

Then using Eq. (3) for dh/dr and $\Phi = \gamma(\cos\theta_e - 1)$ we obtain

$$F = 2\pi r\gamma(\cos\theta_e - \cos\theta) \tag{8a}$$

$$F \approx \pi r\gamma(\theta^2 - \theta_e^2) \qquad \text{(small angle approximation).} \tag{8b}$$

C. Dissipation

In the case of a simple droplet spreading on substrate, the majority of the dissipation in the spreading of a droplet with a small contact angle occurs near the contact line. The viscous dissipative power $\mathcal{P}_v$ scales with the fluid viscosity η as [1]

$$\mathcal{P}_v \propto \eta r\theta^{-1}\left(\frac{dr}{dt}\right)^2. \tag{9}$$

Given the driving force (Eq. (8b)) and power dissipation (Eq. (9)), we can solve for the velocity at the contact line using $\mathcal{P} = F(dr/dt)$, which gives the Hoffman-de Gennes law

$$\frac{dr}{dt} \propto \frac{\gamma}{\eta}\theta(\theta^2 - \theta_e^2). \tag{10}$$

This is consistent with the work of Brochard-Wyart and de Gennes[2]. The two variables r and θ in this differential equation are related through the droplet volume Ω which we take to be a constant. Thus Eq. (10) is an ordinary differential equation in one variable. The two different formulations of the differential equation result in the same characteristic timescale of droplet relaxation for droplets close to their final state, namely $\theta \approx \theta_e$ and $r \approx r_f$. Below we first solve the ODE in terms of the contact angle, and then show that formulating the ODE in terms of the droplet radius gives the same result.

D. ODE in θ

Using Eq. (5) to replace dr/dt with $d\theta/dt$,

$$\frac{d\theta}{dt} \propto \frac{\gamma}{\eta\Omega^{1/3}}\theta^{7/3}\left(\theta_e^2 - \theta^2\right). \tag{11}$$

Letting $x = \theta^2/\theta_e^2$, leads to the differential equation

$$\frac{dx}{dt} \propto \frac{\gamma\theta_e^{10/3}}{\eta\Omega^{1/3}}x^{5/3}\left(1 - x\right). \tag{12}$$

In the limit as $\theta \to \theta_e$, $x \to 1$, the differential equation can be approximated to first order by

$$\frac{dx}{dt} = -\tau^{-1}(1-x), \tag{13}$$

with

$$\tau = \frac{k\eta\Omega^{1/3}}{\gamma\theta_e^{10/3}} \equiv \tau_L. \tag{14}$$

Here k a global constant of proportionality, and the subscript in τ_L refers to the contact-*line* dissipation. This has solutions of an exponential relaxation in x with characteristic timescale τ

$$\frac{1-x}{1-x_i} = \exp\left(\frac{t_i - t}{\tau}\right). \tag{15}$$

When integrated from x_i to x and $t_i = 0$ to t, the solution can be written in terms of θ as

$$\frac{\theta^2 - \theta_e^2}{\theta_i^2 - \theta_e^2} = \exp(-t/\tau). \tag{16}$$

E. ODE in r

We now return to Eq. (10) and write the ODE in terms of r. This will lead to the same differential equation in a reduced variable $x = (r_f/r)^6$, with the same characteristic relaxation time τ as before. Using Eq. (4) to substitute for θ, and Eq. (1b) to substitute for h gives

$$\frac{dr}{dt} \propto \frac{\gamma}{\eta}\frac{\Omega^3}{r^3}\left(r^{-6} - r_f^{-6}\right). \tag{17}$$

Now substituting $x = (r_f/r)^6$ gives

$$\frac{dx}{dt} \propto \frac{\gamma}{\eta}\frac{\Omega^3}{r_f^{10}}\left(1-x\right). \tag{18}$$

In the limit as $r \to r_f$, $x \to 1$, the DE can be approximated by

$$\frac{dx}{dt} = -\tilde{\tau}^{-1}(1-x) \tag{19}$$

where $\tilde{\tau} = (\tilde{k}\eta r_f^{10})/(\gamma\Omega^3)$, and $\tilde{k}$ is a global constant of proportionality. Using the relationships between r and θ from Eq. (1b) and Eq. (2b), we can show that indeed $\tau = \tilde{\tau}$ and the two formulations of the differential equation are equivalent.

II. EXPERIMENTAL RELAXATION MEASUREMENTS

If contact line dependent dissipation was the dominant energy dissipation mechanism, then according to Eq. (14) we would expect $\tau \propto \Omega^{1/3}$. Plotting the experimental relaxation time as a function of $\Omega^{1/3}$ in Fig. S1, shows the data is not consistent with a contact line dissipation. The lines of best fit do not pass through the origin, which suggests an alternate scaling must be used.

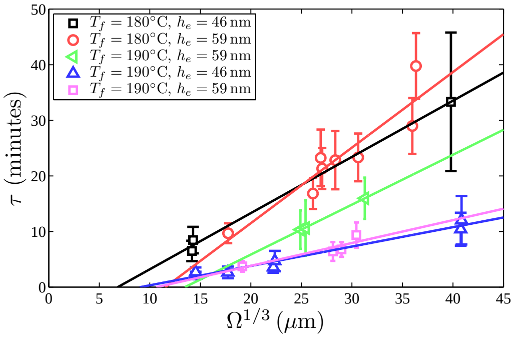

FIG. S1: The experimentally measured relaxation time τ plotted against the cube-root of the droplet volume $\Omega^{1/3}$. The lines are best fit to Eq. (14) with an intercept τ_0. The scaling law does not work for small droplets, which gives rise to a non-zero intercept.

A scaling law of $\tau \propto \Omega^{2/3}$ better describes the data (Fig. S2), which suggests that a different dissipation mechanism might be dominant. Comparing the intercept τ_0 for both an $\Omega^{1/3}$ scaling and an $\Omega^{2/3}$ scaling, the intercept is smaller for the $\Omega^{2/3}$ scaling as shown in Fig. S3. This highlights that the data is indeed consistent with an area-dependent dissipation, and not a contact-line dissipation.

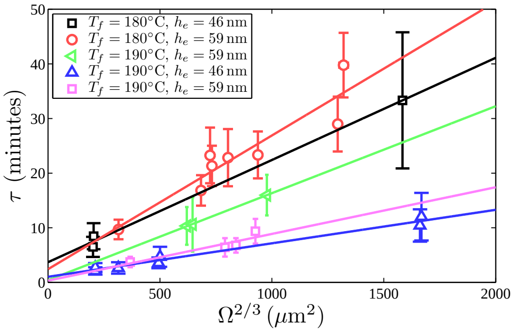

FIG. S2: The relaxation time τ plotted against $\Omega^{2/3}$. The scaling law $\tau \propto \Omega^{2/3}$ better describes the small-droplet relaxation as the intercept more closely passes through the origin.

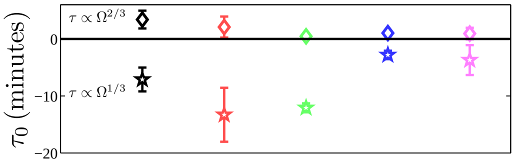

FIG. S3: The intercept τ_0 from fits to the two different scaling laws in Fig. S1 and Fig. S2. The $\Omega^{2/3}$ scaling law fits have significantly smaller intercepts, which show the data is more consistent with an area-dependent dissipation mechanism. The colors used correspond to the legends in Fig. S1 and Fig. S2.

III. GENERAL FORM OF DISSIPATION

Suppose the power dissipation takes a more general form

$$\mathcal{P} \propto K r^{\alpha} \theta^{\beta} \dot{r}(t)^2, \tag{20}$$

then making use of the driving force from Eq. (8b) and solving for the velocity at the contact line using $\mathcal{P} = F\frac{dr}{dt}$ we get a general DE

$$\frac{dr}{dt} \propto \frac{\gamma}{K} r^{(1-\alpha)}\theta^{-\beta}(\theta^2 - \theta_e^2). \tag{21}$$

Casting in terms of only θ

$$\frac{d\theta}{dt} \propto \frac{\gamma}{K\Omega^{\alpha/3}}\theta^{(\alpha/3-\beta+1)}\left(\theta_e^2 - \theta^2\right). \tag{22}$$

Letting $x = \theta^2/\theta_e^2$, leads to the differential equation

$$\frac{dx}{dt} \propto \frac{\gamma\theta_e^{(\alpha/3-\beta+2})}{\eta\Omega^{\alpha/3}} x^{\alpha/6-\beta/2+1}\left(1 - x\right). \tag{23}$$

In the limit as $\theta \to \theta_e$, $x \to 1$, the differential equation can be approximated to first order by

$$\frac{dx}{dt} = -\tau^{-1}(1 - x), \tag{24}$$

with

$$\tau \propto \frac{K\Omega^{\alpha/3}}{\gamma\theta_e^{(\alpha/3-\beta+2)}}. \tag{25}$$

This has solutions of an exponential relaxation in x with characteristic timescale τ

$$\frac{1-x}{1-x_i} = \exp\left(\frac{t_i - t}{\tau}\right). \tag{26}$$

When integrated from x_i to x and $t_i = 0$ to t, the solution can be written in terms of θ as

$$\frac{\theta^2 - \theta_e^2}{\theta_i^2 - \theta_e^2} = \exp(-t/\tau). \tag{27}$$

---

[1] G. McHale, S. Rowan, and M. Newton, J. Phys. D. Appl. Phys. **27**, 2619 (1994).
[2] F. Brochard-Wyart and P. D. Gennes, Adv. Colloid Interface Sci. **39**, 1 (1992).

3.3 Paper III - Capillary levelling of initial conditions with different symmetry

Michael Benzaquen*, Mark Ilton*, Michael V. Massa, Thomas Salez, Paul Fowler, Elie Raphaël, and Kari Dalnoki-Veress "Symmetry plays a key role in the erasing of patterned surface features", Applied Physics Letters, **107**, 053103 (2015).

* shared first authorship

3.3.1 Preface to Paper III

This paper was motivated by the theory work of our collaborators Dr. Michael Benzaquen, Dr. Thomas Salez, and Dr. Elie Raphaël [45]. They showed that any summable initial film thickness profile would converge in finite time to the rescaled Green's function of the linearized supported capillary driven thin film equation. In other words, for any initial perturbation $\delta(x, t = 0)$ to a film with thickness h_0 in which $\int dx\, \delta(x) \neq 0$, the film thickness profile at a later time converges to the same shape. Regardless of the initial shape of the perturbation, the perturbation will relax to the same shape at some intermediate time provided volume was added or removed from the film to create the perturbation. The time has to be long enough for memory of the initial condition to be forgotten, but it still happens in a finite amount of time.

Here we explore what happens at intermediate times for the case where the perturbations add no extra volume to the film. Many lithographic techniques involve creating these type of perturbations, so there is a technological motivation for studying what happens in these types of films. The way we create such "zero-volume" perturbations is by using focused laser spike annealing. Since the laser effectively pushes material out of the way, it conserves the total volume of the initially uniform film.

In the paper, we show that the film thickness profile (in the notation of the paper $\delta(x,t) \to d(x,t)$) can be written as an infinite series $d(x,t) = \sum_{n=0}^{\infty} W_n$. The nth term in the series depends on the nth moment of the initial film thickness profile $W_n \propto \int dx\, x^n d(x,0)$. The nth term in the series is also a power law in time $W_n \propto$

$t^{-(n+1)/4}$. This means that the higher order terms decay more quickly in time. The intermediate behaviour of the film thickness profile is dominated by the first non-zero term in the expansion. For example, in the case of a trench created by Flask, the 0th and 1st order moments are zero $W_0 = W_1 = 0$, and the dynamics are described by the second order term at intermediate time, with the depth of the profile decaying as $t^{-1/2}$.

We experimentally verified this series expansion for the $n = 1$ and $n = 2$ terms ($n = 0$ was published previously [121]). Also a version of this expansion was derived for 3D axisymmetric perturbations. We experimentally show that a non-axisymmetric shape evolves towards the axisymmetric zero-volume attractor in the 3D case.

The results here have important implications for the stability or erasing of an initial perturbation. Just by altering the symmetry or dimensionality of an initial condition, the power law which describes the relaxation of the depth of the feature will change.

In this work I helped Mike Massa revive the Flask setup in our lab, performed the experiments, analyzed the results, wrote a first draft of the manuscript, and was involved in revisions.

APPLIED PHYSICS LETTERS **107**, 053103 (2015)

Symmetry plays a key role in the erasing of patterned surface features

Michael Benzaquen,[1,a)] Mark Ilton,[2,a)] Michael V. Massa,[2] Thomas Salez,[1] Paul Fowler,[2]
Elie Raphaël,[1] and Kari Dalnoki-Veress[2,1,b)]
[1]*Laboratoire de Physico-Chimie Théorique, UMR CNRS Gulliver 7083, ESPCI ParisTech, PSL Research University, 75005 Paris, France*
[2]*Department of Physics and Astronomy, McMaster University, Hamilton, Ontario L8S 4M1, Canada*

(Received 24 April 2015; accepted 17 July 2015; published online 3 August 2015)

We report on how the relaxation of patterns prepared on a thin film can be controlled by manipulating the symmetry of the initial shape. The validity of a lubrication theory for the capillary-driven relaxation of surface profiles is verified by atomic force microscopy measurements, performed on films that were patterned using focused laser spike annealing. In particular, we observe that the shape of the surface profile at late times is entirely determined by the initial symmetry of the perturbation, in agreement with the theory. The results have relevance in the dynamical control of topographic perturbations for nanolithography and high density memory storage.
© *2015 AIP Publishing LLC*. [http://dx.doi.org/10.1063/1.4927599]

Thin polymer films are of general interest, being both industrially relevant and readily amenable to experiment.[1] Used in diverse applications such as data storage, lubricant coatings, electronic devices, and wire arrays, polymer films can be easily tuned in both their wetting properties as well as their dynamics. An area of especially active research involves the use of thin polymer films for nanoscale pattern templating. Block copolymer lithography,[2–6] for instance, has been used to shape samples on sub-10 nm length-scales[7–9] by taking advantage of the self-assembly of amphiphilic polymer molecules. This self assembly can be further controlled by topographic perturbations, for example, those created using graphoepitaxy, grayscale lithography, or 3D printing, on larger mesoscopic length-scales.[10–14] Topographic perturbations can also be used to directly pattern homogeneous thin films, as is the case in nanoimprint lithography,[15–19] and is applicable as a data storage technique with dense memory capabilities,[20,21] in self-cleaning surfaces,[22] and organic optoelectronics.[23,24] The relaxation of thin film perturbations has been used to study glassy polymer dynamics,[25–27] film viscosity,[28–31] and viscoelastic properties.[32–34] Topographic perturbations can be used not only in patterning films for applied technologies but also as a way to study material properties on small length-scales.

Perturbations can be created atop a polymer film on a mesoscopic length-scale in a variety of ways. Unfavourable wetting properties,[35–39] electro-hydrodynamic instability,[40–42] Marangoni flow,[43–46] and thermocapillary forces[47–51] can all drive a flat film away from a uniform film thickness. The film viscosity η, surface tension γ, and unperturbed film thickness h_0 are three parameters that influence the effective mobility of a film, which affects the relaxation of an applied surface perturbation. A dimensionless time-scale $t_0 = 3\eta h_0/\gamma$ can be used to characterize the relaxation of a viscous film.[52] By increasing the temperature or placing the film in solvent vapour, the effective mobility of the film can be increased, causing a faster relaxation of topographic perturbations. Finally, geometry appears to play a key role as well, since a long and straight trench[53] relaxes with a different power-law in time than a cylindrical mound.[54]

In this article, we rationalize a method to control the surface relaxation rate of a thin film, based on the geometrical properties of its initial pattern. First, we present a linear theory of the capillary relaxation of surface profiles. Then, the validity of the asymptotic series expansion of the general solution is experimentally tested using focused laser spike annealing and atomic force microscopy. In agreement with theory, we find that the shape and relaxation rate of surface feature to strongly depend on their initial symmetry. More specifically, within the configurations studied here, we observe that quickly erasable features can be created by patterning an initial perturbation with a high degree of spatial symmetry.

For an annealed film with a vertical thickness profile described by $h(\boldsymbol{r},t) = h_0 + d(\boldsymbol{r},t)$, the surface displacement $d(\boldsymbol{r},t)$ at a given horizontal position $\boldsymbol{r}$ decays in time t due to capillary forces, and the final equilibrium state is a flat film with uniform thickness h_0.

When the system is bidimensional, namely, invariant along one spatial direction, the perturbation is a function of one spatial direction x only, and $\boldsymbol{r}$ is replaced by x. In such a case, one can show within a lubrication model (see supplementary material[55]) that the perturbation is given by the asymptotic series expansion

$$\frac{d(x,t)}{h_0} = \underbrace{\frac{\mathcal{M}_0 F_0(u)}{(t/t_0)^{1/4}}}_{\text{non-zero volume}} - \underbrace{\frac{\mathcal{M}_1 F_1(u)}{(t/t_0)^{1/2}}}_{\substack{\text{zero-volume}\\ \text{asymmetric}}} + \frac{1}{2}\underbrace{\frac{\mathcal{M}_2 F_2(u)}{(t/t_0)^{3/4}}}_{\substack{\text{zero-volume}\\ \text{symmetric}}} - \cdots, \tag{1}$$

where $u = (x/h_0)/(t/t_0)^{1/4}$ is a dimensionless variable. Each term in Eq. (1) has a dimensionless attractor function $F_i(u)$, and two prefactors: the moment $\mathcal{M}_i/(i!)$ and the temporal dependence $(t_0/t)^{(i+1)/4}$. The prefactors are functions of the initial state of the perturbation and the characteristic time-scale t_0. In the first term, $\mathcal{M}_0$ is proportional to the amount

---

[a)] M. Benzaquen and M. Ilton contributed equally to this work.
[b)] Electronic mail: dalnoki@mcmaster.ca

This article is copyrighted as indicated in the article. Reuse of AIP content is subject to the terms at: http://scitation.aip.org/termsconditions. Downloaded to IP: 130.113.111.210 On: Wed, 02 Sep 2015 23:46:22

of excess volume the perturbation adds, or equivalently the 0th moment of the initial profile ($\mathcal{M}_0 \propto \int \mathrm{d}x\, d(x,0)$). For that reason, this term is labelled as "non-zero volume." In the second term, $\mathcal{M}_1$ is non-zero when the profile is asymmetric, and it is proportional to the 1st moment of the initial profile ($\mathcal{M}_1 \propto \int \mathrm{d}x\, x\, d(x,0)$). Because, at long times, this term becomes the leading order term when $\mathcal{M}_0 = 0$ and $\mathcal{M}_1 \neq 0$, it is termed "zero-volume asymmetric." Similarly, the third term is proportional to the 2nd moment of the initial distribution ($\mathcal{M}_2 \propto \int \mathrm{d}x\, x^2\, d(x,0)$). This term becomes dominant when the initial distribution has no excess volume and is perfectly symmetric, namely, $\mathcal{M}_0 = \mathcal{M}_1 = 0$ and $\mathcal{M}_2 \neq 0$ and is thus labelled "zero-volume symmetric." The attractor functions $F_i(u) = F_0^{(i)}(u)$ are the i-th derivatives of $F_0(u)$ and encode the rescaled shape of the spatial profile of the perturbation. Examples of attractor functions are shown in Figures 1(b) and 1(d). Because of the different power-laws in time for each term, after an initial transient regime, the overall relaxation is dominated by the first term with a non-zero prefactor in Eq. (1), regardless of the exact shape of the initial surface feature. In that sense, the attractor functions are referred to as *universal* attractors. If volume is added to the reference flat film by the initial perturbation, $\mathcal{M}_0 \neq 0$, the profile $d(x,\ t)$ will converge to the function $F_0(u)$ in finite time.[33] If no volume is added by the initial perturbation, then the profile will converge to the first term with a non-zero prefactor in Eq. (1).

In the case where the surface displacement is a function of two spatial dimensions in the plane, $\boldsymbol{r} = (x,y) = (r,\psi)$, an angular average on ψ around the center[56] of the perturbation can be taken and the averaged profile, $\langle d(r,\psi,t)\rangle_\psi$, can be written as the following asymptotic series expansion:[55]

$$\frac{\langle d(r,\psi,t)\rangle_\psi}{h_0} = \underbrace{\frac{\mathcal{N}_0 G_0(v)}{(t/t_0)^{1/2}}}_{\text{non-zero volume}} + \underbrace{\frac{1}{2}\frac{\mathcal{N}_2 G_2(v)}{t/t_0}}_{\text{zero-volume}} + \cdots . \qquad (2)$$

Here, $v = (r/h_0)/(t/t_0)^{1/4}$, where r is the radial distance from the center. Each term in the series has a similar structure to that of the 2D case. There are moments $\mathcal{N}_i$ that depend on the symmetry of the initial perturbation, attractor functions $G_i(u)$ that encode the rescaled shape of the spatial profile, and power-laws in time which have larger respective exponents than the 2D case. Higher order terms in the series are zero-volume terms that depend on higher order moments of the initial perturbation.

Previous studies have focused on non-zero volume perturbations and the convergence to 0th order terms in the 2D[33,53,57] and 3D cases.[54] In particular, special attention was dedicated to the convergence time,[33] a first crucial quantity for practical purposes as it is the time-scale after which a surface feature has undergone significant relaxation. Here, we study zero-volume perturbations which are of technological significance, since patterns designed by inducing flow in the material show no volume change from the initially flat film (e.g., through wetting properties, electro-hydrodynamic instabilities, or thermocapillary forces). In that case, the first terms in Eqs. (1) and (2) vanish—$\mathcal{M}_0 = 0$ in the 2D case, and $\mathcal{N}_0 = 0$ in the 3D case—and the relaxation at late times is therefore dominated by the next, lowest, non-zero moment. In contrast with previous investigations on the convergence time,[33] we here focus on the second crucial quantity for practical purposes: the temporal exponent of the relaxation. For zero-volume perturbations with similar convergence times, we show that the higher the symmetry, the larger the exponent, *i.e.,* the faster the erasing.

In order to test the role symmetry plays in surface relaxation, three types of zero-volume perturbations were made (see Figure 1) using focused laser spike annealing[51,58,59] on thin polystyrene films (see supplementary material for further information[55]): (i) a 2D asymmetric feature which maximizes the second term in Eq. (1), as shown in Figures 1(a) and 1(b); (ii) a 2D symmetric feature dominated by the third term in Eq. (1), as shown in Figures 1(c) and 1(d); and (iii) a 3D feature with no apparent symmetry such that only the first term in Eq. (2) is zero, as shown in Figures 1(e) and 1(f). The 2D asymmetric feature was created with large extrema, with a peak-to-peak height of 114 nm. The 2D symmetric feature had an initial amplitude of 361 nm. Finally, the 3D feature was created by making 4 different depressions of varying depths, resulting in a deepest feature with an amplitude of 188 nm, and with three smaller features nearby.

Each sample was annealed above the glass transition temperature ($T_g \approx 100\,^\circ\mathrm{C}$) to probe the surface relaxation.

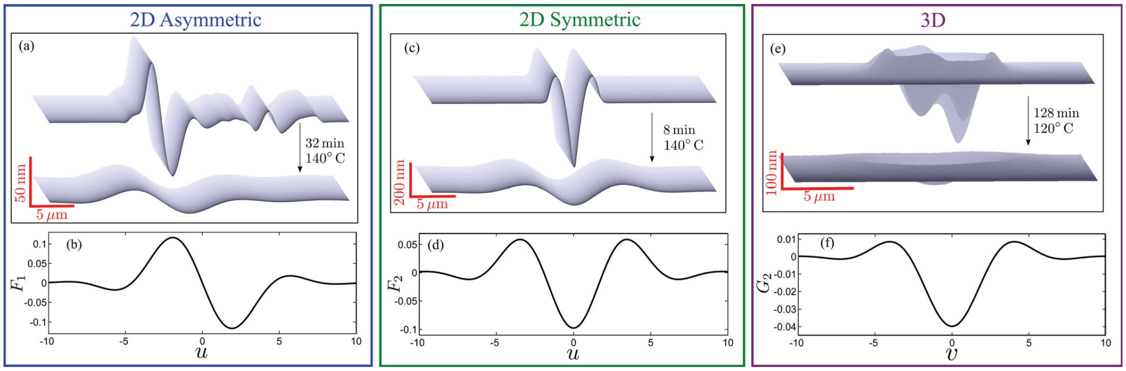

FIG. 1. ((a), (c), and (e)) Experimentally measured AFM profiles of three different zero-volume surface perturbations atop thin polystyrene films, initially and after annealing. ((b), (d), and (f)) Corresponding attractor functions which appear in Eqs. (1) and (2).

This article is copyrighted as indicated in the article. Reuse of AIP content is subject to the terms at: http://scitation.aip.org/termsconditions. Downloaded to IP: 130.113.111.210 On: Wed, 02 Sep 2015 23:46:22

After a certain annealing time, the sample was quenched to room temperature, its height profile measured with atomic force microscopy (AFM), and then it was placed back on the hot stage in order to repeat the annealing-quenching-measure sequence. The 2D features were annealed at 140 °C. Because the 3D dynamics is faster than the 2D case, as stated above, the 3D feature was annealed at 120 °C to slow down its relaxation and ensure that the annealing times were much longer (≥ 1 min) than the time it took to quench the sample (<10 s). Since the films are rapidly quenched deep into the glassy state between annealing steps, flow only occurred during the time the samples were annealed above T_g.

To explicitly test the convergence of the 2D surface profiles to the corresponding attractor functions $F_i(u)$, the normalized profiles are plotted in Figure 2 as a function of the rescaled position u for several times t. Figure 2(a) shows the normalized relaxation profile of the 2D asymmetric feature from Figure 1(a), that is, with $\mathcal{M}_0 = 0$ and $\mathcal{M}_1 \neq 0$. The profiles collapse onto the normalized attractor $F_1/F_{1\max}$, which corresponds to the lowest-order non-zero term from Eq. (1). Similarly, Figure 2(b) shows the normalized relaxation profile of the 2D symmetric feature from Figure 1(c), that is, with $\mathcal{M}_0 = \mathcal{M}_1 = 0$ and $\mathcal{M}_2 \neq 0$. In this case, the data collapse to the normalized attractor $F_2/F_2(0)$.

For the 3D feature shown in Figure 1(e), that is, with $\mathcal{N}_0 = 0$, the normalized profiles are shown from above in Figure 3(a) along with the normalized attractor $G_2(v)$. The feature starts off with a low degree of symmetry, evolving towards a roughly axisymmetric depression. The radially averaged profiles are shown in Figure 3(b), with $v = 0$ taken to be the deepest point of the surface perturbation. As predicted by Eq. (2), there is a collapse of the profiles to $G_2(v)$ at late times.

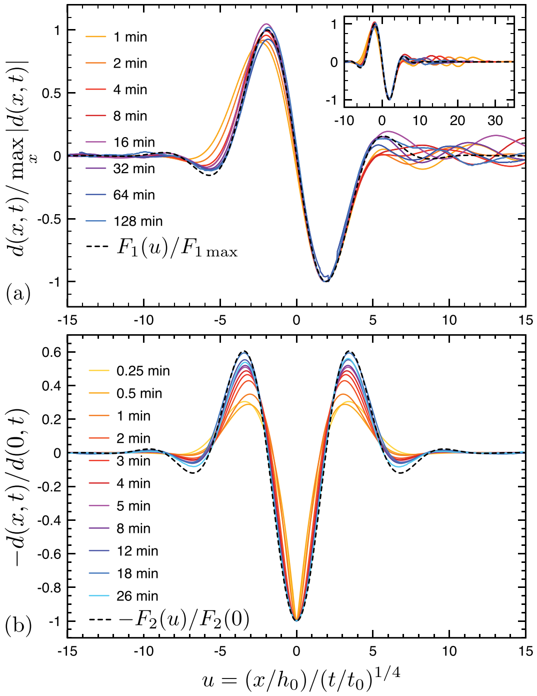

FIG. 2. Normalized profiles of 2D features for both the (a) asymmetric and (b) symmetric initial perturbations, as a function of the rescaled horizontal position $u = (x/x_0)/(t/t_0)^{1/4}$, for different times t that the feature was annealed at 140° C. The black dashed lines correspond to the normalized attractor functions in 2D (see Eq. (1), Figs. 1(b) and 1(d)). The inset shows that the oscillations on the right hand side have a finite spatial extent.

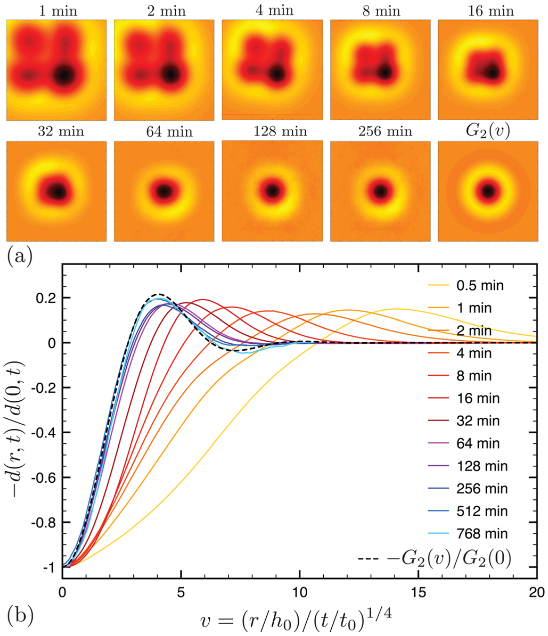

FIG. 3. (a) AFM images showing the temporal evolution of the 3D perturbation viewed from above (see Figure 1(e)), shown in normalized horizontal units, $(x/h_0)/(t/t_0)^{1/4}$ and $(y/h_0)/(t/t_0)^{1/4}$, and color-scaled by the amplitude of the feature: the darker the deeper. The corresponding 3D attractor (see Eq. (2) and Figure 1(f)) is shown in the last panel. (b) Angularly averaged profiles of the normalized AFM images above plotted as a function of the rescaled radius v and compared to the attractor.

So far, we have shown that depending on the initial symmetry of a surface perturbation, Eq. (1) or Eq. (2) describes well the *shape* of the relaxing profile. Now, we focus on the temporal evolution of the *amplitude* of such perturbations. We show that the initial symmetry plays a key role in the relaxation rate. According to Eqs. (1) and (2), the maximum amplitude $d_{\max} = \max(|d|)$ of the perturbation should scale as a power-law in time t for sufficiently long times. The power-law exponent should depend on which order/term controls the relaxation. For example, for the 2D asymmetric feature, the $F_1(u)$ term is dominant which means Eq. (1) predicts $d_{\max} \sim t^{-1/2}$ at late times. Since η and h_0 are obvious factors controlling the dynamics of the film, they have been scaled out using a normalized time. Here, we use the convergence time t_c, which was previously defined[33] as the time when the asymptotic power-law behavior for the amplitude equals the initial amplitude of the perturbation. Convergence times can been computed theoretically for the three present configurations using a similar definition,[55] and the experimentally determined convergence times are given in Fig. 4. The normalized amplitude $d_{\max}(t)/d_{\max}(0)$ is thus plotted against the normalized time t/t_c in Fig. 4. The late-time relaxation of each of the three data sets agrees well with the

This article is copyrighted as indicated in the article. Reuse of AIP content is subject to the terms at: http://scitation.aip.org/termsconditions. Downloaded to IP: 130.113.111.210 On: Wed, 02 Sep 2015 23:46:22

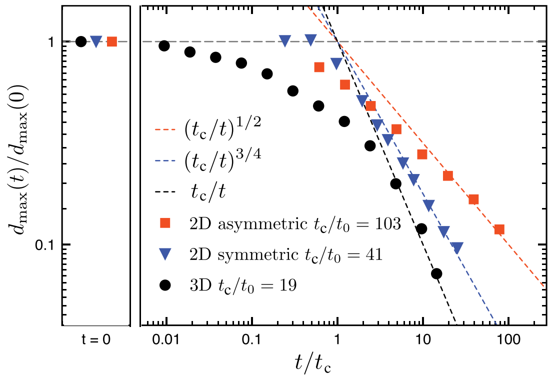

FIG. 4. Double logarithmic plot of the normalized amplitude $d_{\max}/d_{\max}(0)$ of the three different zero-volume surface perturbations, as a function of time t normalized by the convergence time t_c (solid points). The left panel shows the normalized amplitudes at $t = 0$. The dashed lines are the corresponding power-laws predicted by Eqs. (1) and (2).

theoretical power-law predictions from Eqs. (1) and (2). The 3D feature has the steepest relaxation, followed by the 2D symmetric feature, and finally the 2D asymmetric feature. Note that, in the current work, we observe t_c/t_0 to be smaller for patterns described by a steeper power-law (Fig. 4, legend), but, in general, this is not the case for an arbitrary initial profile shape. There are in fact two independent key control parameters: the convergence time and the time exponent.

To sum up, the relaxation of zero-volume perturbations on a flat thin film agrees well with linear lubrication theory. Perturbations with lower symmetry and dimensionality were observed to have the slowest evolution, while perturbations with higher symmetry and dimensionality relaxed more quickly. This has clear implications for the use of topographic perturbations in an applied context. At fixed temperature (or viscosity) and film thickness, if the goal is to create a liquid perturbation stabilized against flow, one should aim to have the lowest possible symmetry and dimensionality. On the other hand, if a quickly erasable perturbation is desirable, the use of higher symmetry and higher dimensionality (3D, rather than 2D feature) would give a faster relaxation. Reliably creating 3D perturbations with a large fourth-order moment, but with zero lower-order moments, is technically challenging but would allow for fast erasing processes. Such strategies, and properly shaped nanoindentors and masks, would speed up—and thus improve—nanomechanical memory storage.[20,21]

In conclusion, we have used focused laser spike annealing to create zero-volume surface perturbations in thin polystyrene films. The relaxation of the initial profiles was measured as a function of time, as the film was driven by surface tension towards the equilibrium state of a flat film. The surface profiles collapse to predicted attractor functions in both 2D and 3D. The amplitudes of the features follow a power-law relaxation in time, the exponent of which is determined by the lowest moment of the initial profile. We have discovered a strategy for tuning the stability and relaxation capabilities of patterned features at the nanoscale. The dimensionality and initial symmetry play a crucial role in the relaxation time-scale of a thin film perturbation. A stable liquid feature is created by adding—or removing—material on an initially flat film and by choosing a 2D initial profile shape with a large convergence time. A quickly erasable feature needs to be patterned in 3D with a short convergence time, and a high degree of symmetry.

Financial Support for this work was provided in part by NSERC (Canada). The authors thank Mark Ediger for an interesting discussion on this topic.

[1] *Polymer Thin Films*, edited by O. K. C. Tsui and T. P. Russell (World Scientific, 2008).
[2] A. Nunns, J. Gwyther, and I. Manners, Polymer (Guildford) **54**, 1269–1284 (2013).
[3] D. A. Boyd, *New Future Developments Catalysis*, edited by S. L. Suib (Elsevier, 2013), pp. 305–332.
[4] Y.-C. Tseng and S. B. Darling, Polymers (Basel) **2**, 470–489 (2010).
[5] A. P. Marencic and R. A. Register, Annu. Rev. Chem. Biomol. Eng. **1**, 277–297 (2010).
[6] I. Hamley, Prog. Polym. Sci. **34**, 1161–1210 (2009).
[7] S.-M. Park, O.-H. Park, J. Y. Cheng, C. T. Rettner, and H.-C. Kim, Nanotechnology **19**, 455304 (2008).
[8] J. G. Son, J.-B. Chang, K. K. Berggren, and C. A. Ross, Nano Lett. **11**, 5079–5084 (2011).
[9] C. M. Bates, T. Seshimo, M. J. Maher, W. J. Durand, J. D. Cushen, L. M. Dean, G. Blachut, C. J. Ellison, and C. G. Willson, Science **338**, 775–779 (2012).
[10] J. Y. Cheng, A. M. Mayes, and C. A. Ross, Nat. Mater. **3**, 823–828 (2004).
[11] J. Y. Cheng, C. A. Ross, H. I. Smith, and E. L. Thomas, Adv. Mater. **18**, 2505–2521 (2006).
[12] I. Bita, J. K. W. Yang, Y. S. Jung, C. A. Ross, E. L. Thomas, and K. K. Berggren, Science **321**, 939–943 (2008).
[13] W. Man, M. Megens, P. J. Steinhardt, and P. M. Chaikin, Nature **436**, 993–996 (2005).
[14] C. Sun, N. Fang, D. M. Wu, and X. Zhang, Sens. Actuators, A Phys. **121**, 113–120 (2005).
[15] S. Y. Chou, P. R. Krauss, and P. J. Renstrom, Appl. Phys. Lett. **67**, 3114 (1995).
[16] S. Y. Chou, P. R. Krauss, and P. J. Renstrom, Science **272**, 85–87 (1996).
[17] M. D. Austin and S. Y. Chou, Appl. Phys. Lett. **81**, 4431 (2002).
[18] L. J. Guo, J. Phys. D: Appl. Phys. **37**, R123–R141 (2004).
[19] L. Guo, Adv. Mater. **19**, 495–513 (2007).
[20] P. Vettiger, G. Cross, U. Drechsler, U. Durig, B. Gotsmann, W. Haberle, M. Lantz, H. Rothuizen, R. Stutz, and G. Binnig, IEEE Trans. Nanotechnol. **1**, 39–55 (2002).
[21] H. Pozidis and P. Bachtold, in *Proceedings of the 2006 IEEE Conference on Emerging Technology* (IEEE, 2006), pp. 39–44.
[22] G. D. Bixler and B. Bhushan, Adv. Funct. Mater. **23**, 4507–4528 (2013).
[23] J. B. Kim, P. Kim, N. C. Pégard, S. J. Oh, C. R. Kagan, J. W. Fleischer, H. A. Stone, and Y.-L. Loo, Nat. Photonics **6**, 327–332 (2012).
[24] A. Bay, N. André, M. Sarrazin, A. Belarouci, V. Aimez, L. A. Francis, and J. P. Vigneron, Opt. Express **21**(1), A179–A189 (2013).
[25] Z. Fakhraai and J. A. Forrest, Science **319**, 600–604 (2008).
[26] Z. Yang, Y. Fujii, F. K. Lee, C.-H. Lam, and O. K. C. Tsui, Science **328**, 1676–1679 (2010).
[27] Y. Chai, T. Salez, J. D. McGraw, M. Benzaquen, K. Dalnoki-Veress, E. Raphaël, and J. A. Forrest, Science **343**, 994–999 (2014).
[28] T. Leveder, S. Landis, and L. Davoust, Appl. Phys. Lett. **92**, 013107 (2008).
[29] T. Leveder, E. Rognin, S. Landis, and L. Davoust, Microelectron. Eng. **88**, 1867–1870 (2011).
[30] E. Rognin, S. Landis, and L. Davoust, Phys. Rev. E **84**, 041805 (2011).
[31] J. D. McGraw, T. Salez, O. Bäumchen, E. Raphaël, and K. Dalnoki-Veress, Phys. Rev. Lett. **109**, 128303 (2012).
[32] E. Rognin, S. Landis, and L. Davoust, J. Vac. Sci. Technol., B Microelectron. Nanom. Struct. **30**, 011602 (2012).
[33] M. Benzaquen, P. Fowler, L. Jubin, T. Salez, K. Dalnoki-Veress, and E. Raphaël, Soft Matter **10**, 8608–8614 (2014).
[34] E. Rognin, S. Landis, and L. Davoust, Langmuir **30**, 6963–6969 (2014).
[35] D. J. Srolovitz and S. A. Safran, J. Appl. Phys. **60**, 255–260 (1986).

This article is copyrighted as indicated in the article. Reuse of AIP content is subject to the terms at: http://scitation.aip.org/termsconditions. Downloaded to IP: 130.113.111.210 On: Wed, 02 Sep 2015 23:46:22

[36] F. Wyart and J. Daillant, Can. J. Phys. **68**, 1084–1088 (1990).

[37] R. Seemann, S. Herminghaus, and K. Jacobs, Phys. Rev. Lett. **87**, 196101 (2001).

[38] G. Reiter, M. Hamieh, P. Damman, S. Sclavons, S. Gabriele, T. Vilmin, and E. Raphaël, Nat. Mater. **4**, 754–758 (2005).

[39] X.-C. Chen, H.-M. Li, F. Fang, Y.-W. Wu, M. Wang, G.-B. Ma, Y.-Q. Ma, D.-J. Shu, and R.-W. Peng, Adv. Mater. **24**, 2637–2641 (2012).

[40] E. Schaffer, T. Thurn-Albrecht, T. Russell, and U. Steiner, Nature **403**, 874–877 (2000).

[41] M. D. Morariu, N. E. Voicu, E. Schäffer, Z. Lin, T. P. Russell, and U. Steiner, Nat. Mater. **2**, 48–52 (2003).

[42] N. Voicu, S. Harkema, and U. Steiner, Adv. Funct. Mater. **16**, 926–934 (2006).

[43] C. B. Kim, D. W. Janes, D. L. McGuffin, and C. J. Ellison, J. Polym. Sci. Part B: Polym. Phys. **52**, 1195–1202 (2014).

[44] J. M. Katzenstein, C. B. Kim, N. A. Prisco, R. Katsumata, Z. Li, D. W. Janes, G. Blachut, and C. J. Ellison, Macromolecules **47**, 6804–6812 (2014).

[45] T. A. Arshad, C. B. Kim, N. A. Prisco, J. M. Katzenstein, D. W. Janes, R. T. Bonnecaze, and C. J. Ellison, Soft Matter **10**, 8043–8050 (2014).

[46] J. M. Katzenstein, D. W. Janes, J. D. Cushen, N. B. Hira, D. L. McGuffin, N. A. Prisco, and C. J. Ellison, ACS Macro Lett. **1**, 1150–1154 (2012).

[47] F. Brochard, Langmuir **5**, 432–438 (1989).

[48] D. Kataoka and S. Troian, Nature **402**, 794–797 (1999).

[49] J. P. Valentino, S. M. Troian, and S. Wagner, Appl. Phys. Lett. **86**, 184101 (2005).

[50] M. Dietzel and S. Troian, Phys. Rev. Lett. **103**, 074501 (2009).

[51] J. P. Singer, P.-T. Lin, S. E. Kooi, L. C. Kimerling, J. Michel, and E. L. Thomas, Adv. Mater. **25**, 6100–6105 (2013).

[52] T. Salez, J. D. McGraw, S. L. Cormier, O. Bäumchen, K. Dalnoki-Veress, and E. Raphaël, Eur. Phys. J. E **35**, 114 (2012).

[53] O. Bäumchen, M. Benzaquen, T. Salez, J. D. McGraw, M. Backholm, P. Fowler, E. Raphaël, and K. Dalnoki-Veress, Phys. Rev. E **88**, 035001 (2013).

[54] M. Backholm, M. Benzaquen, T. Salez, E. Raphaël, and K. Dalnoki-Veress, Soft Matter **10**, 2550–2558 (2014).

[55] See supplementary material at http://dx.doi.org/10.1063/1.4927599 for details of the theoretical and experimental methods.

[56] In the general case, although the center of the surface perturbation is not uniquely defined, the results are independent of the choice of the center. For most real experimental features, the position of the center can be chosen quite naturally.

[57] M. Benzaquen, T. Salez, and E. Raphaël, Eur. Phys. J. E. **36**, 82 (2013).

[58] J. M. Hudson, M.A.Sc. thesis, McMaster University, 2004. http://hdl.handle.net/11375/16668.

[59] J. Parete, M.A.Sc. thesis, McMaster University, 2008. See http://hdl.handle.net/11375/16667.

This article is copyrighted as indicated in the article. Reuse of AIP content is subject to the terms at: http://scitation.aip.org/termsconditions. Downloaded to IP: 130.113.111.210 On: Wed, 02 Sep 2015 23:46:22

Supplementary information to "Symmetry Plays a Key Role in the Erasing of Patterned Surface Features"

Michael Benzaquen,[1, a)] Mark Ilton,[2, a)] Michael V. Massa,[2] Thomas Salez,[1] Paul Fowler,[2] Elie Raphaël,[1] and Kari Dalnoki-Veress[2, 1, b)]

1)*Laboratoire de Physico-Chimie Théorique, UMR CNRS Gulliver 7083,*
ESPCI ParisTech, PSL Research University, 75005 Paris,
France

2)*Department of Physics & Astronomy, McMaster University, Hamilton, Ontario,*
Canada, L8S 4M1

---

a)These authors contributed equally to this work.

b)Electronic mail: dalnoki@mcmaster.ca

I. Experimental Methods

Thin polystyrene films, with molecular weight $M_w = 31.8$ kg/mol and polydispersity index 1.06 (Polymer Source), were spincast from dilute toluene solution (Fisher Scientific, Optima grade) onto silicon wafers (University Wafer). The films were pre-annealed for 2 hours at 150° C on a hot stage (Linkham Scientific Instruments) to relax the polymer chains. Zero-volume surface perturbations were created using a home-built focused laser spike annealing setup similar to that described previously[1–3]. Briefly, a focused laser (Coherent, Verdi V2, 532 nm) is rastered across the thin polymer film at room temperature. The silicon substrate absorbs some of the laser energy which creates a large temperature gradient. This locally heats the polymer film above its glass transition ($\sim$ 100 °C). Since the surface tension decreases with increasing temperature, there is a surface tension gradient that drives flow away from the region of higher temperature, thus creating a perturbation in the film without any resulting change in volume. Both 2D and 3D depressions can be created using this method. A 2D feature is created by holding the laser at a constant power and moving it over the surface at constant speed in a long (200 μm) straight motion, creating a nearly-uniform height profile in the direction y parallel to the laser motion. The 2D asymmetric feature was created using multiple passes of the laser with progressively lower power and a small horizontal shift along x between passes. As a line is rastered with the laser, material gets pushed to either side of the line. Because there are multiple passes of the laser, there is an imperfect clearance of the material resulting in small oscillations to the right ($x > 0$). These are all less than $\sim$ 20% of the main feature height (see inset of Figure 2(a)), and become less important after annealing. On the other hand, the 2D symmetric feature was created using a single pass of the laser, and no oscillation was present due to the single pass of the laser. Finally, a 3D depression is created by opening the laser shutter at a fixed point for a brief amount of time ($\approx$ 1 s). Atomic force microscopy (AFM, Veeco, Caliber) was used to measure the surface profiles of the films and was performed after a quench at room temperature.

II. Theoretical Methods

The theory is based on the lubrication approximation and the thin film equation[4]:

$$\partial_t h + \frac{\gamma}{3\eta}\,\boldsymbol{\nabla}\cdot\left(h^3\,\boldsymbol{\nabla}\Delta h\right) = 0\ , \tag{S1}$$

which describes the capillary-driven relaxation of a thin supported film with vertical thickness profile $h(\boldsymbol{r},t)$, along horizontal space $\boldsymbol{r}$ and time t. Equation (S1) can be nondimensionalized through $h = h_0 + d(\boldsymbol{r},t) = H\,h_0$, $\boldsymbol{r} = \boldsymbol{R}\,h_0$ and $t = T\,t_0$, where $t_0 = 3\eta h_0/\gamma$, and where h_0 is the reference height at infinity. Equation (S1) is highly nonlinear and, as of today, hasn't been solved analytically. When the surface of the film is only slightly perturbed, meaning that the surface displacement d is small compared to the reference height h_0, the capillary-driven thin film equation can be linearized[5,6] by letting $H(\boldsymbol{R},T) = 1 + \mathcal{Z}(\boldsymbol{R},T)$, with $|\mathcal{Z}(\boldsymbol{R},T)| \ll 1$, where $\mathcal{Z} = d/h_0$ denotes the dimensionless surface displacement. This yields, at the lowest order in $\mathcal{Z}$, the dimensionless linear thin film equation:

$$\left(\partial_T + \Delta^2\right)\mathcal{Z}(\boldsymbol{R},T) = 0\ , \tag{S2}$$

where Δ^2 denotes the bilaplacian operator. Equation (S2) can be solved by deriving its Green's function $\mathcal{G}(\boldsymbol{R},T)$. Proceeding as in a previous communication[6] yields $\mathcal{G}(\boldsymbol{R},T) = \breve{\mathcal{G}}(\boldsymbol{U},T)$ with for all $T > 0$:

$$\breve{\mathcal{G}}(\boldsymbol{U},T) = \frac{1}{T^{(d-1)/4}}\ \phi(\boldsymbol{U})\ , \tag{S3}$$

where the function ϕ depends only on the dimensionality of the system $d \in \{2,3\}$:

$$\phi(\boldsymbol{U}) = \frac{1}{(2\pi)^{(d-1)}}\int \mathrm{d}^{(d-1)}\boldsymbol{Q}\ e^{-\left(\boldsymbol{Q}^2\right)^2}e^{i\boldsymbol{Q}\cdot\boldsymbol{U}}\ , \tag{S4}$$

and where we introduced the self-similar variable $\boldsymbol{U} = \boldsymbol{R}T^{-1/4}$. Note that the function ϕ can be written in terms of hypergeometric functions[5–8]. The solution to any summable initial perturbation $\mathcal{Z}(\boldsymbol{R},0) = \mathcal{Z}_0(\boldsymbol{R})$ is simply given by the convolution $(\mathcal{G} * \mathcal{Z}_0)(\boldsymbol{R},T)$. Assuming that the initial perturbation is *rapidly decreasing* in space, namely for all $n \in \mathbb{N}$, $\lim_{|\boldsymbol{R}|\to\infty} |\boldsymbol{R}|^n \mathcal{Z}_0(\boldsymbol{R}) = 0$, allows for writing the solution as a series in which the different terms naturally decrease with time, and where remarkably: the higher the order, the faster the decrease. Defining respectively the algebraic volume, $\mathcal{M}_0$, the first and second moments,

$\boldsymbol{\mathcal{M}}_1$ and $\mathfrak{M}_2$, of the initial perturbation $\mathcal{Z}_0(\boldsymbol{R})$, as well as the Hessian matrix $\mathcal{H}_\phi(\boldsymbol{U})$ of the function $\phi(\boldsymbol{U})$, yields $\mathcal{Z}(\boldsymbol{R},T) = \breve{\mathcal{Z}}(\boldsymbol{U},T)$ with:

$$\breve{\mathcal{Z}}(\boldsymbol{U},T) = \frac{1}{T^{(d-1)/4}}\left[\mathcal{M}_0\,\phi(\boldsymbol{U}) - \frac{\boldsymbol{\mathcal{M}}_1\cdot\boldsymbol{\nabla}\phi(\boldsymbol{U})}{T^{1/4}} + \frac{1}{2}\frac{\mathfrak{M}_2 : \mathcal{H}_\phi(\boldsymbol{U})}{T^{1/2}} + \mathrm{O}\left(\frac{1}{T^{3/4}}\right)\right]\ , \tag{S5}$$

where $\mathfrak{A} : \mathfrak{B} = \sum_{ij}\mathfrak{A}_{ij}\mathfrak{B}_{ij}$ is the tensor contraction of $\mathfrak{A}$ and $\mathfrak{B}$. In the 2D case, $d = 2$, where the profile depends on only one spatial variable, Eq. (S5) simply becomes:

$$\breve{\mathcal{Z}}(U,T) = \frac{1}{T^{1/4}}\left[\mathcal{M}_0\,\phi^{\mathrm{2D}}(U) - \frac{\mathcal{M}_1\,\phi^{\mathrm{2D}\prime}(U)}{T^{1/4}} + \frac{1}{2}\frac{\mathcal{M}_2\,\phi^{\mathrm{2D}\prime\prime}(U)}{T^{1/2}} + \mathrm{O}\left(\frac{1}{T^{3/4}}\right)\right]\ . \tag{S6}$$

where $\mathcal{M}_n = \int \mathrm{d}X'\,X'^n\mathcal{Z}_0(X')$. In the 3D case, the first moments of the initial perturbation $\mathcal{Z}_0(\boldsymbol{R})$ read:

$$\mathcal{M}_0 = \int \mathrm{d}^2\boldsymbol{R}\,\mathcal{Z}_0(\boldsymbol{R}) \tag{S7a}$$

$$\boldsymbol{\mathcal{M}}_1 = \int \mathrm{d}^2\boldsymbol{R}\,\boldsymbol{R}\,\mathcal{Z}_0(\boldsymbol{R}) \tag{S7b}$$

$$\mathfrak{M}_2 = \begin{pmatrix} \int \mathrm{d}X\,\mathrm{d}Y\,X^2\mathcal{Z}_0(X,Y) & \int \mathrm{d}X\,\mathrm{d}Y\,XY\mathcal{Z}_0(X,Y) \\ \int \mathrm{d}X\,\mathrm{d}Y\,XY\mathcal{Z}_0(X,Y) & \int \mathrm{d}X\,\mathrm{d}Y\,Y^2\mathcal{Z}_0(X,Y) \end{pmatrix}\ . \tag{S7c}$$

Letting the polar change of variables $\boldsymbol{U} = U_R(\cos\psi, \sin\psi)$, together with Eqs. (S7) yields:

$$\boldsymbol{\mathcal{M}}_1\cdot\boldsymbol{\nabla}\phi^{\mathrm{3D}} = \int \mathrm{d}R'\mathrm{d}\alpha\,R'^2\cos(\alpha-\psi)\,\mathcal{Z}_0(R',\alpha)\phi^{\mathrm{3D}\prime}(U_R) \tag{S8a}$$

$$\mathfrak{M}_2 : \mathcal{H}_{\phi^{\mathrm{2D}}} = \int \mathrm{d}R'\mathrm{d}\alpha\,R'^3\mathcal{Z}_0(R',\alpha)\left[\cos^2(\alpha-\psi)\phi^{\mathrm{3D}\prime\prime}(U_R) + \sin^2(\alpha-\psi)\frac{\phi^{\mathrm{3D}\prime}(U_R)}{U_R}\right] . \tag{S8b}$$

Considering the averaged profiles over the angle ψ yields $\langle\boldsymbol{\mathcal{M}}_1\cdot\boldsymbol{\nabla}\phi^{\mathrm{3D}}\rangle_\psi = 0$ and:

$$\langle\mathfrak{M}_2 : \mathcal{H}_\phi^{\mathrm{3D}}\rangle_\psi = \frac{1}{2}\int \mathrm{d}R'\,R'^3\mathcal{Z}_0(R')\left[\phi^{\mathrm{3D}\prime\prime}(U_R) + \frac{\phi^{\mathrm{3D}\prime}(U_R)}{U_R}\right]\ . \tag{S9}$$

Note as well that, if the initial profile is axisymmetric, namely $\mathcal{Z}_0(R,\alpha) = \mathcal{Z}_0(R)$ then one has $\boldsymbol{\mathcal{M}}_1\cdot\boldsymbol{\nabla}\phi^{\mathrm{3D}} = 0$, and $\mathfrak{M}_2 : \mathcal{H}_{\phi^{\mathrm{3D}}} = \langle\mathfrak{M}_2 : \mathcal{H}_\phi^{\mathrm{2D}}\rangle_\psi$ as given by Eq. (S9).

In the manuscript, Eq. (1) is none other than Eq. (S6) where we have let $F_n(u) = \phi^{\mathrm{2D}(n)}(u)$, and Eq. (2) is the angular average of Eq. (S5), where $G_0(v) = \phi^{\mathrm{3D}}(v)$, $G_2(v) = \phi^{\mathrm{3D}\prime\prime}(v) + \phi^{\mathrm{3D}\prime}(v)/v$, $\mathcal{N}_0 = \mathcal{M}_0$ as given by Eq. (S7a), and $\mathcal{N}_2 = \int \mathrm{d}R'\,R'^3\mathcal{Z}_0(R')$, consistent with Eq. (S9).

As mentioned in the article, the convergence time can be computed analytically using the scheme proposed previously[7] for the particular case of non-zero volume surface perturbations. Briefly, denoting by $\mathcal{Z}_\infty(\boldsymbol{R}, T)$ the dimensionless surface displacement in the long-term asymptotic regime, the dimensionless convergence time is determined by its intersection with the initial amplitude. Choosing the maximum amplitude over space as a reference value yields: $\max_X |\mathcal{Z}_\infty(X, T_\mathrm{c})| = |\mathcal{Z}_0|_{\max}$. For the three-dimensional case, the method is naturally applied to the angularly averaged profiles. Using Eqs. (S5), (S6) and (S9) in the three particular cases relevant to the experiments presented in this article, one obtains:

$$\text{2D asymmetric:} \qquad T_\mathrm{c} = \left(\frac{\mathcal{M}_1 {\phi^{2\mathrm{D}\prime}}_{\max}}{\mathcal{Z}_{0\,\max}}\right)^2 \tag{S10a}$$

$$\text{2D symmetric:} \qquad T_\mathrm{c} = \left|\frac{\mathcal{M}_2 \phi^{2\mathrm{D}\prime\prime}(0)}{2\mathcal{Z}_0(0)}\right|^{4/3} \tag{S10b}$$

$$\text{3D:} \qquad T_\mathrm{c} = \left|\frac{\mathcal{N}_2}{16\pi \mathcal{Z}_0(0)}\right| . \tag{S10c}$$

References

[1] J. M. Hudson, *Laser lithography of thin polymer films*, Thesis (m.a.sc.), McMaster University (2004).

[2] J. Parete, *Laser lithography of diblock copolymer films*, Thesis (m.a.sc.), McMaster University (2008).

[3] J. P. Singer, P.-T. Lin, S. E. Kooi, L. C. Kimerling, J. Michel, and E. L. Thomas, Adv. Mater. **25**, 6100 (2013).

[4] R. Blossey, *Thin Liquid Films: Dewetting and Polymer Flow* (Springer, 2012).

[5] T. Salez, J. D. McGraw, O. Bäumchen, K. Dalnoki-Veress, and E. Raphaël, Phys. Fluids **24**, 102111 (2012).

[6] M. Benzaquen, T. Salez, and E. Raphaël, Eur. Phys. J. E. Soft Matter **36**, 82 (2013).

[7] M. Benzaquen, P. Fowler, L. Jubin, T. Salez, K. Dalnoki-Veress, and E. Raphaël, Soft Matter **10**, 8608 (2014).

[8] M. Backholm, M. Benzaquen, T. Salez, E. Raphaël, and K. Dalnoki-Veress, Soft Matter **10**, 2550 (2014).

3.4 Paper IV - Freestanding thin film flow

Mark Ilton, Miles Couchman, Thomas Salez, Michael Benzaquen, Paul Fowler, Elie Raphaël, and Kari Dalnoki-Veress "Capillary leveling of a freely-suspended viscous film", submitted (2015).

3.4.1 Preface to Paper IV

Here, the flow in freestanding films described in Section 1.4.3 of this thesis was experimentally measured using capillary levelling. By monitoring the evolution of an initial step profile, we find that the width of the step w broadens as a power law in time as $w \propto (v_c h_0 t)^{1/2}$, where h_0 is a characteristic thickness and v_c is the capillary velocity. This scaling agrees with the freestanding thin film equation derived in Section 1.4.3. Therefore, we have experimentally measured flow which is consistent with pure plug flow.

Another interesting aspect of freestanding flow is the linearization of the freestanding thin film equation, which is equivalent to the heat equation. This has an analytical solution for a Heaviside step profile given by the error function $\mathrm{erf}(x) = \frac{2}{\pi}\int_0^x e^{-\phi^2}\,d\phi$. We show that experimentally measured profiles are described by the error function for the case where the step is much thinner that the overall film thickness.

Finally, as a consistency check, the levelling of both freestanding and supported steps of 55 kg/mol was measured simultaneously by placing samples of each type side-by-side in a vacuum oven. With freestanding or supported levelling, the capillary velocity is extracted by fitting to solutions of the freestanding or supported thin film equation. Since the two types of samples are the same liquid at the exact same temperature, the extracted capillary velocity should be the same. Using the freestanding thin film equation presented in Section 1.4.3 of this thesis gives a freestanding capillary velocity which is three times smaller than the supported capillary velocity. This discrepancy is resolved by including a viscous stress term in the pressure, as is done in the paper. The end result is that equation 1.79 presented in this thesis is not complete and the left-hand side needs to be multiplied by 3 to give:

$$3\frac{\partial h}{\partial t} = \frac{\gamma}{\eta}\frac{\partial}{\partial x}\left(h\frac{\partial h}{\partial x}\right). \tag{3.1}$$

The sample preparation and measurement were quite difficult: freestanding films can easily rupture, temperature gradients can occur due to poor thermal conductivity of the films, and measuring a freestanding film with AFM is especially challenging. This work was the result of the perseverance of a talented B.Sc. thesis student Miles Couchman, who performed most of the measurements in this paper. In this work, I co-supervised Miles, helped with experiments, performed analysis, wrote a first version of the paper, and helped revise the manuscript.

Capillary leveling of a freely-suspended viscous film

Mark Ilton,[1] Miles Couchman,[1] Thomas Salez,[2] Michael Benzaquen,[2]
Paul Fowler,[1] Elie Raphaël,[2] and Kari Dalnoki-Veress[1, 2, *]

[1] *Department of Physics & Astronomy and the Brockhouse Institute for Materials Research, McMaster University, Hamilton, Ontario, Canada, L8S 4M1*
[2] *Laboratoire de Physico-Chimie Théorique, UMR CNRS Gulliver 7083, ESPCI ParisTech, PSL Research University, 75005 Paris, France*

(Dated: September 29, 2015)

We measure the capillary-driven leveling of viscous, thin free-standing polystyrene films using atomic force microscopy. Films with an initially heaviside step profile broaden in time, with a step width that increases with the square root of time. A continuum fluid dynamics model is developed which assumes a constant velocity profile along the thickness of the film (plug flow), leading to a second order partial different equation: the free-standing thin film equation. Solutions to this equation agree with the experimentally measured height profiles. The use of the free-standing step-leveling geometry is a promising experimental candidate to study the enhanced mobility previously observed in both free-standing glassy films and polymer films under confinement.

Continuum fluid dynamics gives a remarkably accurate description of liquid flow on lengthscales ranging from tens of nanometers to astronomical sizes, and can accommodate a variety of forces that drive or mediate flow (e.g. gravity, surface tension, inertia, viscosity). Surface tension driven flow mediated by viscosity is a particularly interesting regime as these two forces dominate in many technologically relevant applications (e.g. thin films, microfluidics) [1, 2] where flow occurs on small lengthscales. Moreover, in this regime simplifications can be made which allow for conceptually simple experiments that probe underlying physics internal to the fluid. For example, assumptions about the molecular motion of fluid particles at a solid interface can be tested [3]. A thin film geometry allows further simplification, since the majority of flow occurs in plane of the film [4]. In this regime, the fluid dynamics are determined by the capillary velocity $v_c = \gamma/\eta$ (the ratio of surface tension to viscosity) along with a characteristic film thickness.

Research in this area has largely been focused on a thin film of fluid which coats a solid substrate. One way to probe the dynamics of such a film is by applying a stress to the film and measuring the departure from its initial state. This can be achieved with a variety of experimental techniques, such as a dynamic surface force apparatus [5], nanoparticle embedding [6–8], electrohydrodynamic instability [9–11], unfavorable wetting conditions [3, 12–18], and Marangoni flow [19–22]. Alternatively, dynamics of a thin coating of fluid can be probed by starting with an initial strain and measuring the film as it relaxes towards equilibrium. The initial strain can be accomplished by starting with a film flatter than this equilibrium roughness [23–26], or by purposefully applying an initial perturbation [25, 27–37]. Both of these approaches, an applied stress or an initial strain, can be used to study physical phenomena like the glass transition [6–8, 25, 27, 36], viscoelasticity [32, 34, 35], and address questions about interfacial molecular friction [3, 17, 18]. The initial strain measurements have the added benefit of simplicity since the only forces involved are properties of the fluid (surface tension and viscosity).

In contrast to studies of thin fluid films coating a solid substrate, here we examine surface tension driven flow mediated by viscosity in a configuration with no interfacial friction: a freely-suspended film. Instead of supporting the film underneath with a substrate, the film is supported at its edges creating a membrane or free-standing film. A useful visualization is to picture cling wrap covering the opening of a bowl, except the free-standing films here are orders of magnitude thinner than cling wrap and are in the liquid state. Flow in free-standing films has been previously studied for fluids which have some internal structure which stabilizes the film against rupture, such as surfactant stabilized films of water (soap films) [38–42] or liquid crystalline films with some molecular order [43–45]. In those two cases, the structure has a significant impact on the flow dynamics. In this letter, we examine an idealized system where the only friction in the flow is internal to the liquid and due to its isotropic viscosity. Boundary conditions on a thin viscous film can have a significant impact on flow, and the free-standing films we study here are in an interesting and extreme limit of zero interfacial molecular friction.

Working with nanoscopically thin films which are able to flow presents experimental challenges in both the creation of stable films and in their measurement. Experimental techniques used to characterize flow in supported films typically do not work in the free-standing geometry. However, the potential application of a free-standing flow geometry to study physical phenomena is compelling. Previous studies have found that the glass transition temperature reductions observed for supported films are even more pronounced for free-standing films [46]. As well, a free-standing film provides an ideal system to study molecular confinement effects of polymeric liquids due to the absence of any fluid-substrate interaction.

To characterize free-standing film dynamics, we use a convenient initial-strain geometry known as step leveling [31, 47], where a film with a sharp edge is placed upon a second film made of the same material [see schematic in Fig. 1(a)]. The edge has excess surface area which drives flow, causing the step to broaden over time thereby reducing the surface area. The broadening of the step is a measure of the fluid's capillary velocity. Previous step leveling experiments of thin polystyrene films on a supported substrate have shown that the width of the profile, w, increases as a power-law in time t as [31]

$$w \propto \left(v_c h_2^3 t\right)^{1/4}, \qquad \text{(supported)} \qquad (1)$$

where h_2 is the thickness of the film with the sharp edge [shown schematically in Fig 1(a)]. Eq. (1) is derived from the thin film equation [31], which is Stokes equation in the thin film regime with a no-slip boundary condition at the solid-liquid interface. This no-slip condition, which assumes zero horizontal velocity at the fluid-solid interface, results in a parabolic velocity profile in the film (Poiseuille flow) which is largest at the liquid-air interface. In this letter, first we empirically determine the scaling law for the profile width for the case of a free-standing film. Then, by modifying the boundary conditions in the theory, we derive a free-standing thin film equation consistent with our observations. Experimentally measured atomic force microscopy (AFM) profiles show excellent agreement to solutions of the free-standing thin film equation. Finally, by performing simultaneous measurements of supported and free-standing films, we show that the measured capillary velocity is independent of the boundary conditions on the film.

The free-standing samples were prepared using a similar protocol as the preparation of supported step leveling films [47]. Here, thin polystrene films (polymer obtained from Polymer Source, Canada with weight-averaged molecular weight 55 kg/mol) with thickness ranging from $\sim 100-500\,\mathrm{nm}$ were spuncast from dilute toluene solution onto mica (Ted Pella, USA) and pre-annealed in a home-built vacuum oven for 12 hours at 140°C, well above the glass transition temperature $T_g \approx 100°\mathrm{C}$ of the films. After annealing, the films were floated onto a deionized water bath (18.2 MΩ cm, Pall, USA) and picked up onto custom-machined stainless steel grids. Each grid had 85 hexagonal holes, roughly 1 mm across, which allowed each free-standing film to be sectioned off into smaller regions. Having the film sectioned off by the grid stopped the growth of nucleated holes into other regions of the film. This prevented rupture from destroying the thin free-standing films. Each grid had up to 85 parallel experiments, most of which were not stable over the course of the entire experiment. The results described in this letter are from the portions of the grid that were stable. After floating a film onto a grid, the film was heated above T_g to remove any wrinkles caused by floating. A second film with a sharp edge created by a floating induced gap [48] (with thickness h_2) was then floated on top of the initial film (with thickness h_1) schematically shown in Fig. 1(a). The stepped films were then annealed at $T_g + 10°\mathrm{C} \approx 110°\mathrm{C}$ on a hot stage (Linkham, UK) for an annealing time t. To minimize the excess surface area, the films underwent a "symmetrization" shown schematically in Fig. 1(b). The step which was originally created on one side of the film, rapidly develops into a step on both sides of the film with a plane of mirror symmetry in the center. Because the vertical length-scale is orders of magnitude smaller than the typical horizontal length-scale, the symmetrization occurs rapidly (on the order of seconds), and could not be resolved in our experiments. A slower process that could be measured is the broadening of the stepped films. To measure the height profile of the step, the films were cooled rapidly ($> 90°\mathrm{C/min}$) to room temperature, deep into the glassy state, and then measured using AFM (Veeco Caliber, USA). Since using AFM on a thin, solid membrane can easily lead to noise due to resonance between the oscillating AFM tip and the freely-suspended film, extra caution was required to avoid acoustic noise. After imagining, the films were placed back on the hot stage and rapidly heated back above T_g to continue the leveling process. Because appreciable flow does not occur at room temperature, the films could be intermittently imaged at room temperature with no affect on the dynamics above T_g.

The time evolution of a free-standing stepped film is shown in the main panel of Fig. 1(c). The step was prepared by stacking two films of identical thickness ($h_1 = h_2 = 176\,\mathrm{nm}$). The initially sharp step profile broadens over time. To characterize the broadening, the width of the profile as a function of annealing time was measured. The width was extracted by fitting a tangent line to the center of the profile and multiplying the inverse of the slope by the step height [47], as shown by the schematic in the inset of Fig. 1(c). The width of the step is consistent with a $t^{1/2}$ power law [red open circles in Fig. 2(a)] at late times. At small values of t, the width shows a small deviation from the power-law behavior, consistent with previous work [31, 34] which attribute this deviation to residual stresses in the film (e.g. interfacial healing between the two stacked films). Also shown in Fig. 2(a) are the results for two other measured steps with $h_1 = h_2$, which also follow a $t^{1/2}$ scaling of the width. Each dataset in Fig. 2(a) is fit to $w = (Mt)^{1/2}$. The prefactor M scales linearly with h_2 [Fig. 2(b)]. Using dimensional analysis, this empirically gives free-standing version of Eq. (1) as

$$w \propto \left(v_c h_2 t\right)^{1/2}. \qquad \text{(free-standing)} \qquad (2)$$

The scaling of the width in the free-standing case has a similar form to the supported case in Eq. (1), but with different power-law exponents. The width has a stronger dependence on time in free-standing films compared to supported films, which is consistent with free-standing

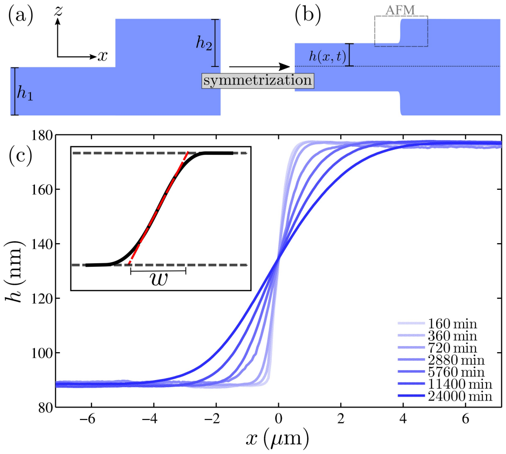

FIG. 1. (a) Schematic of a stepped free-standing film, prepared by stacking a film with a sharp edge and thickness h_2 on top of a film with thickness h_1. (b) After annealing above the glass transition temperature, a plane of symmetry quickly develops (dotted line), and the initially sharp step begins to broaden. The height profile from the plane of symmetry, $h(x,t)$, is measured by an AFM scan of the top surface. (c) AFM profiles of a stepped film with $h_1 = h_2 = 176\,\text{nm}$ are shown for different annealing times t above T_g. The width of the AFM profiles is defined by the intersection of tangent line at the center of the profile with the two flat regions of the film, as shown in the inset.

films flowing more readily due to their unconstrained boundaries.

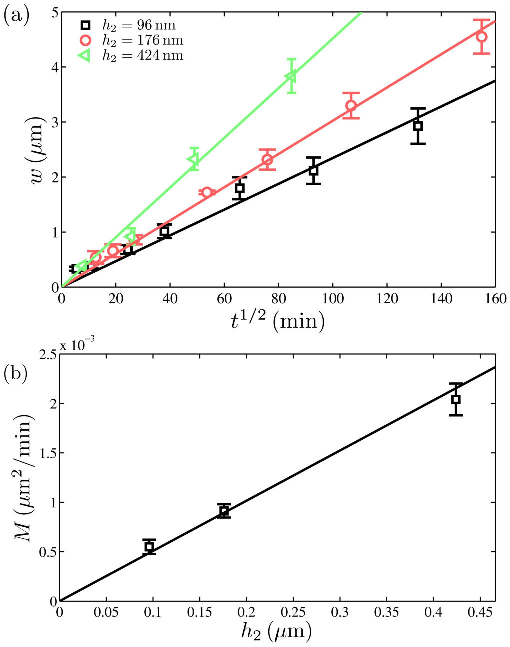

FIG. 2. (a) The AFM profile width w is consistent with a $t^{1/2}$ scaling for free-standing stepped films with $h_1 = h_2$. The open symbols are the measured widths for three different film thicknesses h_2. The solid lines are fits to $w = (Mt)^{1/2}$, where $M(v_c, h_2)$ is a fitting coefficient. (b) The fitting coefficent M scales linearly with the characteristic film thickness h_2. Combining the results of (a) and (b), and enforcing dimensional consistency gives Eq. (2).

Armed with the motivation from the empirical scaling of Eq. (2), we develop a theoretical description of the free-standing flow. Let us consider a symmetric free-standing film of total thickness $2 \times h(x,t)$ shown schematically in Fig. 1(b). At $z = 0$ (the axis of symmetry) the boundary conditions are:

$$v = 0 \tag{3}$$

$$\partial_z u = 0, \tag{4}$$

where u and v are respectively the horizontal and vertical velocities. Since at the liquid-air interfaces there is no appreciable friction, there is a no-stress boundary condition at $z = h$

$$\partial_z u = 0 \tag{5}$$

$$p = -\gamma \partial_x^2 h + \sigma_{zz}, \tag{6}$$

where $\sigma_{zz} = 2\eta \partial_z v|_{z=h}$. This implies that the flow cannot be Poiseuille type flow as it is for the supported case. Here we make the hypothesis of plug flow, where the horizontal velocity is uniform along the z direction, i.e. $u = u(x,t)$. The leading non-vanishing order of the dynamical equations yield:

$$\eta \partial_x^2 u = \partial_x p \tag{7}$$

$$\partial_x u + \partial_z v = 0. \tag{8}$$

Integrating Eq. (7) twice with respect to x together with Eq. (6) and Eq. (8) leads to

$$3u = -v_c \partial_x h, \tag{9}$$

where the constants of integration are set to zero by taking into account that u is constant when the film is flat. Applying the conservation of volume constraint $\partial_t h = -\partial_x(hu)$, gives the free-standing thin film equation (FSTFE):

$$\partial_t h = \frac{v_c}{3} \partial_x (h \partial_x h). \tag{10}$$

Eq. (10) can be nondimensionalized if we let $H = h/h_2$, $X = x/h_2$, and $T = v_c t/3h_2$. Proceeding in a similar manner as ref. [31], by introducing the variable

$$U = \frac{X}{T^{1/2}} = x \left(\frac{3}{v_c h_2 t} \right)^{1/2}, \tag{11}$$

one can show the existence of self-similar solutions of the form $H(X,T) = F(U)$. In other words, solutions to the FSTFE with dimensionalized variables can be related to the self-similar solution $F(U)$ by means of equation (11). At fixed values of U, this relation confirms the empirical scaling of Eq. (2).

The theory can also be used to determine the full height profile of free-standing films as they flow. By employing a numerical scheme [49], solutions to Eq. (10) were calculated and fit to the experimental data. Fig. 3(a) shows a typical experimental profiles (red lines) for the step with $h_1 = h_2 = 176\,\text{nm}$. The normalized height is plotted against the normalized horizontal position $x/t^{1/2}$ for three different annealing times. The three experimental profiles collapse onto one curve and agree well with the numerically calculated theory (green line). The difference between the experiment and theory is less than 1 nm [red lines in Fig.3(b)]. There is a similar level of agreement between the theory and experiment for the other measured self-similar profiles with $h_1 = h_2$.

A further simplification can be made in the case where the size of the surface perturbation is small in comparison to the overall thickness of the film. This situation can be experimentally realized by creating a stepped film with $h_1 >> h_2$. In that case, the nondimensionalized height profiles can be written as $H(X,T) = 1 + \Delta(X,T)$, with $\Delta << 1$. One can show that to first order Eq. (10) reduces to a simple diffusion equation

$$\partial_T \Delta = \partial_X^2 \Delta. \tag{12}$$

This linearized version of the free-standing thin film equation has an analytic solution

$$F(U) = 1 + \frac{\Delta_0}{2}(\text{erf}(U/2) + 1). \tag{13}$$

To test the linearized theory, a sample with $h_1 = 681\,\text{nm}$ and $h_2 = 92\,\text{nm}$ was annealed above T_g and measured with AFM. The linearized theory [yellow line in Fig. 3(a)] shows remarkable agreement to the collapsed AFM data [blue lines in Fig 3(a)], with $< 0.5\,\text{nm}$ deviation over the entire profile as shown by the blue lines in Fig. 3(b). In short, there is an excellent agreement between the theory and experiment. Not only is the experimentally measured scaling law reproduced by the theory, the profile of the stepped films as they evolve in time agrees with both numeric and linearized analytic solutions to the FSTFE.

A final experiment was performed to compare the capillary velocity measured in a free-standing film to ensure that it is equivalent to the supported film value. Both supported and free-standing PS stepped films were annealed side-by-side at the same time. Since the capillary velocity is a material property of the film independent of the substrate, the supported samples should have an equivalent v_c to the free-standing films. Stepped PS films ($h_1 = h_2 = 390\,\text{nm}$) were created on the free-standing grids as well as on supported substrates (both silicon and $\approx 4\mu\text{m}$ thick polysulfone films were used as substrates to ensure the substrate thickness did not affect the temperature of the PS film). The samples were placed in a home-built vacuum oven at 120°C, where a metal cap was clamped above the samples to ensure there were no temperature gradients in the vacuum oven. The samples were measured after 735 and 1485 minutes of annealing to confirm that the measured profiles were self-similar in time. Fig. 4(a) shows the results of the supported measurements. The normalized height of the step for 10 different supported profiles is plotted as a function of the normalized horizontal position ($x/t^{1/4}$). The collapse of the profiles for the two different annealing times shows that the flow is self-similar in $t^{1/4}$ as is the case for supported thin-film flow [Eq.(1)]. The theoretical profile [49] is fit to the experimental data with only one free parameter, v_c. This gives the capillary velocity of PS ($55\,\text{kg/mol}$ at 120°C) as $v_c = 0.068 \pm 0.008\,\mu\text{m/min}$ in the supported case. Fig. 4(b) shows the results of the free-standing measurements, plotting the normalized height of the profiles as a function of the normalized horizontal position $x/t^{1/2}$. There is a collapse of all 16 free-standing profiles for the two different annealing times,

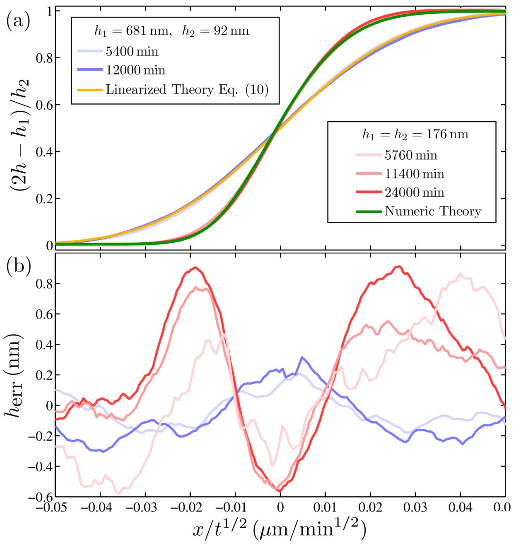

FIG. 3. (a) Normalized height profile plotted as a function of normalized horizontal position for two different samples. A sample with $h_1 = h_2$ (bottom right legend), which agrees well with the calculated numeric solution to Eq. (10), and a sample with $h_1 > h_2$ (top left legend) which agrees with the analytic linearized solution of Eq. (12). (b) The residuals of the fits to the theoretical profiles show a $< 1\,\text{nm}$ deviation for both the sample with $h_1 = h_2$ (red solid lines) and $h_1 > h_2$ (blue solid lines). The colors correspond to the same annealing times as the legend in panel (a).

reconfirming the $t^{1/2}$ self-similarity predicted by the theory. Similarly, the numeric theory (from Fig. 3) is fit to the collapsed profile with one free parameter (v_c), which gives $v_c = 0.065 \pm 0.005$ in agreement with the supported measurement. The fact that the free-standing measurement gives the same capillary velocity as the supported measurement proves the robustness of the step leveling technique. Having a well-characterized technique to measure flow in a free-standing geometry opens new avenues of research in the study of thin fluid membranes.

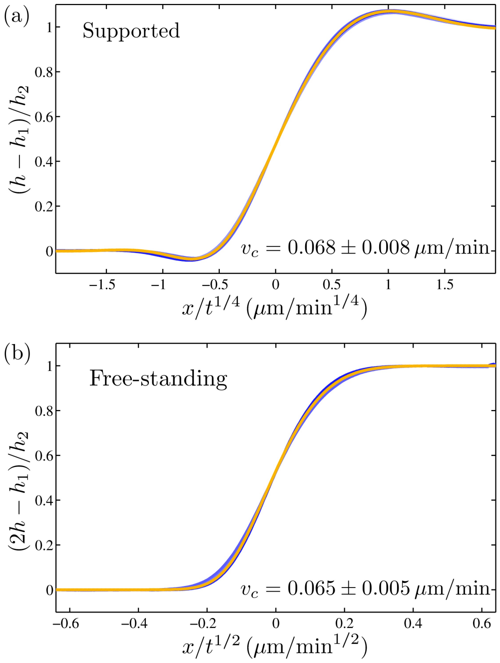

FIG. 4. (a) Step leveling measurement of supported films. The 10 different experimentally measured profiles for two different annealing times (solid blue lines) collapse when plotted as a function of the rescaled horizontal position $x/t^{1/4}$ which indicates self-similarity. The numerical solution to the thin film equation [31] (solid yellow line) is fit to the experimental profiles which gives v_c. (b) A step leveling measurement of free-standing films performed simultaneously to the supported measurement. Here, the 12 free-standing profiles for the same two annealing times collapse as a function of the normalized horizontal position $x/t^{1/2}$. The capillary velocity is determined by fitting the numeric solution to the FSTFE Eq. (10) to the experimental profiles, and is in agreement with the supported measurement.

In summary, we have measured flow in thin free-standing polystyrene films using a stepped film geometry. The steps broaden as they are annealed above T_g, and the width of the step follows a $t^{1/2}$ power law. Unlike a supported film with a no-slip liquid-solid boundary condition, the flow in free-standing films is consistent with theory derived from an assumption of plug flow, i.e. a uniform flow velocity along the thickness of the film. The free-standing thin film equation (Eq. (10)) reproduces the both the empirical scaling law and AFM profiles. The capillary velocity was determined to be independent of the film's boundary condition by a simultaneous measurement of supported and free-standing films. Using free-standing capillary leveling to study flow in thin films should readily allow for its application to unresolved physical problems. Probing the flow of thin free-standing films just below their glass transition temperature would provide insight into the mechanism behind large T_g reductions. Comparing the response of supported and free-standing films made of high molecular weight polymer would clarify the role that the substrate plays in systems that demonstrate a viscosity reduced by confinement [26].

---

* dalnoki@mcmaster.ca

[1] K. Jacobs, R. Seemann, and S. Herminghaus, in *Polym. Thin Film.*, edited by O. K. C. Tsui and T. P. Russell (World Scientific, 2008) Chap. 10, pp. 243–265.
[2] P. Tabeling, *Introduction to Microfluidics* (Oxford University Press, 2005).
[3] O. Bäumchen and K. Jacobs, J. Phys. Condens. Matter **22**, 033102 (2010).
[4] R. Blossey, *Thin Liquid Films: Dewetting and Polymer Flow* (Springer, 2012).
[5] J. N. Israelachvili, P. M. McGuiggan, and A. M. Homola, Science **240**, 189 (1988).
[6] J. H. Teichroeb and J. A. Forrest, Phys. Rev. Lett. **91**, 016104 (2003).
[7] M. Ilton, D. Qi, and J. A. Forrest, Macromolecules **42**, 6851 (2009).
[8] D. Qi, M. Ilton, and J. A. Forrest, Eur. Phys. J. E. Soft Matter **34**, 1 (2011).
[9] E. Schaffer, T. Thurn-Albrecht, T. Russell, and U. Steiner, Nature **403**, 874 (2000).
[10] M. D. Morariu, N. E. Voicu, E. Schäffer, Z. Lin, T. P. Russell, and U. Steiner, Nat. Mater. **2**, 48 (2003).
[11] N. Voicu, S. Harkema, and U. Steiner, Adv. Funct. Mater. **16**, 926 (2006).
[12] D. J. Srolovitz and S. A. Safran, J. Appl. Phys. **60**, 255 (1986).
[13] F. Wyart and J. Daillant, Can. J. Phys. **68**, 1084 (1990).
[14] R. Seemann, S. Herminghaus, and K. Jacobs, Phys. Rev. Lett. **87**, 196101 (2001).
[15] G. Reiter, M. Hamieh, P. Damman, S. Sclavons, S. Gabriele, T. Vilmin, and E. Raphaël, Nat. Mater. **4**, 754 (2005).
[16] X.-C. Chen, H.-M. Li, F. Fang, Y.-W. Wu, M. Wang, G.-B. Ma, Y.-Q. Ma, D.-J. Shu, and R.-W. Peng, Adv. Mater. **24**, 2637 (2012).
[17] O. Bäumchen, R. Fetzer, and K. Jacobs, Phys. Rev. Lett. **103**, 1 (2009).
[18] O. Bäumchen and K. Jacobs, Soft Matter **6**, 6028 (2010).
[19] C. B. Kim, D. W. Janes, D. L. McGuffin, and C. J. Ellison, J. Polym. Sci. Part B Polym. Phys. **52**, 1195

(2014).

[20] J. M. Katzenstein, C. B. Kim, N. A. Prisco, R. Katsumata, Z. Li, D. W. Janes, G. Blachut, and C. J. Ellison, Macromolecules **47**, 6804 (2014).

[21] T. A. Arshad, C. B. Kim, N. A. Prisco, J. M. Katzenstein, D. W. Janes, R. T. Bonnecaze, and C. J. Ellison, Soft Matter **10**, 8043 (2014).

[22] J. M. Katzenstein, D. W. Janes, J. D. Cushen, N. B. Hira, D. L. McGuffin, N. A. Prisco, and C. J. Ellison, ACS Macro Lett. , 1150 (2012).

[23] O. K. C. Tsui, Y. J. Wang, F. K. Lee, C.-H. Lam, and Z. Yang, Macromolecules **41**, 1465 (2008).

[24] Z. Yang, C. H. Lam, E. Dimasi, N. Bouet, J. Jordan-Sweet, and O. K. C. Tsui, Appl. Phys. Lett. **94**, 3 (2009).

[25] Z. Yang, Y. Fujii, F. K. Lee, C.-H. Lam, and O. K. C. Tsui, Science **328**, 1676 (2010).

[26] F. Chen, D. Peng, C.-H. Lam, and O. K. C. Tsui, Macromolecules , 150709130643005 (2015).

[27] Z. Fakhraai and J. A. Forrest, Science (80-.). **319**, 600 (2008).

[28] T. Leveder, S. Landis, and L. Davoust, Appl. Phys. Lett. **92**, 013107 (2008).

[29] T. Leveder, E. Rognin, S. Landis, and L. Davoust, Microelectron. Eng. **88**, 1867 (2011).

[30] E. Rognin, S. Landis, and L. Davoust, Phys. Rev. E **84**, 041805 (2011).

[31] J. D. McGraw, T. Salez, O. Bäumchen, E. Raphaël, and K. Dalnoki-Veress, Phys. Rev. Lett. **109**, 1 (2012).

[32] E. Rognin, S. Landis, and L. Davoust, J. Vac. Sci. Technol. B Microelectron. Nanom. Struct. **30**, 011602 (2012).

[33] M. Benzaquen, T. Salez, and E. Raphaël, Eur. Phys. J. E. Soft Matter **36**, 82 (2013).

[34] M. Benzaquen, P. Fowler, L. Jubin, T. Salez, K. Dalnoki-Veress, and E. Raphaël, Soft Matter **10**, 8608 (2014).

[35] E. Rognin, S. Landis, and L. Davoust, Langmuir **30**, 6963 (2014).

[36] Y. Chai, T. Salez, J. D. McGraw, M. Benzaquen, K. Dalnoki-Veress, E. Raphaël, and J. a. Forrest, Science (80-.). **343**, 994 (2014).

[37] M. Benzaquen, M. Ilton, M. V. Massa, T. Salez, P. Fowler, E. Raphaël, and K. Dalnoki-Veress, Appl. Phys. Lett. **107**, 053103 (2015).

[38] M. A. Rutgers, X.-l. Wu, R. Bhagavatula, A. A. Petersen, and W. I. Goldburg, Phys. Fluids **8**, 2847 (1996).

[39] V. Horváth, J. Cressman, W. Goldburg, and X. Wu, Phys. Rev. E **61**, R4702 (2000).

[40] D. Georgiev and P. Vorobieff, Rev. Sci. Instrum. **73**, 1177 (2002).

[41] H. Diamant, J. Phys. Soc. Japan **78**, 041002 (2009).

[42] M. J. Huang, C. Y. Wen, I. C. Lee, and C. H. Tsai, Phys. Fluids **16**, 3975 (2004).

[43] K. Harth, A. Eremin, and R. Stannarius, Soft Matter **7**, 2858 (2011).

[44] A. Eremin, C. Bohley, and R. Stannarius, Phys. Rev. E - Stat. Nonlinear, Soft Matter Phys. **74**, 1 (2006).

[45] R. Stannarius, C. Bohley, and A. Eremin, Phys. Rev. Lett. **97**, 1 (2006).

[46] K. Dalnoki-Veress, J. A. Forrest, C. Murray, C. Gigault, and J. R. Dutcher, Phys. Rev. E. Stat. Nonlin. Soft Matter Phys. **63**, 031801 (2001).

[47] J. D. McGraw, N. M. Jago, and K. Dalnoki-Veress, Soft Matter **7**, 7832 (2011).

[48] O. Bäumchen, M. Benzaquen, T. Salez, J. D. McGraw, M. Backholm, P. Fowler, E. Raphaël, and K. Dalnoki-Veress, Phys. Rev. E **88**, 035001 (2013).

[49] T. Salez, J. D. McGraw, S. L. Cormier, O. Bäumchen, K. Dalnoki-Veress, and E. Raphaël, Eur. Phys. J. E **35**, 114 (2012).

3.5 Paper V - Stability of holes in a freestanding film

Mark Ilton, Christian DiMaria, and Kari Dalnoki-Veress "Direct measurement of the critical pore size in a model membrane", submitted (2015).

3.5.1 Preface to Paper V

Freestanding polystyrene films were also the subject of this work, focusing on the stability and evolution of holes (pores) created in the film. The freestanding films in this work ranged in thickness from $\sim 100\,\mathrm{nm} - 2\,\mu\mathrm{m}$. A pore in a membrane was created by exposing a supported PS film to the focused laser spike annealing procedure with a stationary sample stage. Laser exposure continued until the substrate was exposed in a small circular region of the film. The film could then be transferred into the freestanding state, yielding a freely-suspended polymer membrane with a pore. The initial size of the pore could be tuned by changing the laser power or exposure time.

In these experiments, films were created with arrays of hundreds of pores of varying size. When the films were heated above their glass transition temperature to allow for flow, the radius of some of the pores grew exponentially in time, consistent with previous measurements of rupture in thin viscous films. Other pores were observed to shrink, and closed over time. A select few of the hundreds of pores did not grow or shrink over the course of the measurement. These unchanging pores define a critical radius for pore growth. This critical radius r_c was measured for 9 different thicknesses of PS, and it was found that the critical radius scaled linearly with film thickness $r_c \propto h$.

These experiments relate to the phenomena of nucleation and growth. In the case of pore formation in a viscous film, creating a pore reduces the surface area at the two air interfaces in the plane of the membrane. This gives a reduction in the free energy proportional to the area of the pore in the plane (energy reduction $\propto 2\pi r^2\gamma$). However, at the edge of the pore there is an increase in the free energy cost proportional to the perimeter of the pore. The energy cost per unit length of perimeter, known as the line tension, depends on the curvature of the interface at the edge of the pore, as well as any molecular rearrangements that might occur near the pore to accommodate the curved interface.

For the case of the PS membrane, we assume that the line tension contribution to the free energy is the surface tension cost of creating a torus shape at the edge of the pore. This gives $r_c = \pi h/4$, which agrees with the experimentally measured data with no fitting parameters. To change the line tension, a PS-PMMA diblock copolymer is used. Layers of molecules at the edge of the pore then need to undergo a rearrangement to accommodate the curvature of the pore. This extra line tension cost increases the critical radius of pores for thin films.

This work, much like the other freestanding project, involved difficult sample preparation and measurement. Here as well, a bright and determined undergraduate student Christian DiMaria was instrumental in this work. For my contribution, I co-supervised Christian, designed and performed initial proof-of-concept experiments, developed a model for the diblock copolymer films, wrote the first draft of the paper, and was involved in the revision of the manuscript.

Direct measurement of the critical pore size in a model membrane

Mark Ilton,[1] Christian DiMaria,[1] and Kari Dalnoki-Veress[1, 2, *]
[1]*Department of Physics & Astronomy and the Brockhouse Institute for Materials Research,*
McMaster University, Hamilton, Ontario, Canada, L8S 4M1
[2]*Laboratoire de Physico-Chimie Théorique, UMR CNRS Gulliver 7083,*
ESPCI ParisTech, PSL Research University, 75005 Paris, France

(Dated: October 20, 2015)

We study pore nucleation in a model membrane system, a freestanding polymer film. Nucleated pores smaller than a critical size close, while pores larger than the critical size grow. Holes of varying size were purposefully created in liquid polymer films, and their evolution in time was monitored using optical and atomic force microscopy to extract a critical radius. The critical radius scales linearly with film thickness for a homopolymer film. The results agree with a simple model which takes into account the energy cost due to surface area at the edge of the pore. The effect of having an additional energy cost at the edge of the pore was studied using a diblock copolymer, where molecular rearrangements at the edge of the pore cause an increased tension at the edge of the pore.

Nucleation and growth occurs in a variety of physical systems where there is a phase transition. Crystallization of ice, the formation of micelles in solution, and the growth of diamonds from vitreous carbon are all systems where a nucleus can form and then either grow or shrink depending on its size [1]. In crystallization, for example, there is a trade-off between the volumetric free energy contribution which favors the crystalline phase, and the surface area dependent cost of the interfacial tension between the two phases which favors a single liquid phase [2]. By examining the free energy cost of creating a nucleated phase with radius r, the critical radius r_c can be derived from classical nucleation theory. For a nucleus with $r < r_c$, the nucleated phase is unstable to fluctuations, while for $r > r_c$ the nucleated phase is energetically favorable and the nucleus can grow. The same physics governs diverse phenomena including bubble nucleation of false vacuum states in inflationary cosmology [3], as well as many biologically important processes such as amyloid-beta protein aggregation [4, 5], microtubule growth [6], and pore formation in cell membranes [7]. In this letter we focus on pore formation in a membrane. Membrane pores can be created by pathogenic bacteria to invade target cells [8], and play an important role in many biological processes such as mechanical force transduction [9] and water permeability of biological membranes [10].

For the nucleation of a pore in a membrane, there is a balance between a two competing effects. First, there is an energy cost of having an interface between the membrane and its surrounding phase. Because the presence of a pore removes interface, this reduces the interfacial energy cost. Opposing this effect is the energetic cost of creating an edge around the perimeter of the pore. The stability and growth of pores depends on the relative contribution of interface reduction compared to the edge cost. Written mathematically, the free energy cost of creating a pore in a membrane which has two surfaces with interfacial tension γ is given by [11]

$$\Delta G(r) = 2\pi r\Gamma - 2\pi r^2\gamma, \tag{1}$$

where Γ is the line tension (or edge tension) of the pore, which is the free energy cost per unit length of creating interface at the edge of the pore [see schematic in Fig.1(a)]. The line tension in lipid membranes has been the subject of both experimental [12–19] and theoretical [20–26] studies, which address important questions about the composition profile of the lipid molecules around the pore edge [21, 25] as well as the role of peptides in the free energy of the pore [17–19]. An experimental challenge working with lipid membranes is their size. Typically the thickness of such membranes is a few nanometers, while pores can be sub-nanometer in size.

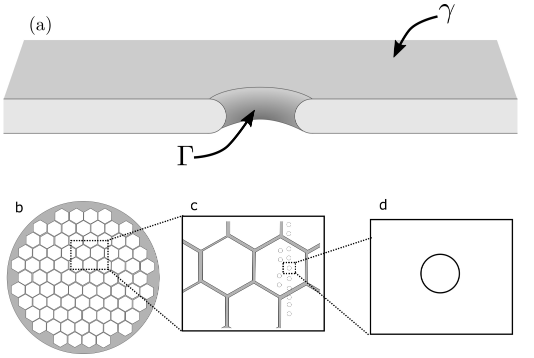

FIG. 1. (a) Cross-sectional diagram of a pore in a membrane with interfacial tension γ and line tension Γ. (b) Schematic of the grids used to support the freestanding polymer membranes. Each hexagon is ∼ 1 mm across. (c) Optical microscopy image of a sample with hundreds of holes of various sizes. (d) The size of the hole is monitored with optical microscopy after annealing above the glass transition temperature of the polymer. Because the polymer is in the liquid state, pores can grow or shrink depending on their size.

Here we study the formation of pores in a model membrane system, a thin freely-suspended polymer film. Previously, viscous polymer membranes have been used as a model system to study the growth dynamics of rupture in bubbles [27] as well as to study the spontaneous nucleation and growth of holes [28–30]. Our approach is to purposefully make holes of various sizes in a liquid polymer membrane and allows them to evolve under the force of surface tension. Holes with a radius below the critical radius fill in, while those larger than the critical radius grow. Examining the shrinkage or growth of many holes allow for the determination of r_c which depends on the film thickness h.

To create the polymer membranes, monodisperse polystyrene (obtained from Scientific Polymer Products, USA, $M_n = 48\,\mathrm{kg/mol}$) was spincast from dilute toluene solution onto freshly cleaved mica (Ted Pella, USA). The polystyrene (PS) films were then floated off the mica onto a deionized water bath (18.2 MΩ cm, Pall, USA), and transfered onto silicon (University Wafer, USA). Pores in the polystyrene film were created by a focused laser spike annealing setup [31–33], where a tightly focused laser (Coherent, Verdi V2, 532 nm) was used to locally heat the silicon wafer supporting the PS film. This heating had two effects. First, the local temperature of the PS film became greater than its glass transition temperature ($T_g \approx 100$°C), which created a local region of liquid PS. Second, the laser caused a lateral temperature gradient within the PS film, and because the surface tension of PS decreases with increasing temperature, thermocapillary flow created an axisymmetric dewetted region around the center of the laser beam. By varying the power and exposure time of the laser, holes of various sizes in the PS film could be created. The process of exposing the film to the laser, closing the laser shutter and then translating the sample to a new location was repeated to yield hundreds of holes in each PS film. Having hundreds of holes ensured a good statistical average for the critical radius measurement. After exposure to the laser, the films were then floated off the silicon back onto the water bath, and picked up onto stainless steel grids shown schematically in Fig. 1(b). The edge of the grids supported the PS film, with a freely-suspended region of PS film in the center. The films were then heated above T_g on a heating stage (Linkham, UK) to bring them into the liquid state. The size of the pores was measured in situ using optical microscopy (OM) [Olympus, USA] as shown in Fig. 1(c-d), or by intermittently quenching the samples to room temperature, deep into the glassy state of PS where no flow occurs, and scanning the film with atomic force microscopy (AFM) [Veeco Cailber, USA].

The AFM profiles of three pores in a film with thickness $h = 810\,\mathrm{nm}$ are shown in Fig. 2 for three different annealing times t at temperatures above T_g. The largest hole grew (left column), the next largest was stable over the timescale of the experiment (middle column), and the smallest hole shrank (right column). The size of the stable pore gives an estimate of $r_c \approx 500\,\mathrm{nm}$ for $h = 810\,\mathrm{nm}$.

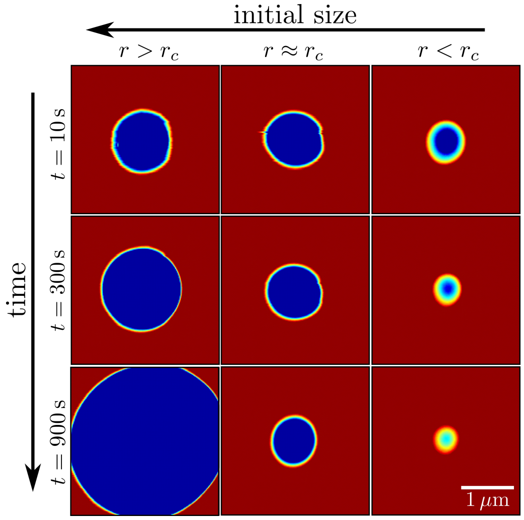

FIG. 2. The time evolution of pores in a viscous polystyrene membrane ($h = 810\,\mathrm{nm}$) as measured by AFM. The largest hole grows (left column), while the smallest hole closes (right column). An intermediate hole (middle column) is stable in size over the measurement.

In order to perform measurements on hundreds of pores in the same film, OM was used to measure the pore radius. Fig. 3 shows the time evolution of the radius of three different holes for a film $h \approx 900\,\mathrm{nm}$ thick. The largest pore grows exponentially with time, consistent with previous studies [28, 29, 34]. The intermediate sized pore does not change over the measurement, while the smallest hole rapidly shrinks. Repeating this measurement on a sample with hundreds of holes, we find only 8 stable holes. From the size of the stable holes, we find $r_c = 730 \pm 100\,\mathrm{nm}$ for $h = 965\,\mathrm{nm}$.

The results of $r_c(h)$ for 9 different PS film thicknesses are shown in Fig. 4 (black squares). For PS homopolymer films, the critical radius depends linearly on the film thickness.

To understand the linear relation between r_c and h, we need to consider the line tension term in Eq.(1). Since the PS films are composed of a single polymeric species and the film thickness is much larger than the typical molecular dimensions, the energy cost of creating the rim of the pore is just the bulk surface tension cost. If we consider the edge of the pore to be the a torus [26] with a diameter h, then the surface area of the rim is given by the surface area of the inner half of a torus $A = \pi^2 hr - \pi h^2$. This gives the free energy of the PS pore as

$$\frac{\Delta G(r)}{\gamma h^2} = -\pi + \pi^2 \left(\frac{r}{h}\right) - 2\pi \left(\frac{r}{h}\right)^2, \qquad (2)$$

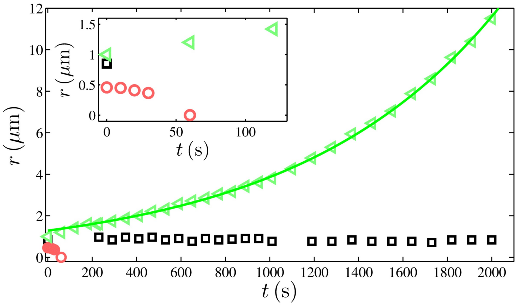

FIG. 3. The radius of three different sized pores in a film $h \approx 900\,\text{nm}$ thick. The pore which started off with the largest radius (green triangles) grew over time, while the smallest hole (red circles) shrank and closed. The intermediate sized pore (black squares) was stable in size during the measurement. The solid green line is a fit of $r = r_0 e^{t/\tau}$ to the growing hole, with $r_0 = 1.3\,\mu\text{m}$ and $\tau = 910\,\text{s}$. The inset shows the same data over a smaller range of time to highlight the dynamics of the shrinking pore.

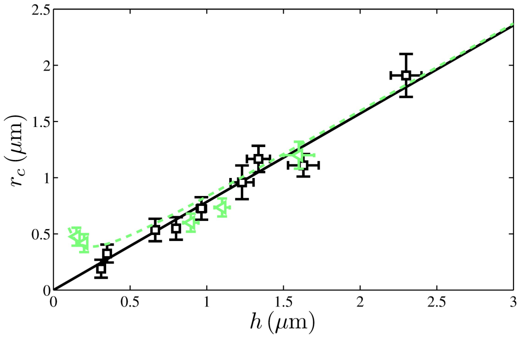

FIG. 4. The critical radius plotted as a function of film thickness for a PS homopolymer (black squares) and a PS-PMMA diblock copolymer with additional line tension (green triangles). For thick films, there is no difference in the critical radius. The line tension becomes important for thin films, and the critical radius of pores in the diblock films becomes larger than that in the homopolymer case. The black solid line is the theoretical prediction of Eq. (4) with no fitting parameters. The green line is a fit of Eq. (7) to the diblock copolymer data.

where we identify the line tension as

$$\Gamma_{\text{homopolymer}} = \frac{\gamma}{2}\left(\pi h - \frac{h^2}{r}\right). \tag{3}$$

The solid black line in Fig. 5 shows the free energy cost of a pore as given by Eq. (2). The single maximum of the free energy is an energy barrier to the growth of a pore. This prevents smaller pores from growing, and ultimately leads to their closure. Pores which are left of the peak in the free energy shrink, while those to the right of the peak grow. The critical radius is given by the maximum in the free energy, which we find by setting $\partial_r \Delta G|_{r=r_c} = 0$, which gives

$$r_c = \pi h/4. \tag{4}$$

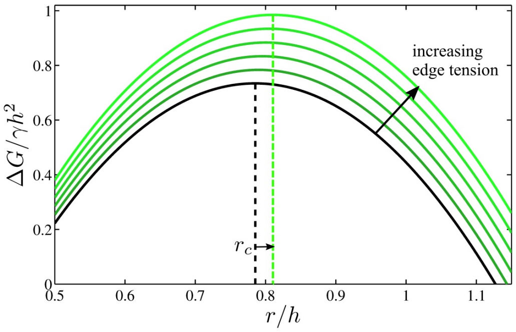

FIG. 5. The normalized free energy cost of creating a pore with radius r in a viscous membrane of film thickness h and surface tension γ. For $r < r_c$, the pore is unstable and will shrink. Larger pores with $r > r_c$ will grow exponentially in time. The solid black line is given by Eq. (1), and the value of r_c (dashed black line) is given by Eq. (4) for a film with no confinement effects. The green lines are the free energy cost of creating a pore when there is an additional contribution to the line tension from the molecular structure. The free energy barrier increases and r_c shifts further to the right as the energy cost of creating curvature at the edge of the pore increases (increasing edge tension). The green curves are generated by setting $2\pi\phi L/\gamma h^2 = \{0.02, 0.04, 0.06, 0.08, 0.1\}$ in Eq. (6), with higher values corresponding to larger edge tension and darker colored curves in the figure.

This theoretical expression for the critical radius is shown in Fig. 4 (black solid line). Eq.(4) agrees with the experimentally measured values with no fitting parameters. Since $h > 200\,\text{nm}$ for all measured films, the contribution from disjoining pressure is negligible [35]. The excellent agreement between the theory and experiment confirms the assumption that surface tension is the only free energy contribution in creating a pore in PS homopolymer films. The PS homopolymer films are behaving as model membranes with only the total surface area contributing to the free energy.

Now that we have a well-characterized model membrane, we turn to incorporating some aspects of biological membranes. The stability of pores in membranes is largely determined by the effects of line tension at the edge of the pore. For example, peptide binding can alter the line tension which stabilizes pores [18]. Here we explore the effect of altering the line tension in our model system by making a small alteration. Instead of using a homopolymer (as has been used up until this point in the letter) in our polymer membrane, we use a diblock copolymer. A diblock copolymer is a type of polymer in which each molecule contains two distinct chemical blocks [2]. Due to an enthalpic repulsion of the two parts of each chain, phase separation is favorable at sufficiently low temperatures. But because the two chemical species are covalently bonded together, phase separation can only occur on the lengthscale of the individual molecules (typically $10 - 100\,\mathrm{nm}$). Here we use a symmetric polystyrene-polymethylmethacrylate (PS-b-PMMA) diblock copolymer (with $M_n = 25\,\mathrm{kg/mol}$ for the PS block and $M_n = 26\,\mathrm{kg/mol}$ for the PMMA block, obtained from Polymer Source, Canada). A symmetric diblock copolymer will phase separate into lamellar layers with equilibrium thickness L, similar to a lipid bilayer. In fact, diblock copolymers have previously been used to model lipid bilayer membranes in previous theoretical work [26]. When confined to a thin film, there is an extra free energy cost of a curved diblock surface [36]. Unlike the case of a homopolymer membrane where the free energy cost at the edge of the pore is just due to the bulk surface tension of the fluid, a diblock copolymer has an added energy cost of rearranging molecules near the curved edge of the pore which is inversely related the radius of curvature. Here, the radius of curvature is $h/2$, and to first order this adds an additional cost to the line tension of a hole given by Eq. (3) in terms of the non-dimensional curvature L/h as

$$\Gamma_{\mathrm{diblock}} = \Gamma_{\mathrm{homopolymer}} + \phi \frac{L}{h}, \tag{5}$$

where ϕ is an energy cost per unit length associated with the curvature. Putting Eq. (5) into Eq. (1) gives

$$\frac{\Delta G(r)}{\gamma h^2} = -\pi + \left(\pi^2 + \frac{2\pi\phi L}{\gamma h^2}\right)\left(\frac{r}{h}\right) - 2\pi\left(\frac{r}{h}\right)^2. \tag{6}$$

The free energy cost of a pore in a system with an added line tension contribution is shown in Fig. 5. The free energy given by Eq. (6) is plotted for successively larger values of the line tension. The larger line tension creates a larger free energy barrier to hole growth, which shifts r_c to a progressively higher values.

The obtain the critical radius for the diblock copolymer case, we once again set $\partial_r \Delta G|_{r=r_c} = 0$, which results in the critical radius

$$r_c = \pi h/4 + \frac{\phi L}{2\gamma h}. \tag{7}$$

To test the scaling of Eq. (7), diblock copolymer membranes with pores were created in the same way as the PS homopolymer case, and the critical radius was measured for varying film thicknesses (triangles in Fig. 4). For thick films ($> 800\,\mathrm{nm}$), the critical radius measured in the diblock films show no significant difference from that of the homopolymer films. In thinner films, the effect of the additional line tension of the diblock copolymer film becomes important, and the critical radius begins to increase as the film thickness is decreased. The solid green line is the fit of Eq. (7) to the diblock data, which gives $\phi L/2\gamma = 0.0475\,\mu\mathrm{m}^2$. Given the surface tension $\gamma \approx 34\,\mathrm{mJ/m}^2$ and lamellar spacing $L = 27\,\mathrm{nm}$ [37], this gives the energy cost of confinement per unit length for this system as $\phi \sim 10^{-7}\,\mathrm{J/m}$.

Polymer membranes have provided a convenient system to examine a nucleated process. The ability to use direct optical measurements allows for a conceptually straightforward demonstration of nucleation and growth, which are important in many other physical processes. The simplicity of the system allows for an uncomplicated mathematical description of the physics involved. The ability to tune the pore stability by changing molecular architecture gives a clear understanding of the competing contributions to the free energy of the system.

In conclusion, we have studied the stability of pores in a model membrane. We find that for a simple polystyrene film, the critical radius depends linearly on the film thickness. A model which only accounts for the surface tension contribution to the free energy and takes into consideration the surface area at the edge of the pore describes our experimental results with no free parameters. On the other hand, we find that for a membrane made of a diblock copolymer the critical radius does not match the simple model for thin films. The ordered microstructure of the diblock causes deviations from the bulk free energy cost due to surface tension. This added contribution to the edge tension can be accommodated with an additional term in the free energy which becomes important for thin films. This modification is able to describe the experimental diblock copolymer critical radius with one fitting parameter. The study of pores in polymer membranes provides a model system for nucleation and growth where the critical radius can be derived from simple mathematical arguments. In this model membrane system the effect of the line tension, which is important to biological processes, can be altered simply by changing the molecular architecture of the polymer used in the membrane.

---

[*] dalnoki@mcmaster.ca

[1] J. Schmelzer, G. Röpke, and V. Priezzhev, *Nucleation theory and applications* (2005) p. 470.
[2] R. A. L. Jones, *Soft condensed matter*, Vol. 6 (Oxford University Press, 2002).
[3] P. H. Frampton, Phys. Rev. Lett. **37**, 1378 (1976).
[4] A. Lomakin, D. S. Chung, G. B. Benedek, D. A. Kirschner, and D. B. Teplow, Proc. Natl. Acad. Sci. U. S. A. **93**, 1125 (1996).
[5] K. Garai, B. Sahoo, P. Sengupta, and S. Maiti, J. Chem. Phys. **128** (2008), 10.1063/1.2822322.
[6] M. Piehl, U. S. Tulu, P. Wadsworth, and L. Cassimeris, Proc. Natl. Acad. Sci. U. S. A. **101**, 1584 (2004).
[7] R. Phillips, J. Kondev, J. Theriot, and H. Garcia, *Phys-*

ical biology of the cell (Garland Science, 2012).

[8] D. Yamashita, T. Sugawara, M. Takeshita, J. Kaneko, Y. Kamio, I. Tanaka, Y. Tanaka, and M. Yao, Nat. Commun. **5**, 4897 (2014).

[9] B. Coste, B. Xiao, J. S. Santos, R. Syeda, J. Grandl, K. S. Spencer, S. E. Kim, M. Schmidt, J. Mathur, A. E. Dubin, M. Montal, and A. Patapoutian, Nature **483**, 176 (2012).

[10] P. Agre, L. S. King, M. Yasui, W. B. Guggino, O. P. Ottersen, Y. Fujiyoshi, A. Engel, and S. r. Nielsen, J. Physiol. **542**, 3 (2002).

[11] C. Taupin, M. Dvolaitzky, and C. Sauterey, Biochemistry **14**, 4771 (1975).

[12] D. V. Zhelev and D. Needham, Biochim. Biophys. Acta - Biomembr. **1147**, 89 (1993).

[13] M. Bier, W. Chen, T. R. Gowrishankar, R. D. Astumian, and R. C. Lee, Phys. Rev. E **66**, 062905 (2002).

[14] S. Loi, G. Sun, V. Franz, and H.-J. Butt, Phys. Rev. E **66**, 031602 (2002).

[15] P.-H. Puech, N. Borghi, E. Karatekin, and F. Brochard-Wyart, Phys. Rev. Lett. **90**, 128304 (2003).

[16] E. Karatekin, O. Sandre, H. Guitouni, N. Borghi, P.-H. Puech, and F. Brochard-Wyart, Biophys. J. **84**, 1734 (2003).

[17] M. T. Lee, F. Y. Chen, and H. W. Huang, Biochemistry **43**, 3590 (2004).

[18] A. J. García-Sáez, S. Chiantia, J. Salgado, and P. Schwille, Biophys. J. **93**, 103 (2007).

[19] M.-T. Lee, W.-C. Hung, F.-Y. Chen, and H. W. Huang, Proc. Natl. Acad. Sci. U. S. A. **105**, 5087 (2008).

[20] R. Netz and M. Schick, Phys. Rev. E **53**, 3875 (1996).

[21] M. Muller and M. Schick, J. Chem. Phys. **105**, 8282 (1996).

[22] V. Talanquer and D. W. Oxtoby, J. Chem. Phys. **118**, 872 (2003).

[23] H. Leontiadou, A. E. Mark, and S. J. Marrink, Biophys. J. **86**, 2156 (2004).

[24] T. V. Tolpekina, W. K. den Otter, and W. J. Briels, J. Chem. Phys. **121**, 12060 (2004).

[25] Z.-J. Wang and D. Frenkel, J. Chem. Phys. **123**, 154701 (2005).

[26] J. Li, K. A. Pastor, A. C. Shi, F. Schmid, and J. Zhou, Phys. Rev. E - Stat. Nonlinear, Soft Matter Phys. **88**, 1 (2013).

[27] G. Debregeas, P. de Gennes, and F. Brochard-Wyart, Science (80-.). **279**, 1704 (1998).

[28] K. Dalnoki-Veress, B. Nickel, C. Roth, and J. Dutcher, Phys. Rev. E **59**, 2153 (1999).

[29] A. B. Croll and K. Dalnoki-Veress, Soft Matter **6**, 5547 (2010).

[30] J. M. Rathfon, R. W. Cohn, A. J. Crosby, and G. N. Tew, Macromolecules **44**, 134 (2011).

[31] J. P. Singer, S. E. Kooi, and E. L. Thomas, Nanoscale **3**, 2730 (2011).

[32] J. P. Singer, P.-T. Lin, S. E. Kooi, L. C. Kimerling, J. Michel, and E. L. Thomas, Adv. Mater. **25**, 6100 (2013).

[33] M. Benzaquen, M. Ilton, M. V. Massa, T. Salez, P. Fowler, E. Raphaël, and K. Dalnoki-Veress, Appl. Phys. Lett. **107**, 053103 (2015).

[34] G. Debrégeas, P. Martin, and F. Brochard-Wyart, Phys. Rev. Lett. **75**, 3886 (1995).

[35] K. Jacobs, R. Seemann, and S. Herminghaus, in *Polym. Thin Film.*, edited by O. K. C. Tsui and T. P. Russell (World Scientific, 2008) Chap. 10, pp. 243–265.

[36] G. M. Wilmes, D. a. Durkee, N. P. Balsara, and J. A. Liddle, Macromolecules **39**, 2435 (2006).

[37] A. Croll, M. Massa, M. Matsen, and K. Dalnoki-Veress, Phys. Rev. Lett. **97**, 1 (2006).

Chapter 4

Conclusions

This thesis work has focused on the study of capillary driven flow mediated by viscosity in thin polymer films. We have used a variety of sample geometries to study flow: the capillary levelling of trenches, divots, and steps was used to extract quantitative information about the rheological properties of films. Droplet spreading was used to investigate dissipation in a polymer fluid. The dynamics of pores opening or closing in a polymer membrane was used to study nucleation.

In all of the studies, the properties of the polymer fluid played a role in the dynamics. The temperature and molecular weight dependent viscosity of polymeric liquids determined the rate at which energy dissipation occurred. The size and the molecular structure of the polymer chains had important effects on the boundary condition and free energy of the films.

There is a strong connection between the free energy of the film and the dynamics of flow. When the film is in a high energy state, a driving force pushes the liquid to flow. In Papers I and II, this connection between the equilibrium free energy and flow allowed for the careful study of a partially wetting fluid. The presence of a bulk disordered state with interfacially induced ordering resulted in a non-monotonic film thickness dependence of the free energy. As a direct consequence of the decaying oscillatory interface potential energy we were able to observe the unique phenomenon detailed in Paper I. For a single liquid on a homogeneous substrate, the fluid dewetted into droplets which did not have a single contact angle as is usually the case; the droplets dewetted into a discrete spectrum of contact angles. Using the temperature dependence of this spectrum, we studied the dynamics of the droplets as they approached equilibrium. Unlike other systems where the dissipation in droplets mostly occurs at the contact line, in Paper II we found that the droplets forming the spectrum of contact angles dissipated energy at the base of the droplets. This was consistent with an effective slip boundary condition at the liquid-solid interface.

In the other three papers, the connection between the flow and the free energy of the film was more straightforward. In those works, flow was induced purely by the extra surface area of the fluid which was a free energy cost due to surface tension. We used these purely capillary driven systems to study the effect of different initial conditions and boundary conditions.

In Paper III, initial conditions with different symmetry and effective dimensionality were created in supported films. The initial perturbations decayed over time, as the excess surface area decreases bringing the film towards its equilibrium flat state. The depth of the perturbations decayed as a power law in time with an exponent that depended upon the initial symmetry and effective dimensionality of the perturbation. The types of features slowest to decay are 2D features in which material is added or removed from a flat film. Faster erasing of surface features can be achieved by creating a 3D feature with a higher order symmetry.

The boundary condition was changed in Papers IV and V. Instead of working with polymer films supported underneath by a solid substrate, films were freely-suspended by holding them at their edges. This removed any interfacial friction in the system which had a drastic impact on flow. In Paper IV, we used capillary levelling to show that the flow in freestanding viscous films is consistent with plug flow: a flow profile where there is no gradient in horizontal velocity in the direction perpendicular to the film.

Freely-suspended films were then used as a model membrane in Paper V. By creating pores of various sizes in viscous polymer membranes, we observed that some pores grew, others shrank, and some did not change over hours of heating above the glass transition temperature of the film. From this we were able to determine that the critical radius for pore growth depended linearly on film thickness, which agreed well with a simple model with no fitting parameters. It was found that the critical radius could be made larger by using a diblock copolymer membrane because of the larger energy cost at the edge of a pore.

In this thesis, three themes in which molecular details have a role in determining the flow in a viscous fluid film were addressed. First, the structure of a diblock copolymer fluid can lead to modifications to the boundary condition. Second, the dynamics of flow depends on the symmetry of the initial condition. Third, removing interfacial friction at the boundary of a fluid film drastically alters the velocity profile in the fluid as it flows.

One intriguing aspect of all these situations is how continuum fluid dynamics still works remarkably well. Even in situations where molecular details are important, continuum mechanics is still able to describe the flow we observe. The relative importance of the terms in the Stokes' equations change, which results in qualitative differences in the dynamics of flow. However, the same framework is still able to give quantitative details in a wide array of situations.

There are some natural extensions to the work presented in this thesis, some of which are ongoing work. For example, the diblock copolymer droplet shown in figure 2.5 which coexisted with two different wetting layer thicknesses has a different contact angle on each side. This causes an unbalanced force on the droplet and as a result, the droplet moves towards the side with a thicker wetting layer. The measurement of this effect is a work in progress.

Another ongoing project is measuring the capillary levelling of a viscous film on a thin, flexible substrate. If the substrate is thin enough, the viscous film will undergo a symmetrization similar to a freestanding film. However, since there is still a no-slip boundary condition at the interface between the viscous film and the flexible substrate, the flow has the same self-similar scaling as a film supported by a rigid substrate.

The ability to use AFM on a freestanding film has provided our group with some new avenues of research. For example, future work could examine the universal attractors for a freestanding film. Since the linearized freestanding thin film equation is simply the heat equation, the attractor functions are analytically solvable. In fact, the zeroth order attractor for the case of non-zero volume should be a Gaussian function. The higher order attractors would then be derivatives of the Gaussian function.

Perhaps the most interesting extension to this thesis would be the use of freestanding films to probe some of the existing questions in the literature. How does the surface of a glassy freestanding film flow, and how does this depend on molecular weight? How does flow in a freestanding film change when the polymer molecules are confined? Is it possible to measure surface fluctuations in freestanding films similar to the way it is done in the supported case? Progress on answering these questions could provide an important contribution to the field of polymer physics.

Bibliography

[1] S.-M. Park, O.-H. Park, J. Y. Cheng, C. T. Rettner, and H.-C. Kim. Patterning sub-10nm line patterns from a block copolymer hybrid. *Nanotechnology*, 19(45), 455304, (2008).

[2] J. G. Son, J.-B. Chang, K. K. Berggren, and C. A. Ross. Assembly of sub-10-nm block copolymer patterns with mixed morphology and period using electron irradiation and solvent annealing. *Nano Lett.*, 11(11), 5079–84, (2011).

[3] C. M. Bates, T. Seshimo, M. J. Maher, W. J. Durand, J. D. Cushen, L. M. Dean, G. Blachut, C. J. Ellison, and C. G. Willson. Polarity-switching top coats enable orientation of sub-10-nm block copolymer domains. *Science*, 338(6108), 775–9, (2012).

[4] O. K. C. Tsui and T. P. Russell, editors. *Polymer Thin Films.* World Scientific, (2008).

[5] R. Blossey. *Thin Liquid Films: Dewetting and Polymer Flow.* Springer, (2012).

[6] M. Rubinstein and R. H. Colby. *Polymer Physics.* OUP Oxford, (2003).

[7] L. Fetters, D. Lohse, and D. Richter. Connection between polymer molecular weight, density, chain dimensions, and melt viscoelastic properties. *Macromolecules*, 27(17), (1994).

[8] A. B. Croll, M. W. Matsen, A.-C. Shi, and K. Dalnoki-Veress. Kinetics of layer hopping in a diblock copolymer lamellar phase. *Eur. Phys. J. E*, 411, 407–411, (2008).

[9] A. R. Khokhlov and P. G. de Gennes. *Giant Molecules: Here, There, and Everywhere*. World Scientific, (2011).

[10] M. Doi. *Introduction to Polymer Physics*. Clarendon Press, (1996).

[11] R. H. Colby, L. J. Fetters, and W. W. Graessley. Melt viscosity-molecular weight relationship for linear polymers. *Macromolecules*, 20(9), 2226–2237, (1987).

[12] J. D. McGraw, N. M. Jago, and K. Dalnoki-Veress. Capillary levelling as a probe of thin film polymer rheology. *Soft Matter*, 7(17), 7832, (2011).

[13] J. D. McGraw, T. Salez, O. Bäumchen, E. Raphaël, and K. Dalnoki-Veress. Self-Similarity and Energy Dissipation in Stepped Polymer Films. *Phys. Rev. Lett.*, 109(12), 128303, (2012).

[14] L. J. Fetters, D. J. Lohse, S. T. Milner, and W. W. Graessley. Packing length influence in linear polymer melts on the entanglement, critical, and reptation molecular weights. *Macromolecules*, 32(20), 6847–6851, (1999).

[15] J. C. Mauro, Y. Yue, A. J. Ellison, P. K. Gupta, and D. C. Allan. Viscosity of glass-forming liquids. *Proc. Natl. Acad. Sci. U. S. A.*, 106(47), 19780–19784, (2009).

[16] I. Hamley. Ordering in thin films of block copolymers: Fundamentals to potential applications. *Prog. Polym. Sci.*, 34(11), 1161–1210, (2009).

[17] A. Marchand, J. H. Weijs, J. H. Snoeijer, and B. Andreotti. Why is surface tension a force parallel to the interface? *Am. J. Phys.*, 79(10), 999, (2011).

[18] S. Wu. Surface and Interfacial Tensions of Polymer Melts II. Poly(methyl methacrylate), Poly(n-butyl methacrylate) and Polystyrene. *J. Phys. Chem.*, 74(3), 632–638, (1970).

[19] G. T. Dee and B. B. Sauer. The surface tension of polymer blends: theory and experiment. *Macromolecules*, 26(11), 2771–2778, (1993).

[20] J. E. Mark. *Polymer Data Handbook*. Oxford University Press, (2009).

[21] D. Legrand and G. Gaines. The molecular weight dependence of polymer surface tension. *J. Colloid Interface Sci.*, 31(2), 162–167, (1969).

[22] G. T. Dee, T. O, and D. J. Walsh. The pressure-volume-temperature properties of polyethylene , poly (dimethyl siloxane), poly (ethylene glycol) and poly (propylene glycol) as a function of molecular weight. *Polymer (Guildf).*, 33(16), 3462–3469, (1992).

[23] B. B. Sauer and G. T. Dee. Studies of Polymer, Copolymer, and Associating Liquids by Melt Surface Tension Methods and Cahn-Hilliard Density-Gradient Theory. *J. Colloid Interface Sci.*, 162(1), 25–35, (1994).

[24] R. B. Thompson, J. R. MacDonald, and P. Chen. Origin of change in molecular-weight dependence for polymer surface tension. *Phys. Rev. E*, 78(3), 030801, (2008).

[25] G. T. Dee and B. B. Sauer. The molecular weight and temperature dependence of polymer surface tension: Comparison of experiment with interface gradient theory. *J. Colloid Interface Sci.*, 152(1), 85–103, (1992).

[26] K. Jacobs, R. Seemann, and S. Herminghaus. Stability and dewetting of thin liquid films. In O. K. C. Tsui and T. P. Russell, editors, *Polym. Thin Film.*, chapter 10, pages 243–265. World Scientific, (2008).

[27] R. Seemann, S. Herminghaus, and K. Jacobs. Dewetting Patterns and Molecular Forces: A Reconciliation. *Phys. Rev. Lett.*, 86(24), 5534–5537, (2001).

[28] K. Jacobs, R. Seemann, G. Schatz, and S. Herminghaus. Growth of Holes in Liquid Films with Partial Slippage. *Langmuir*, 14(18), 4961–4963, (1998).

[29] M. Ilton, P. Stasiak, M. W. Matsen, and K. Dalnoki-Veress. Quantized Contact Angles in the Dewetting of a Structured Liquid. *Phys. Rev. Lett.*, 112(6), 068303, (2014).

[30] M. Müller and L. G. MacDowell. Nano-dewetting: Interplay between van der Waals- and short-ranged interactions. *J. Chem. Phys.*, 115, 9960–9969, (2001).

[31] R. Seemann, S. Herminghaus, and K. Jacobs. Gaining control of pattern formation of dewetting liquid films. *J. Phys. Condens. Matter*, 13(21), 4925–4938, (2001).

[32] R. A. L. Jones. *Soft condensed matter.* Oxford University Press, New York, (2002).

[33] J. N. Israelachvili. *Intermolecular and Surface Forces: Revised Third Edition.* Intermolecular and Surface Forces. Elsevier Science, (2011).

[34] A. W. Adamson. *Physical Chemistry of Surfaces.* A Wiley-Interscience publication. Wiley, (1990).

[35] R. Limary, P. F. Green, and K. R. Shull. Influence of surface ordering on the wetting of structured liquids. *Eur. Phys. J. E*, 8(2), 103–110, (2002).

[36] M. W. Matsen. Thin films of block copolymer. *J. Chem. Phys.*, 106, 7781–7791, (1997).

[37] X. Xu, U. Thiele, and T. Qian. A Variational approach to thin film hydrodynamics of binary mixtures. *J. Phys. Condens. Matter*, 27(8), 085005, (2015).

[38] R. Xie, A. Karim, J. Douglas, C. Han, and R. Weiss. Spinodal Dewetting of Thin Polymer Films. *Phys. Rev. Lett.*, 81(6), 1251–1254, (1998).

[39] J. Pellicer. The physical description of elementary surface phenomena: Thermodynamics versus mechanics. *Am. J. Phys.*, 63(6), 542, (1995).

[40] A. Münch, B. Wagner, and T. P. Witelski. Lubrication models with small to large slip lengths. *J. Eng. Math.*, 53(3-4), 359–383, (2005).

[41] T. Salez, J. D. McGraw, O. Bäumchen, K. Dalnoki-Veress, and E. Raphaël. Capillary-driven flow induced by a stepped perturbation atop a viscous film. *Phys. Fluids*, 24(10), 102111, (2012).

[42] T. Salez, J. D. McGraw, S. L. Cormier, O. Bäumchen, K. Dalnoki-Veress, and E. Raphaël. Numerical solutions of thin-film equations for polymer flows. *Eur. Phys. J. E*, 35(11), 114, (2012).

[43] G. I. Barenblatt. *Scaling, Self-similarity, and Intermediate Asymptotics.* Cambridge University Press, (1996).

[44] M. Rauscher, R. Blossey, A. Münch, and B. Wagner. Spinodal dewetting of thin films with large interfacial slip: Implications from the dispersion relation. *Langmuir*, 24(21), 12290–12294, (2008).

[45] M. Benzaquen, T. Salez, and E. Raphaël. Intermediate asymptotics of the capillary-driven thin-film equation. *Eur. Phys. J. E*, 36(8), 82, (2013).

[46] S. Cormier, J. McGraw, T. Salez, E. Raphaël, and K. Dalnoki-Veress. Beyond Tanners Law: Crossover between Spreading Regimes of a Viscous Droplet on an Identical Film. *Phys. Rev. Lett.*, 109(15), 1–5, (2012).

[47] M. Backholm, M. Benzaquen, T. Salez, E. Raphaël, and K. Dalnoki-Veress. Capillary levelling of a cylindrical hole in a viscous film. *Soft Matter*, 10(15), 2550–8, (2014).

[48] R. N. Li, F. Chen, C.-H. Lam, and O. K. C. Tsui. Viscosity of PMMA on Silica: Epitome of Systems with Strong PolymerSubstrate Interactions. *Macromolecules*, 46(19), 7889–7893, (2013).

[49] P. C. Lee, H. E. Park, D. C. Morse, and C. W. Macosko. Polymer-polymer interfacial slip in multilayered films. *J. Rheol. (N. Y. N. Y).*, 53, 893, (2009).

[50] G. Reiter. Mobility of Polymers in Films Thinner than Their Unperturbed Size. *Europhys. Lett.*, 23(8), 579–584, (2007).

[51] T. Koga, C. Li, M. K. Endoh, J. Koo, M. Rafailovich, S. Narayanan, D. R. Lee, L. B. Lurio, and S. K. Sinha. Reduced Viscosity of the Free Surface in Entangled Polymer Melt Films. *Phys. Rev. Lett.*, 104(6), 066101, (2010).

[52] F. Chen, D. Peng, C.-H. Lam, and O. K. C. Tsui. Viscosity and Surface-Promoted Slippage of Thin Polymer Films Supported by a Solid Substrate. *Macromolecules*, page 150709130643005, (2015).

[53] E. Rognin, S. Landis, and L. Davoust. Viscoelastic leveling of annealed thin polystyrene films. *Langmuir*, 30(23), 6963–9, (2014).

[54] E. Rognin, S. Landis, and L. Davoust. Viscoelastic properties measurements of thin polymer films from reflow of nanoimprinted patterns. *J. Vac. Sci. Technol. B Microelectron. Nanom. Struct.*, 30(2012), 011602, (2012).

[55] J. H. Teichroeb and J. A. Forrest. Direct imaging of nanoparticle embedding to probe viscoelasticity of polymer surfaces. *Phys. Rev. Lett.*, 91(1), 016104, (2003).

[56] Z. Fakhraai, S. Valadkhan, and J. A. Forrest. Qualitative discrepancy between different measures of dynamics in thin polymer films. *Eur. Phys. J. E. Soft Matter*, 18(2), 143–8, (2005).

[57] R. M. Papaléo, R. Leal, W. H. Carreira, L. G. Barbosa, I. Bello, and a. Bulla. Relaxation times of nanoscale deformations on the surface of a polymer thin film near and below the glass transition. *Phys. Rev. B - Condens. Matter Mater. Phys.*, 74(9), 1–5, (2006).

[58] Z. Fakhraai and J. A. Forrest. Measuring the surface dynamics of glassy polymers. *Science (80-.).*, 319(5863), 600–604, (2008).

[59] M. Ilton, D. Qi, and J. A. Forrest. Using nanoparticle embedding to probe surface rheology and the length scale of surface mobility in glassy polymers. *Macromolecules*, 42(18), 6851–6854, (2009).

[60] A. Serghei, M. Tress, and F. Kremer. The glass transition of thin polymer films in relation to the interfacial dynamics. *J. Chem. Phys.*, 131(15), 154904, (2009).

[61] Z. Yang, Y. Fujii, F. K. Lee, C.-H. Lam, and O. K. C. Tsui. Glass transition dynamics and surface layer mobility in unentangled polystyrene films. *Science*, 328(5986), 1676–9, (2010).

[62] J. E. Pye, K. A. Rohald, E. A. Baker, and C. B. Roth. Physical Aging in Ultrathin Polystyrene Films: Evidence of a Gradient in Dynamics at the Free Surface and Its Connection to the Glass Transition Temperature Reductions. *Macromolecules*, 43(19), 8296–8303, (2010).

[63] Y. Chai, T. Salez, J. D. McGraw, M. Benzaquen, K. Dalnoki-Veress, E. Raphaël, and J. A. Forrest. A direct quantitative measure of surface mobility in a glassy polymer. *Science (80-.).*, 343(6174), 994–999, (2014).

[64] Y. L. Zhang, R. V. Craster, and O. K. Matar. Surfactant driven flows overlying a hydrophobic epithelium: Film rupture in the presence of slip. *J. Colloid Interface Sci.*, 264(1), 160–175, (2003).

[65] D. Peschka, a. Münch, and B. Niethammer. Thin-film rupture for large slip. *J. Eng. Math.*, 66(October 2009), 33–51, (2010).

[66] O. Bäumchen, R. Fetzer, M. Klos, M. Lessel, L. Marquant, H. Hähl, and K. Jacobs. Slippage and nanorheology of thin liquid polymer films. *J. Phys. Condens. Matter*, 24(32), 325102, (2012).

[67] P. C. Lee, H. E. Park, D. C. Morse, and C. W. Macosko. Polymer-polymer interfacial slip in multilayered films. *J. Rheol. (N. Y. N. Y).*, 53(4), 893, (2009).

[68] J.-H. Cho, B. Law, and F. Rieutord. Dipole-Dependent Slip of Newtonian Liquids at Smooth Solid Hydrophobic Surfaces. *Phys. Rev. Lett.*, 92(16), 166102, (2004).

[69] E. Lauga, M. Brenner, and H. Stone. Microfluidics: The No-Slip Boundary Condition. In C. Tropea, A. L. Yarin, and J. F. Foss, editors, *Springer Handb. Exp. Fluid Mech.*, chapter 19, pages 1219–1240. Springer Berlin Heidelberg, (2007).

[70] P. L. Evans, J. R. King, and A. M. Intermediate-Asymptotic Structure of a Dewetting Rim with Strong Slip. 2006, 1–25, (2006).

[71] R. Fetzer and K. Jacobs. Slippage of newtonian liquids: Influence on the dynamics of dewetting thin films. *Langmuir*, 23(23), 11617–11622, (2007).

[72] T. Schmatko, H. Hervet, and L. Leger. Friction and slip at simple fluid-solid interfaces: The roles of the molecular shape and the solid-liquid interaction. *Phys. Rev. Lett.*, 94(24), 1–4, (2005).

[73] Y. Zhu and S. Granick. Rate-dependent slip of Newtonian liquid at smooth surfaces. *Phys. Rev. Lett.*, 87(9), 096105, (2001).

[74] G. Reiter and R. Khanna. Real-time determination of the slippage length in autophobic polymer dewetting. *Phys. Rev. Lett.*, 85(13), 2753–6, (2000).

[75] O. Bäumchen, L. Marquant, R. Blossey, A. Münch, B. Wagner, and K. Jacobs. Influence of Slip on the Rayleigh-Plateau Rim Instability in Dewetting Viscous Films. *Phys. Rev. Lett.*, 113(1), 014501, (2014).

[76] A. Münch and B. Wagner. Impact of slippage on the morphology and stability of a dewetting rim. *J. Phys. Condens. Matter*, 23(18), 184101, (2011).

[77] R. Pit, H. Hervet, and L. Léger. Direct experimental evidence of slip in hexadecane: solid interfaces. *Phys. Rev. Lett.*, 85(5), 980–983, (2000).

[78] J.-L. Barrat and L. Bocquet. Large Slip Effect at a Nonwetting Fluid-Solid Interface. *Phys. Rev. Lett.*, 82(23), 4671–4674, (1999).

[79] C. Cottin-Bizonne, B. Cross, a. Steinberger, and E. Charlaix. Boundary Slip on Smooth Hydrophobic Surfaces: Intrinsic Effects and Possible Artifacts. *Phys. Rev. Lett.*, 94(5), 056102, (2005).

[80] G. Kitavtsev and B. Wagner. Coarsening dynamics of slipping droplets. *J. Eng. Math.*, 66(1), 271–292, (2010).

[81] Y. Zhu and S. Granick. No-slip boundary condition switches to partial slip when fluid contains surfactant. *Langmuir*, 18(26), 10058–10063, (2002).

[82] O. Bäumchen and K. Jacobs. Slip effects in polymer thin films. *J. Phys. Condens. Matter*, 22, 033102, (2010).

[83] S. Granick, Y. Zhu, and H. Lee. Slippery questions about complex fluids flowing past solids. *Nat. Mater.*, 2(4), 221–227, (2003).

[84] Y. Zhu and S. Granick. Apparent slip of Newtonian fluids past adsorbed polymer layers. *Macromolecules*, 35(12), 4658–4663, (2002).

[85] S. Haefner, M. Benzaquen, O. Bäumchen, T. Salez, R. Peters, J. D. McGraw, K. Jacobs, E. Raphaël, and K. Dalnoki-Veress. Influence of slip on the Plateau-Rayleigh instability on a fibre. *Nat. Commun.*, 6(May), 7409, (2015).

[86] C. Neto, D. R. Evans, E. Bonaccurso, H.-J. Butt, and V. S. J. Craig. Boundary slip in Newtonian liquids: a review of experimental studies. *Reports Prog. Phys.*, 68(12), 2859–2897, (2005).

[87] R. Blossey, A. Münch, M. Rauscher, and B. Wagner. Slip vs. viscoelasticity in dewetting thin films. *Eur. Phys. J. E*, 20(3), 267–271, (2006).

[88] O. K. C. Tsui, Y. J. Wang, F. K. Lee, C. H. Lam, and Z. Yang. Equilibrium pathway of spin-coated polymer films. *Macromolecules*, 41(4), 1465–1468, (2008).

[89] Y. Wang and O. K. Tsui. Mean-field description of spinodal growth of surface waves on rupturing films. *J. Non. Cryst. Solids*, 352(42-49), 4977–4982, (2006).

[90] Z. Yang, C. H. Lam, E. Dimasi, N. Bouet, J. Jordan-Sweet, and O. K. C. Tsui. Method to measure the viscosity of nanometer liquid films from the surface fluctuations. *Appl. Phys. Lett.*, 94(25), 3–6, (2009).

[91] Z. Yang, Y. Fujii, F. K. Lee, C.-H. Lam, and O. K. C. Tsui. Glass transition dynamics and surface layer mobility in unentangled polystyrene films. *Science*, 328(2010), 1676–1679, (2010).

[92] R. N. Li, A. Clough, Z. Yang, and O. K. C. Tsui. Equilibration of polymer films cast from solutions with different solvent qualities. *Macromolecules*, 45(2), 1085–1089, (2012).

[93] H. Kim, a. Rühm, L. B. Lurio, J. K. Basu, J. Lal, D. Lumma, S. G. J. Mochrie, and S. K. Sinha. Surface Dynamics of Polymer Films. *Phys. Rev. Lett.*, 90(6), 068302, (2003).

[94] T. Koga, N. Jiang, P. Gin, M. K. Endoh, S. Narayanan, L. B. Lurio, and S. K. Sinha. Impact of an Irreversibly Adsorbed Layer on Local Viscosity of Nanoconfined Polymer Melts. *Phys. Rev. Lett.*, 107(22), 225901, (2011).

[95] G. Reiter, M. Hamieh, P. Damman, S. Sclavons, S. Gabriele, T. Vilmin, and E. Raphaël. Residual stresses in thin polymer films cause rupture and dominate early stages of dewetting. *Nat. Mater.*, 4(10), 754–8, (2005).

[96] J. N. Israelachvili. Measurement of the viscosity of liquids in very thin films. *J. Colloid Interface Sci.*, 110(1), 263–271, (1986).

[97] J. Baudry, E. Charlaix, a. Tonck, and D. Mazuyer. Experimental evidence for a large slip effect at a nonwetting fluid-solid interface. *Langmuir*, 17(17), 5232–5236, (2001).

[98] V. Craig, C. Neto, and D. Williams. Shear-Dependent Boundary Slip in an Aqueous Newtonian Liquid. *Phys. Rev. Lett.*, 87(5), 054504, (2001).

[99] O. I. Vinogradova and G. E. Yakubov. Dynamic effects on force measurements. 2. Lubrication and the atomic force microscope. *Langmuir*, 19(4), 1227–1234, (2003).

[100] C. Redon, F. Brochard-Wyart, and F. Rondelez. Dynamics of dewetting. *Phys. Rev. Lett.*, 66(6), 715–718, (1991).

[101] C. Redon, J. B. Brzoska, and F. Brochard-Wyart. Dewetting and slippage of microscopic polymer films. *Macromolecules*, 27, 468–471, (1994).

[102] G. Reiter and A. Sharma. Auto-Optimization of Dewetting Rates by Rim Instabilities in Slipping Polymer Films. *Phys. Rev. Lett.*, 87(16), 166103, (2001).

[103] S.-H. Choi and B.-M. Zhang Newby. Dynamic contact angle in rim instability of dewetting holes. *J. Chem. Phys.*, 124(5), 054702, (2006).

[104] O. Bäumchen and K. Jacobs. Slip effects in polymer thin films. *J. Phys. Condens. Matter*, 22(3), 033102, (2010).

[105] S. Sabzevari, J. D. McGraw, K. Jacobs, and P. Wood-Adams. Sacrificial Mica Substrates Influence the Slip Boundary Condition of Dewetting Polymer Films. *Polymer (Guildf).*, (2015).

[106] R. Seemann, S. Herminghaus, and K. Jacobs. Shape of a Liquid Front upon Dewetting. *Phys. Rev. Lett.*, 87(19), 196101, (2001).

[107] O. Bäumchen, R. Fetzer, and K. Jacobs. Reduced Interfacial Entanglement Density Affects the Boundary Conditions of Polymer Flow. *Phys. Rev. Lett.*, 103(24), 1–4, (2009).

[108] J. H. Snoeijer and B. Andreotti. Moving Contact Lines: Scales, Regimes, and Dynamical Transitions. *Annu. Rev. Fluid Mech.*, 45(1), 269–292, (2013).

[109] L. Tanner. The spreading of silicone oil drops on horizontal surfaces. *J. Phys. D. Appl. Phys.*, 12(9), 1473–1484, (1979).

[110] G. McHale and M. I. Newton. Frenkel's method and the dynamic wetting of heterogeneous planar surfaces. *Colloids Surfaces A Physicochem. Eng. Asp.*, 206(1-3), 193–201, (2002).

[111] P. de Gennes. Wetting: Statics and dynamics. *Rev. Mod. Phys.*, 57(3), 827–863, (1985).

[112] M. Ilton, O. Bäumchen, and K. Dalnoki-Veress. Onset of Area-Dependent Dissipation in Droplet Spreading. *Phys. Rev. Lett.*, 115(4), 046103, (2015).

[113] G. McHale, C. V. Brown, and N. Sampara. Voltage-induced spreading and superspreading of liquids. *Nat. Commun.*, 4, 1605, (2013).

[114] E. Pérez, E. Schäffer, and U. Steiner. Spreading Dynamics of Polydimethylsiloxane Drops: Crossover from Laplace to Van der Waals Spreading. *J. Colloid Interface Sci.*, 234(1), 178–193, (2001).

[115] J. D. McGraw, T. S. Chan, S. Maurer, T. Salez, M. Benzaquen, É. Raphaël, M. Brinkmann, and K. Jacobs. Slip-Mediated Dewetting of Polymer Microdroplets. (2015).

[116] T. Leveder, S. Landis, and L. Davoust. Reflow dynamics of thin patterned viscous films. *Appl. Phys. Lett.*, 92(1), 013107, (2008).

[117] T. Leveder, E. Rognin, S. Landis, and L. Davoust. Reflow of supported sub-100nm polymer films as a characterization process for NanoImprint lithography. *Microelectron. Eng.*, 88(8), 1867–1870, (2011).

[118] E. Rognin, S. Landis, and L. Davoust. Viscosity measurements of thin polymer films from reflow of spatially modulated nanoimprinted patterns. *Phys. Rev. E*, 84(4), 041805, (2011).

[119] E. Rognin, S. Landis, and L. Davoust. Viscoelastic properties measurements of thin polymer films from reflow of nanoimprinted patterns. *J. Vac. Sci. Technol. B Microelectron. Nanom. Struct.*, 30(1), 011602, (2012).

[120] O. Bäumchen, M. Benzaquen, T. Salez, J. D. McGraw, M. Backholm, P. Fowler, E. Raphaël, and K. Dalnoki-Veress. Relaxation and intermediate asymptotics of a rectangular trench in a viscous film. *Phys. Rev. E*, 88(3), 035001, (2013).

[121] M. Benzaquen, P. Fowler, L. Jubin, T. Salez, K. Dalnoki-Veress, and E. Raphaël. Approach to universal self-similar attractor for the levelling of thin liquid films. *Soft Matter*, 10(43), 8608–8614, (2014).

[122] J. D. McGraw, P. D. Fowler, M. L. Ferrari, and K. Dalnoki-Veress. Relaxation of non-equilibrium entanglement networks in thin polymer films. *Eur. Phys. J. E. Soft Matter*, 36(1), 7, (2013).

[123] D. Qi, M. Ilton, and J. A. Forrest. Measuring surface and bulk relaxation in glassy polymers. *Eur. Phys. J. E. Soft Matter*, 34(6), 1–7, (2011).

[124] Z. H. Yang, Y. J. Wang, L. Todorova, and O. K. C. Tsui. Examination of Nonliquidlike Behaviors in Molten Polymer Films. *Macromolecules*, 41(22), 8785–8788, (2008).

[125] Y. Zhu and S. Granick. Limits of the hydrodynamic no-slip boundary condition. *Phys. Rev. Lett.*, 88(10), 106102, (2002).

[126] O. Bäumchen and K. Jacobs. Can liquids slide? Linking stability and dynamics of thin liquid films to microscopic material properties. *Soft Matter*, 6(24), 6028, (2010).

[127] L. E. Scriven. Physics and applications of dip coating and spin coating. In *MRS Proc.*, volume 121, page 717. Cambridge Univ Press, (1988).

[128] C. M. Stafford, K. E. Roskov, T. H. Epps, and M. J. Fasolka. Generating thickness gradients of thin polymer films via flow coating. *Rev. Sci. Instrum.*, 77(2), 1–7, (2006).

[129] D. B. Hall, P. Underhill, and J. M. Torkelson. Spin Coating of Thin and Ultrathin Polymer Films. *Polym. Eng. Sci.*, 38(12), 2039–2045, (1998).

[130] W. W. Flack, D. S. Soong, A. T. Bell, and D. W. Hess. A mathematical model for spin coating of polymer resists. *J. Appl. Phys.*, 56(4), 1199, (1984).

[131] J. P. Singer, P.-T. Lin, S. E. Kooi, L. C. Kimerling, J. Michel, and E. L. Thomas. Direct-write thermocapillary dewetting of polymer thin films by a laser-induced thermal gradient. *Adv. Mater.*, 25(42), 6100–6105, (2013).

[132] O. S. Heavens. Optical properties of thin films. *Reports Prog. Phys.*, 23(1), 1–65, (1960).

[133] J. D. McGraw. *Non-Equilibrium Topographies: Surface Tension Driven Flows Reveal Polymer Properties at the Nanoscale.* Doctoral thesis, McMaster University, (2012).